UNIVERSITY OF CALIFRONIA

Los Angeles

Geochemical Tracers of Crustal Thickness and Their Applicability to the Tibetan-Himalayan Orogen

A dissertation submitted in partial satisfaction of the requirements for the degree Doctor of Philosophy in Geology

by

Ellen Wright Alexander

2020

ABSTRACT OF THE DISSERTATION

Geochemical tracers of crustal thickness and their applicability to the Tibetan-Himalayan Orogen

by

Ellen Wright Alexander

Doctor of Philosophy in Geology

University of California, Los Angeles, 2020

Professor Timothy Mark Harrison, Chair

Tectonic models of continental orogens seek to reconstruct the deformation processes associated with large-scale continental collision events. Geographically broad field surveys provide two spatial dimensions, and geochronology provides a third temporal dimension. The missing fourth dimension, most critical to understanding crustal evolution throughout collision, is the crustal thickening history of the orogen. Over the past few decades, however, accurate methods for estimating crustal thickness from the rock record have not fully emerged. Recently, indirect proxies for Moho depth have been developed using whole rock composition: trace element ratios Sr/Y, La/Yb, and Gd/Yb, and stable Nd isotopes. While these proxies can show changes in apparent depth based on transitions in whole-rock chemistry, these proxies are not immune to unconstrained effects on composition, including source melt composition and phase relations, or systematic changes in the intensive variables controlling the proxy. The application of an accurate and precise empirical thermobarometer to plutonic rocks can provide the depth of

magma generation and assimilation, and thus the minimum depth of the Moho and thickness of the crust. The Gangdese batholith in southern Tibet, spanning ca. 200 Ma of pre- and syn-orogenic history, provides a continuous record of silicic magmatism associated with the subduction and collision history of southern Tibet. This work reconstructs whole-rock and zircon P-T-X-t histories of Gangdese granitoids spanning 225 Ma – 18 Ma from a transect of plutons 0 – 110km north of the Indus-Tsangpo Suture, the southern margin of Eurasia, near Lhasa, Tibet at 92ºE. I compare the utility of indirect geochemical proxies and thermobarometry, and discuss the relationship between the thermo-chemical histories of complex plutonic growth processes, and crustal thickening during orogenesis. High-resolution in-situ thermobarometry of quartz inclusions in zircon suggest rapid crustal thickening began ca. 25 Ma earlier than indicated by indirect isotopic and geochemical proxies. Pluton formation occurred throughout the lower three-quarters of the Tibetan Crust, representing a large zone of plutonic activity that weakened the lower crust and contributed significantly to total orogenic heat budget. These results provide constraints for geodynamic models of intracontinental deformation and reveal the limitations and utility of various barometers and pseudobarometers in granites.

The dissertation of Ellen Wright Alexander is approved.

Craig Manning

Kevin McKeegan

An Yin

Timothy Mark Harrison, Committee Chair

TABLE OF CONTENTS

LIST OF FIGURES

ACKNOWLEDGMENTS

"Never forget what you are, for surely the world will not. Make it your strength. Then it can never be your weakness. Armor yourself in it, and it will never be used to hurt you"

- Tyrion Lannister

I am eternally grateful for the people who have been my shipmates on this long voyage. To my parents Carie and Bruce: for their endless support; for the late-night calls and reassuring texts; for the healing visits and the reminders of who I am and why that matters. To my siblings, Graeme and Susan, for levity and for reminding me of the value of family across time and space. To my grandparents, Chan and Chris Young, for their support and encouragement all my life. To Peter: my eye of the storm, my island in a raging sea, my accomplice and coach and foundation through these years. We really did it. To my friends and colleagues: Mélanie Barboni, for all the support, advice, and counsel; Kaitlyn McCain, for the commiseration and camaraderie for these five years; Heather Kirkpatrick, for the coffee breaks and venting sessions and midwestern charm; Beth Ann Bell, for the advice and guidance in all things SIMS; Daniel Fineman, for friendship and solidarity as a fellow lover of the outdoors; and to the rest of the grad students in EPSS for their camaraderie in my time in the department. I am thankful for the mentorship I have received from so many people, both formally and informally. Thank you to my advisor, Mark Harrison, for teaching me how to be a good scientist. Thank you to my committee members: Craig Manning, for teaching me rigorous petrology; Kevin McKeegan, for sharing wisdom in all things geochemistry and academia; An Yin, for encouraging the synthesis of structural geology and geochemistry. Thank you to Abby Kavner, for showing me how to be a compassionate mentor, an engaged teacher, and a lover of science; I could not have done this thing without your

presence and support. To my Mineralogy and Igneous Petrology students, whose enthusiasm for learning has been so inspiring. To Sarah Crump, for inspiring me to be a geologist and helping me grow into the woman I am today. To Dustin Trail, for advice, commiseration, and kindness. To Lauri Holbrook, for enthusiasm and all our fun, informative chats. To the community of scientists, online and in person, who are working toward a kinder, more inclusive future in academia. You give me strength and hope.

I am eternally grateful to Dr. Rochelle Karapetian, who helped me to trust myself, love myself, and have courage in the face of adversity. I am so happy to have been able to be a part of Big Bear Mountain Patrol during my time in grad school; my days on the hill were a literal breath of fresh air and a reminder of the value of *cure d'air* and of community. Thank you to Andrea Stewart, Darren Church, Dave Nelson, Dan Napier, Palmer Thornton, Kyle McElfish, and all my other fellow patrollers for a wonderful and fun escape. During my time in grad school I have been knee-deep in powder, data, zircons, and work. Here's to a future of geology, skiing, and community.

CURRICULUM VITAE

Ellen W. Alexander

EDUCATION

University of California, Los Angeles — Fall 2015 – Winter 2020
PhD Candidate, Geology
Candidacy Exam, April 2019
Qualifying Exam, March 2017

Wesleyan University — Fall 2011 – Spring 2014
B.A., Earth & Environmental Sciences

AWARDS AND GRANTS

EPSS Excellence in Teaching Award	2016, 2017, 2019
MGPV Division GSA travel grant	2019
2nd Place Talk, L.A. Basin Student Research Symposium	2018
EPSS Departmental Quarterly Fellowship	2017
Honors in Earth & Environmental Sciences	2014
Hughes Summer Fellowship, Wesleyan University	2013

PUBLICATIONS

Alexander, E.W., 2014. Aqueous geochemistry of an active magmato-hydrothermal system: Copahue Volcano, Río Ágrio, and Lake Caviahue, Neuquén, Argentina. Undergraduate Honors Thesis, Wesleyan University.

Tang, F., Taylor, R., Einsle, J., Borlina, C., Fu, R., Weiss, B., Williams, H., Williams, W., Nagy, L., Midgley, P., Lima, E., Bell, E., Harrison, M., Alexander, E.W., and Harrison, R., 2019. Secondary magnetite in ancient zircon precludes analysis of a Hadean geodynamo. Proceedings of the National Academy of Sciences, 116(2), pp.407-412.

Alexander, E.W., Wielicki, M.M., Harrison, T.M., DePaolo, D.J., Zhu, D.C., and Zhao, Z., 2019, Hf and Nd Isotopic Constraints on Pre- and Syn-collisional Crustal Thickening of Southern Tibet. JGR-Solid Earth, 124, pp.11,038-11,054..

Borlina, C., Weiss, B., Lima, E., Tang, F., Taylor, R., Einsle, J., Harrison, R., Fu, R., Bell, E., Alexander, E.W., Kirkpatrick, H., Wielicki, M., Harrison, M., Ramezani, J., and Maloof, A., 2020. Re-evaluating the Evidence for a Hadean-Eoarchean Dynamo: *Science Advances*.

Keisling, B., Bryant, R., Golden, N., Stevens, L., and Alexander, E.W., 2020. Does our Vision of Diversity Reduce Harm and Promote Justice? *In review at GSA Today: Groundwork.*

PLANNED MANUSCRIPTS

Alexander, E.W., Yamamoto-Hillman, C., Wielicki, M., and Harrison, T.M. (in prep). Ti-in-quartz and zircon thermobarometry reveal rapid crustal thickening at the onset of the India-Asia Collision.

Alexander, E.W. and Harrison, T.M. (in prep). Limitations to crustal thickness estimates using

La/Yb, Gd/Yb, and Sr/Y.

Alexander, E.W., Lovera, O., and Harrison, T.M. (in prep). Thermochemical modeling of pluton emplacement: implications for assimilation and fractional crystallization processes.

SELECTED PRESENTATIONS

Alexander, E.W.*, Wielicki, M., Harrison, T.M., Lovera, O. and DePaolo, D., 2016, February. Accessing the Fourth Dimension In Orogenic Reconstruction Using Granitoid Thermobarometry. In AGU Fall Meeting Abstracts.

Alexander, E.W., Harrison, T.M., Wielicki, M., Lovera, O., DePaolo, D. and Yamamoto-Hillman, C., 2017, December. Crustal Thickening History of Southern Tibet Revealed with Titanium-in-Quartz Barometry, Zircon Ti-thermometry, and Zircon U-Pb geochronology. In AGU Fall Meeting Abstracts.

Alexander, E.W.*, Yamamoto-Hillman, C., and Harrison, T.M., 2019, August. TitaniQ Inclusions: Thermobarometry of Tibetan Lhasa Block Granitoid Zircons. Goldschmidt2019, Barcelona, Spain.

Alexander, E.W., Yamamoto-Hillman, C., Wielicki, M., and Harrison, T.M., 2019, September. Understanding oxygen isotopes of zircon inclusions: A case study of quartz inclusions in Tibetan granitoid zircons. Geological Society of America Abstracts with Programs, v. 51, n. 5

Alexander, E.W.* and Harrison, M., 2019, December. Do La/Yb and Sr/Y always reflect crustal thickness in magmatic rocks? In AGU Fall Meeting Abstracts.

(* *oral presentation*)

– Chapter 1 –
Introduction

1.1 Motivation

Tectonic models of continental orogens seek to reconstruct the deformation processes associated with large-scale continental collision events (e.g. Dewey & Burke, 1973; Houseman & England, 1993; Kapp et al., 2007; van Hinsbergen et al., 2012). Historically this has been achieved through a combination of conceptual geophysical models (e.g. Beaumont et al., 1996; Royden et al., 1997; Burov & Yamato, 2008; Duretz & Gerya, 2013) and analog experiments (e.g. Tapponnier et al., 1982; Peltzer & Tapponnier, 1988), as well as field investigations (e.g. Kidd et al., 1988; Murphy et al., 1997; Yin et al., 1999; Kapp et al., 2000). Geodynamic models of orogenic processes do not offer standalone explanations for deformation histories; rather they must base their boundary conditions and deformation mechanisms on empirical evidence of the four-dimensional (time – area – depth) progression of collision and orogeny. Geographically broad field surveys can provide two spatial dimensions, and geochronology provides a third, temporal dimension. The missing fourth dimension, critical to understanding crustal evolution throughout collision, is the crustal thickening history of the orogen.

More than 30 years after the classic tectonic models for the Tibetan-Himalayan orogen were formulated (Houseman et al., 1981; England & McKenzie, 1982; Tapponnier et al., 1982; England & Houseman, 1986), no direct test has yet been devised to reconstruct the crustal thickness of Southern Tibet prior to, during, or shortly after the onset of the India-Asia collision. The approximate magnitude of northward crustal shortening since the onset of collision is approximately 1400 km (Yin & Harrison, 2000), but the exact mechanism of crustal thickening and the accommodation of deformation has been vigorously debated (England & Houseman, 1986; Peltzer & Tapponnier, 1988; Kong & Bird, 1995; Peltzer & Saucier, 1996; Kong et al., 1997; Ingalls et al., 2016). That these models imply vastly different crustal thickness histories

underscores how little we know of this evolution. Geochemical and structural studies of exposed units are essential for complete understanding of collision history. Neotectonic, structural and thermochronologic investigations provide useful proxies to understand the behavior of the Tibetan crust throughout collision (Yin & Harrison, 2000; and references therein), but indirect geochemical proxies toward a geographically broad understanding of crustal thickness in Tibet are emerging (e.g., Zhu et al., 2017; Chen et al., 2018; DePaolo et al., 2019). However, these proxies can produce potentially misleading results due to unconstrained parameters that modify geochemical signals associated with crustal thickness–see Ch. 3. The integration of geochronology and direct thermobarometers with these indirect geochemical crustal thickness proxies can potentially produce a more accurate four-dimensional reconstruction of the Tibetan crust through 3-D space and time.

1.2 Tectonic Background

The Tibetan-Himalayan Orogen broadly encompasses the mountain belt stretching from Tajikistan to the northern Yunnan province, China; and from northern India to Xinjiang and Gansu, China. In total, the orogen represents nearly five million km^2 of land area, mostly contained within southern Eurasia and the northern Indian subcontinent. The modern Tibetan plateau is a jigsaw of several accreted terranes, which were sequentially sutured onto southern Eurasia beginning in the early Paleozoic, with the final suturing event at the onset of the India-Asia collision. The Eurasian portion of the Tibetan plateau is comprised of three major terranes: the Songpan-Ganze terrane in northern Tibet, the Qiangtang terrane in central Tibet, and the Lhasa terrane in southern Tibet; the Himalayan terrane, belonging to the northern Indian subcontinent, bounds the Lhasa terrane to the south (**Figure 1.1**). The Himalayan terrane was sutured to the Lhasa block along the Indus-Tsangpo Suture (ITS, alternately called the Yarlung-

Tsangpo or Indus-Yarlung suture) at the onset of the India-Asia collision at approximately 57 Ma (Leech et al., 2005).

As this work focuses on the magmatic and tectonic evolution of the southernmost portion of the Lhasa terrane, this introduction will focus on the precollisional history of the Lhasa terrane, particularly the southernmost portion. The Lhasa terrane is a microcontinent that rifted away from the Gondwana supercontinent, beginning approximately 250 Ma with the opening of the Neo-Tethys ocean basin by back-arc extension (Zhu et al., 2011). For the following ca. 100

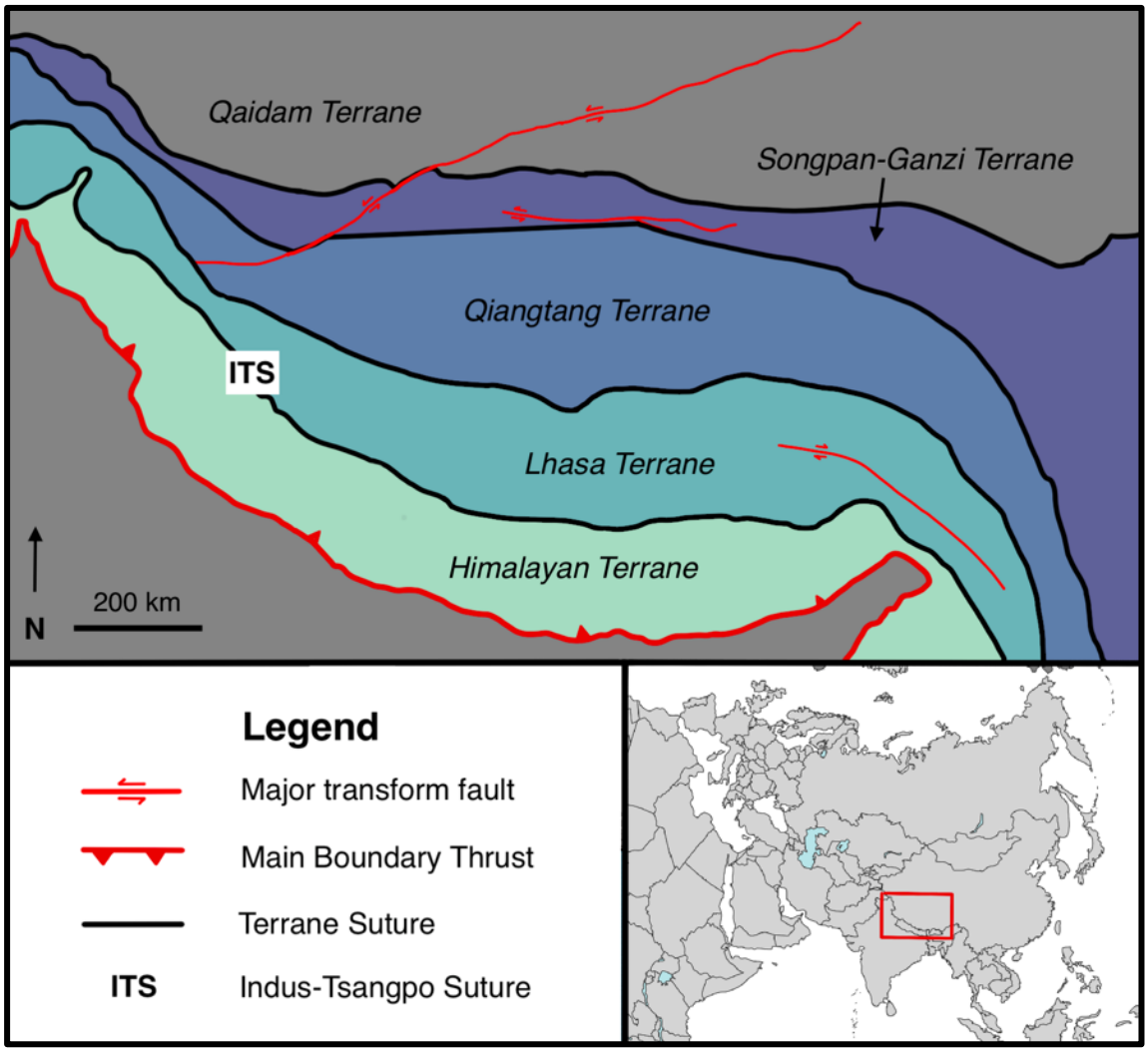

Figure 0.1: Schematic figure of terranes of the Tibetan plateau. The boundary between Eurasia and India is marked by the Indus-Tsangpo Suture (ITS). The studies in the following chapters focus on magmatic rocks from the Lhasa Terrane.

Ma, Lhasa rifted away from what would later become the Indian subcontinent, with continued spreading of the Neo Tethys basin to the south, and subduction of the Bangong-Nujiang Tethys ocean basin to the north. In the Late Jurassic the Lhasa terrane began a protracted collision with the Qiangtang terrane to the north, with collision and suturing progressing from east to west until the Middle Cretaceous (Dewey et al., 1988; Gaetani et al., 1993; Matte et al., 1996). Following completed suturing of Lhasa to Qiangtang along the Bangong-Nujiang suture zone, Lhasa underwent continued north-south shortening until the Late Cretaceous, with approximately 180 km of total internal shortening between its collision with Qiangtang and the onset of the India-Asia collision approximately 70 million years later (Murphy et al., 1997).

Following the Lhasa-Qiangtang collision, the Neo-Tethyan ocean began to subduct under the formerly passive southern margin of Lhasa at approximately 140 Ma (Niu et al., 2003; Zhu et al., 2011). Though there has been continuous magmatic activity in the Lhasa terrane since at least 225 Ma to the present (Chapman & Kapp, 2017; Alexander et al., 2019), the onset of Gangdese Batholith magmatism heralded the commencement of Neo-Tethys subduction. Gangdese magmatic rocks are broadly characterized by juvenile calc-alkaline I-type granitoids and intermediate to felsic arc volcanics, with the most voluminous magmatism likely occurring between ca. 100 – 80 Ma and again between 65 – 45 Ma (Wen et al., 2008; Zhu et al., 2015). The Gangdese Batholith, stretching ca. 2000 km along the entire southern margin of the Lhasa terrane, witnessed the tectonic and thermal effects of continental collision; the geochemistry of its plutonic units record the evolving geologic environment as the India-Asia collision progressed. These granitoids record the evolving crustal structure of the Lhasa terrane, providing a window into the nature and mechanism of collision. The temperature, pressure, and regional tectonic conditions present during granite magmatism inform the geochemistry and

thermobarometry of Gangdese Batholith granitoids, which can then be used to constrain the long-uncertain mechanisms of the 1000's of km of crustal deformation and shortening following the onset of the India-Asia collision.

1.3 Accommodating Collision-Induced Shortening

Structural and geochemical studies of the Tibetan-Himalayan orogen reveal a complex history of deformation and magmatic evolution, from Andean-type subduction to post-collisional pluton emplacement in a significantly thickened crust (Yin and Harrison, 2000). Accommodation of this shortening can include intracrustal deformation, including development of upper-crustal fold-thrust belts or lateral extension; intracontinental subduction; erosion and consumption of the overriding lithosphere by the downgoing plate; and lateral extrusion of rigid crustal blocks or ductile lower crust. The relative impact of these various shortening-induced deformation mechanisms, however, is not well understood. Many have argued that the collision zone thickened to its present state via uniformly distributed shortening (England & McKenzie, 1982; England & Houseman, 1986; Dewey et al., 1988; Royden et al., 1997). The "distributed shortening" (simple-shear thickening) model, initially introduced by Dewey & Bird (1970) and reiterated more recently (e.g. Beaumont et al., 1996; Royden et al., 1997; Shen et al., 2001), often assumes a low-elevation, relatively thin Tibetan crust at the onset of collision. Distributed shortening models simulate substantial deformation of the Tibetan upper crust; even with decoupling of the upper and lower crust, which could accommodate crustal flow, models still generate significant upper crustal deformation. The presence of essentially undeformed late-Cretaceous/Early Cenozoic volcanics (Murphy et al., 1997) in Southern Tibet implies models of this type cannot fully explain the uplift and shortening history of the Tibetan Plateau. Rather Tibet had already been significantly shortened and thickened prior to collision (Murphy et al.,

1997) and did not experience upper crustal shortening during the initial stages of collision (Harrison et al., 1992).

Crustal extrusion, on the other hand, is a process by which the lithosphere is fractured and discrete blocks are extruded laterally away from the indenter, with displacement accommodated either by large-scale strike-slip faults (Peltzer & Tapponnier, 1988; Tapponnier et al., 2001) or by pure shear along a mosaic of slip lines whose location changes as collision progresses (Molnar & Tapponnier, 1975; Tapponnier & Molnar, 1976). Analog experiments conducted by Peltzer and Tapponnier (1988) used several model crustal structures: vertical layers either perpendicular to or parallel to the indenter's velocity, as well as homogeneous blocks. The model with preexisting perpendicular structures most closely mimics the reconstructed displacements and modern strike-slip faults in Tibet and Indochina; there is additionally minimal deformation within the discrete blocks as fracturing and shearing proceeds. The experimental results agree with regional neotectonics, but it is not clear that crustal extrusion was the dominant form of accommodation throughout the entire India-Asia collision. The fundamental distinction between the distributed shortening and crustal extrusion endmember models is whether shortening was accommodated primarily through intracrustal deformation or lateral displacement, respectively. It is estimated that between ~32 and 16 Ma, plate convergence became increasingly accommodated by eastward extrusion, either as translation of the Indochina and South China Blocks (Tapponnier et al., 1982; Harrison et al., 1996) or as ductile flow of underlying material (Bird, 1991).

1.4 The Role of Igneous Geochemistry

Over the past 40 years, intensive structural, geochemical, and thermochronological efforts in the Tibetan orogen have laid the groundwork for a comprehensive understanding of

this mountain belt, but key issues remain unresolved. In the case of continental orogens with voluminous magmatic inflation, like southern Tibet, the chemistry of igneous rocks in the region, and their constituent minerals, may provide better constraints on minimum crustal thicknesses than metamorphic rocks, which are susceptible to disequilibrium processes that may confound the use of thermodynamic methods. In recent years, however, accurate methods for estimating crustal thickness from igneous rocks have not fully emerged. Major element cation exchange barometers such as the Al-in-hornblende barometer (Hammarstrom & Zen, 1986; Schmidt, 1992; Anderson & Smith, 1995; Ague, 1997; Mutch et al., 2016) are limited to a narrow range of phase assemblages and appear to, at best, record emplacement depth rather than depth of melting (Ague, 1997; Alexander et al., 2016; Mutch et al., 2016), and at worst are highly susceptible to closure effects and deuteric alteration (Agemar et al., 1999). More recently, indirect proxies for Moho depth have been developed using whole rock composition: trace element ratios Sr/Y and La/Yb (Chiaradia, 2015; Profeta et al., 2015; Farner & Lee, 2017; Hu et al., 2017; Lieu & Stern, 2019), and Nd isotopes (DePaolo et al., 2019). Chapter 2 explores the use of Hf isotopes in this role and concludes that granitoids in the southern margin of Tibet do not indicate significant assimilation with old crustal material until after the onset of collision. When the thermoisotopic model of DePaolo et al. (2019) is modified for Hf isotopes, calculated apparent depths suggest a relatively thin margin in southern Lhasa until < 50 Ma. Chapter 3 offers a critique of the trace element ratio methods (i.e., Sr/Y, La/Yb, and Gd/Yb) for establishing depth histories; a case study of 336 igneous samples from southern Lhasa age 40–100 Ma demonstrates the unreliability of trace element depth proxies. While chemical and isotopic proxies can show changes in apparent depth based on geochemical transitions, they are not immune to unconstrained effects on composition, such as changing source melt composition and phase relations, or systematic

changes in the intensive variables controlling the proxy (Moyen, 2009). Ironically these changes may be caused by the very crustal thickening that these proxies attempt to track, resulting in unresolvable drift in the baseline assumptions used to implement these proxies (Farner & Lee, 2017; c.f. Hu et al., 2017).

It is clear that direct thermobarometry would be an improvement on compositionally dependent, indirect Moho depth proxies. The application of an accurate and precise empirical thermobarometer to plutonic rocks can provide the depth of magma generation and assimilation, and thus the minimum depth of the Moho and thickness of the crust. Titanium partitioning in zircon and quartz is particularly useful, as it is a fixed charge cation that is universally available in magmatic rocks, compatible in zircon and quartz in trace amounts, and resistant to diffusive resetting at subsolidus temperature (T) and pressure (P) (Cherniak et al., 1997, 2007). Experimental studies have calibrated the T dependency of [Ti] in zircon (Watson & Harrison, 2005; Ferry & Watson, 2007), and the T and P dependency of [Ti] in quartz (Thomas et al., 2010, 2015). One caveat to the paired use of these thermobarometers is the assumption that the zircon and quartz crystallized during the same stage of magma genesis, under thermodynamic equilibrium. Analyses of Ti concentration of quartz inclusions in zircon, as well as the Ti concentration of the adjacent zircon growth zone, allows for simultaneous solution for T and P. Oxygen isotopic analyses of inclusion-host pairs can test thermodynamic equilibrium isotopic fractionation (Trail et al., 2007; Alexander et al., 2019).

The Tibetan-Himalayan orogen presents a natural laboratory to apply these paired thermobarometers to reconstruct crustal thicknesses at the India-Asia margin throughout collision. In Southern Tibet, there are hundreds of granitic plutons spanning ~200 Ma and 1000's of km^2; the petrology of these plutons provides a window into the spatiotemporal history of

magmatic processes throughout the India-Asia collision. Chapter 4 describes a promising feasibility study of titanium thermobarometry on Tibetan granites and suggests it can be a robust technique for accessing the depth of melt generation throughout the India-Asia collision. Chapter 5 synthesizes the results of Chs. 2–4: thermobarometry results inform the reliability of indirect thermoisotopic and geochemical models, showing the challenges in relying on indirect proxies. The robustness of a proxy is governed, in part, by its mutability by unconstrained parameters; in Ch. 5 I recommend future methods to test parameter sensitivity in order to deconvolve crustal thickness information from complex geochemical systems.

1.5 References

Agemar, T., Wörner, G., & Heumann, A. (1999). Stable isotopes and amphibole chemistry on hydrothermally altered granitoids in the North Chilean Precordillera: a limited role for meteoric water? *Contributions to Mineralogy and Petrology*, *136*(4), 331–344. https://doi.org/10.1007/s004100050542

Ague, J. J. (1997). Thermodynamic calculation of emplacement pressures for batholithic rocks, California: Implications for the aluminum-in-hornblende barometer. *Geology*, *25*(6), 563–566. https://doi.org/10.1130/0091-7613(1997)025<0563:TCOEPF>2.3.CO;2

Alexander, E. W., Wielicki, M. M., Harrison, T. M., Lovera, O. M., & Depaolo, D. J. (2016, December). *Accessing the fourth dimension in orogenic reconstruction using granitoid thermobarometry*. Abstracts with Programs presented at the AGU Fall Meeting 2016, Moscone Center. Retrieved from https://agu.confex.com/agu/fm16/meetingapp.cgi/Paper/162115

Alexander, E. W., Harrison, M., Wielicki, M. M., Lovera, O. M., DePaolo, D. J., & Yamamoto-Hillman, C. A. (2017). Crustal Thickening History of Southern Tibet Revealed with

Titanium-in-Quartz Barometry, Zircon Ti-thermometry, and Zircon U-Pb geochronology. *AGU Fall Meeting Abstracts*, *43*. Retrieved from http://adsabs.harvard.edu/abs/2017AGUFM.V43A0523A

Alexander, E. W., Wielicki, M. M., Harrison, T. M., DePaolo, D. J., Zhao, Z.-D., & Zhu, D.-C. (2019). Hf and Nd Isotopic Constraints on Pre- and Syn-collisional Crustal Thickness of Southern Tibet. *Journal of Geophysical Research: Solid Earth*, *124*, 11038–11054. https://doi.org/10.1029/2019JB017696

Alexander, E. W., Yamamoto-Hillman, C. A., & Harrison, T. M. (2019). Understanding oxygen isotopes of zircon inclusions: a case study of quartz inclusions in Tibetan granitoid zircons. Presented at the GSA Annual Meeting in Phoenix, Arizona, USA - 2019, GSA. Retrieved from https://gsa.confex.com/gsa/2019AM/webprogram/Paper339224.html

Anderson, J. L., & Smith, D. R. (1995). The effects of temperature and fO_2 on the Al-in-hornblende barometer. *American Mineralogist*, *80*(5–6), 549–559. https://doi.org/10.2138/am-1995-5-615

Beaumont, C., Ellis, S., Hamilton, J., & Fullsack, P. (1996). Mechanical model for subduction-collision tectonics of Alpine-type compressional orogens. *Geology*, *24*(8), 675–678. https://doi.org/10.1130/0091-7613(1996)024<0675:MMFSCT>2.3.CO;2

Bird, P. (1991). Lateral extrusion of lower crust from under high topography in the isostatic limit. *Journal of Geophysical Research: Solid Earth*, *96*(B6), 10275–10286. https://doi.org/10.1029/91JB00370

Bohrson, W. A., & Spera, F. J. (2001). Energy-Constrained Open-System Magmatic Processes II: Application of Energy-Constrained Assimilation–Fractional Crystallization (EC-AFC)

Model to Magmatic Systems. *Journal of Petrology*, *42*(5), 1019–1041. https://doi.org/10.1093/petrology/42.5.1019

Bohrson, W. A., & Spera, F. J. (2003). Energy-constrained open-system magmatic processes IV: Geochemical, thermal and mass consequences of energy-constrained recharge, assimilation and fractional crystallization (EC-RAFC). *Geochemistry, Geophysics, Geosystems*, *4*(2). https://doi.org/10.1029/2002GC000316

Burov, E., & Yamato, P. (2008). Continental plate collision, P–T–t–z conditions and unstable vs. stable plate dynamics: Insights from thermo-mechanical modelling. *Lithos*, *103*(1), 178–204. https://doi.org/10.1016/j.lithos.2007.09.014

Chapman, J. B., & Kapp, P. (2017). Tibetan Magmatism Database. *Geochemistry, Geophysics, Geosystems*, *18*(11), 4229–4234. https://doi.org/10.1002/2017GC007217

Chen, J.-L., Yin, A., Xu, J.-F., Dong, Y.-H., & Kang, Z.-Q. (2018). Late Cenozoic magmatic inflation, crustal thickening, and >2 km of surface uplift in central Tibet. *Geology*, *46*(1), 19–22. https://doi.org/10.1130/G39699.1

Cherniak, D. J., Hanchar, J. M., & Watson, E. B. (1997). Diffusion of tetravalent cations in zircon. *Contributions to Mineralogy and Petrology*, *127*(4), 383–390. https://doi.org/10.1007/s004100050287

Cherniak, D. J., Watson, E. B., & Wark, D. A. (2007). Ti diffusion in quartz. *Chemical Geology*, *236*(1), 65–74. https://doi.org/10.1016/j.chemgeo.2006.09.001

Chiaradia, M. (2015). Crustal thickness control on Sr/Y signatures of recent arc magmas: an Earth scale perspective. *Scientific Reports*, *5*, 8115. https://doi.org/10.1038/srep08115

DePaolo, D. J., Harrison, T. M., Zhao, Z., Zhu, D.-C., & Mo, X. (2019). Geochemical evidence

for the pre- and post-collisional crustal thickness history of Southern Tibet. *Gondwana Research*.

DePaolo, Donald J., Perry, F. V., & Baldridge, W. S. (1992). Crustal versus mantle sources of granitic magmas: a two-parameter model based on Nd isotopic studies. *Earth and Environmental Science Transactions of The Royal Society of Edinburgh*, *83*(1–2), 439–446. https://doi.org/10.1017/S0263593300008117

Dewey, J.F., Shackleton, R. M., Chang, C., & Sun, Y. (1988). The tectonic evolution of the Tibetan Plateau. *Philosophical Transactions of the Royal Society of London. Series A, Mathematical and Physical Sciences*, *327*(1594), 379–413. https://doi.org/10.1098/rsta.1988.0135

Dewey, John F., & Bird, J. M. (1970). Mountain belts and the new global tectonics. *Journal of Geophysical Research (1896-1977)*, *75*(14), 2625–2647. https://doi.org/10.1029/JB075i014p02625

Dewey, John F., & Burke, K. C. A. (1973). Tibetan, Variscan, and Precambrian Basement Reactivation: Products of Continental Collision. *The Journal of Geology*, *81*(6), 683–692. https://doi.org/10.1086/627920

Duretz, T., & Gerya, T. V. (2013). Slab detachment during continental collision: Influence of crustal rheology and interaction with lithospheric delamination. *Tectonophysics*, *602*, 124–140. https://doi.org/10.1016/j.tecto.2012.12.024

England, P., & Houseman, G. (1986). Finite strain calculations of continental deformation: 2. Comparison with the India-Asia Collision Zone. *Journal of Geophysical Research: Solid*

Earth, *91*(B3), 3664–3676. https://doi.org/10.1029/JB091iB03p03664

England, P., & McKenzie, D. (1982). A thin viscous sheet model for continental deformation. *Geophysical Journal of the Royal Astronomical Society*, *70*(2), 295–321. https://doi.org/10.1111/j.1365-246X.1982.tb04969.x

Farner, M. J., & Lee, C.-T. A. (2017). Effects of crustal thickness on magmatic differentiation in subduction zone volcanism: A global study. *Earth and Planetary Science Letters*, *470*, 96–107. https://doi.org/10.1016/j.epsl.2017.04.025

Ferry, J. M., & Watson, E. B. (2007). New thermodynamic models and revised calibrations for the Ti-in-zircon and Zr-in-rutile thermometers. *Contributions to Mineralogy and Petrology*, *154*(4), 429–437. https://doi.org/10.1007/s00410-007-0201-0

Gaetani, M., Jadoul, F., Erba, E., & Garzanti, E. (1993). Jurassic and Cretaceous orogenic events in the North Karakoram: age constraints from sedimentary rocks. *Geological Society, London, Special Publications*, *74*(1), 39–52. https://doi.org/10.1144/GSL.SP.1993.074.01.04

Hammarstrom, J. M., & Zen, E. (1986). Aluminum in hornblende: an empirical igneous geobarometer. *American Mineralogist*, *71*(11–12), 12971313.

Harrison, T. Mark, Copeland, P., Kidd, W. S. F., & Yin, A. (1992). Raising Tibet. *Science*, *255*(5052), 1663–1670. https://doi.org/10.1126/science.255.5052.1663

Harrison, T.M., Leloup, P. H., Ryerson, F. J., Tapponnier, P., Lacassin, R., & Chen, W. (1996). Diachronous initiation of transtension along the Ailao Shan-Red River shear zone, Yunnan and Vietnam. In *Tectonic Evolution of Asia* (pp. 208–226). Cambridge

University Press.

van Hinsbergen, D. J. J. van, Lippert, P. C., Dupont-Nivet, G., McQuarrie, N., Doubrovine, P. V., Spakman, W., & Torsvik, T. H. (2012). Greater India Basin hypothesis and a two-stage Cenozoic collision between India and Asia. *Proceedings of the National Academy of Sciences*, *109*(20), 7659–7664. https://doi.org/10.1073/pnas.1117262109

Houseman, G., & England, P. (1993). Crustal thickening versus lateral expulsion in the Indian-Asian continental collision. *Journal of Geophysical Research: Solid Earth*, *98*(B7), 12233–12249. https://doi.org/10.1029/93JB00443

Houseman, G. A., McKenzie, D. P., & Molnar, P. (1981). Convective instability of a thickened boundary layer and its relevance for the thermal evolution of continental convergent belts. *Journal of Geophysical Research: Solid Earth*, *86*(B7), 6115–6132. https://doi.org/10.1029/JB086iB07p06115

Hu, F., Ducea, M. N., Liu, S., & Chapman, J. B. (2017). Quantifying Crustal Thickness in Continental Collisional Belts: Global Perspective and a Geologic Application. *Scientific Reports*, *7*(1), 1–10. https://doi.org/10.1038/s41598-017-07849-7

Ingalls, M., Rowley, D. B., Currie, B., & Colman, A. S. (2016). Large-scale subduction of continental crust implied by India–Asia mass-balance calculation. *Nature Geoscience*, *9*(11), 848. https://doi.org/10.1038/ngeo2806

Kapp, P., Yin, A., Manning, C. E., Murphy, M., Harrison, T. M., Spurlin, M., et al. (2000). Blueschist-bearing metamorphic core complexes in the Qiangtang block reveal deep crustal structure of northern Tibet. *Geology*, *28*(1), 19–22. https://doi.org/10.1130/0091-

7613(2000)28<19:BMCCIT>2.0.CO;2

Kapp, P., DeCelles, P. G., Gehrels, G. E., Heizler, M., & Ding, L. (2007). Geological records of the Lhasa-Qiangtang and Indo-Asian collisions in the Nima area of central Tibet. *GSA Bulletin*, *119*(7–8), 917–933. https://doi.org/10.1130/B26033.1

Kidd, W. S. F., Yusheng, P., Chengfa, C., Coward, M. P., Dewey, J. F., Gansser, A., et al. (1988). Geological mapping of the 1985 Chinese—British Tibetan (Xizang—Qinghai) Plateau Geotraverse route. *Phil. Trans. R. Soc. Lond. A*, *327*(1594), 287–305. https://doi.org/10.1098/rsta.1988.0130

Kong, X., Yin, A., & Harrison, T. M. (1997). Evaluating the role of preexisting weaknesses and topographic distributions in the Indo-Asian collision by use of a thin-shell numerical model. *Geology*, *25*(6), 527–530. https://doi.org/10.1130/0091-7613(1997)025<0527:ETROPW>2.3.CO;2

Kong, Xianghong, & Bird, P. (1995). SHELLS: A thin-shell program for modeling neotectonics of regional or global lithosphere with faults. *Journal of Geophysical Research: Solid Earth*, *100*(B11), 22129–22131. https://doi.org/10.1029/95JB02435

Leech, M. L., Singh, S., Jain, A. K., Klemperer, S. L., & Manickavasagam, R. M. (2005). The onset of India–Asia continental collision: Early, steep subduction required by the timing of UHP metamorphism in the western Himalaya. *Earth and Planetary Science Letters*, *234*(1), 83–97. https://doi.org/10.1016/j.epsl.2005.02.038

Lieu, W. K., & Stern, R. J. (2019). The robustness of Sr/Y and La/Yb as proxies for crust thickness in modern arcs. *Geosphere*, *15*(3), 621–641.

https://doi.org/10.1130/GES01667.1

Lovera, O. M., Harrison, M., Schmitt, A. K., Wielicki, M. M., & Tierney, C. R. (2015). Numerical Simulation of Magma Reservoirs to Interpret Chrono-Chemical Signal. *AGU Fall Meeting Abstracts*, *43*. Retrieved from http://adsabs.harvard.edu/abs/2015AGUFM.V43B3156L

Matte, Ph., Tapponnier, P., Arnaud, N., Bourjot, L., Avouac, J. P., Vidal, Ph., et al. (1996). Tectonics of Western Tibet, between the Tarim and the Indus. *Earth and Planetary Science Letters*, *142*(3), 311–330. https://doi.org/10.1016/0012-821X(96)00086-6

Molnar, P., & Tapponnier, P. (1975). Cenozoic Tectonics of Asia: Effects of a Continental Collision. *Science*, *189*(4201), 419–426.

Moyen, J.-F. (2009). High Sr/Y and La/Yb ratios: The meaning of the "adakitic signature." *Lithos*, *112*(3), 556–574. https://doi.org/10.1016/j.lithos.2009.04.001

Murphy, M. A., Yin, A., Harrison, T. M., Dürr, S. B., Chen, Z., Ryerson, F. J., et al. (1997). Did the Indo-Asian collision alone create the Tibetan plateau? *Geology*, *25*(8), 719–722. https://doi.org/10.1130/0091-7613(1997)025<0719:DTIACA>2.3.CO;2

Mutch, E. J. F., Blundy, J. D., Tattitch, B. C., Cooper, F. J., & Brooker, R. A. (2016). An experimental study of amphibole stability in low-pressure granitic magmas and a revised Al-in-hornblende geobarometer. *Contributions to Mineralogy and Petrology*, *171*(10), 85. https://doi.org/10.1007/s00410-016-1298-9

Niu, Y., O'hara, M. J., & Pearce, J. A. (2003). Initiation of Subduction Zones as a Consequence of Lateral Compositional Buoyancy Contrast within the Lithosphere: a Petrological Perspective. *Journal of Petrology*, *44*(5), 851–866.

https://doi.org/10.1093/petrology/44.5.851

Peltzer, G., & Saucier, F. (1996). Present-day kinematics of Asia derived from geologic fault rates. *Journal of Geophysical Research: Solid Earth*, *101*(B12), 27943–27956. https://doi.org/10.1029/96JB02698

Peltzer, G., & Tapponnier, P. (1988). Formation and evolution of strike-slip faults, rifts, and basins during the India-Asia Collision: An experimental approach. *Journal of Geophysical Research: Solid Earth*, *93*(B12), 15085–15117. https://doi.org/10.1029/JB093iB12p15085

Profeta, L., Ducea, M. N., Chapman, J. B., Paterson, S. R., Gonzales, S. M. H., Kirsch, M., et al. (2015). Quantifying crustal thickness over time in magmatic arcs. *Scientific Reports*, *5*, 17786. https://doi.org/10.1038/srep17786

Royden, L. H., Burchfiel, B. C., King, R. W., Wang, E., Chen, Z., Shen, F., & Liu, Y. (1997). Surface Deformation and Lower Crustal Flow in Eastern Tibet. *Science*, *276*(5313), 788–790. https://doi.org/10.1126/science.276.5313.788

Schmidt, M. W. (1992). Amphibole composition in tonalite as a function of pressure: an experimental calibration of the Al-in-hornblende barometer. *Contributions to Mineralogy and Petrology*, *110*(2), 304–310. https://doi.org/10.1007/BF00310745

Shen, F., Royden, L. H., & Burchfiel, B. C. (2001). Large-scale crustal deformation of the Tibetan Plateau. *Journal of Geophysical Research: Solid Earth*, *106*(B4), 6793–6816. https://doi.org/10.1029/2000JB900389

Spera, F. J., & Bohrson, W. A. (2001). Energy-Constrained Open-System Magmatic Processes I: General Model and Energy-Constrained Assimilation and Fractional Crystallization (EC-

AFC) Formulation. *Journal of Petrology*, *42*(5), 999–1018. https://doi.org/10.1093/petrology/42.5.999

Spera, F. J., & Bohrson, W. A. (2002). Energy-constrained open-system magmatic processes 3. Energy-Constrained Recharge, Assimilation, and Fractional Crystallization (EC-RAFC). *Geochemistry, Geophysics, Geosystems*, *3*(12), 1–20. https://doi.org/10.1029/2002GC000315

Tapponnier, P., Peltzer, G., Dain, A. Y. L., Armijo, R., & Cobbold, P. (1982). Propagating extrusion tectonics in Asia: New insights from simple experiments with plasticine. *Geology*, *10*(12), 611–616. https://doi.org/10.1130/0091-7613(1982)10<611:PETIAN>2.0.CO;2

Tapponnier, Paul, & Molnar, P. (1976). Slip-line field theory and large-scale continental tectonics. *Nature*, *264*(5584), 319–324. https://doi.org/10.1038/264319a0

Tapponnier, Paul, Zhiqin, X., Roger, F., Meyer, B., Arnaud, N., Wittlinger, G., & Jingsui, Y. (2001). Oblique Stepwise Rise and Growth of the Tibet Plateau. *Science*, *294*(5547), 1671–1677. https://doi.org/10.1126/science.105978

Thomas, J. B., Bruce Watson, E., Spear, F. S., Shemella, P. T., Nayak, S. K., & Lanzirotti, A. (2010). TitaniQ under pressure: the effect of pressure and temperature on the solubility of Ti in quartz. *Contributions to Mineralogy and Petrology*, *160*(5), 743–759. https://doi.org/10.1007/s00410-010-0505-3

Thomas, J. B., Watson, E. B., Spear, F. S., & Wark, D. A. (2015). TitaniQ recrystallized: experimental confirmation of the original Ti-in-quartz calibrations. *Contributions to*

Mineralogy and Petrology, *169*(3). https://doi.org/10.1007/s00410-015-1120-0

Trail, D., Mojzsis, S. J., Harrison, T. M., Schmitt, A. K., Watson, E. B., & Young, E. D. (2007). Constraints on Hadean zircon protoliths from oxygen isotopes, Ti-thermometry, and rare earth elements. *Geochemistry, Geophysics, Geosystems*, *8*(6), Q06014. https://doi.org/10.1029/2006GC001449

Watson, E. B., & Harrison, T. M. (2005). Zircon Thermometer Reveals Minimum Melting Conditions on Earliest Earth. *Science*, *308*(5723), 841–844. https://doi.org/10.1126/science.1110873

Wen, D.-R., Liu, D., Chung, S.-L., Chu, M.-F., Ji, J., Zhang, Q., et al. (2008). Zircon SHRIMP U–Pb ages of the Gangdese Batholith and implications for Neotethyan subduction in southern Tibet. *Chemical Geology*, *252*(3), 191–201. https://doi.org/10.1016/j.chemgeo.2008.03.003

Yin, A., & Harrison, T. M. (2000). Geologic Evolution of the Himalayan-Tibetan Orogen. *Annual Review of Earth and Planetary Sciences*, *28*(1), 211–280. https://doi.org/10.1146/annurev.earth.28.1.211

Yin, A., Harrison, T. M., Murphy, M. A., Grove, M., Nie, S., Ryerson, F. J., et al. (1999). Tertiary deformation history of southeastern and southwestern Tibet during the Indo-Asian collision. *GSA Bulletin*, *111*(11), 1644–1664. https://doi.org/10.1130/0016-7606(1999)111<1644:TDHOSA>2.3.CO;2

Zhu, D.-C., Zhao, Z.-D., Niu, Y., Mo, X.-X., Chung, S.-L., Hou, Z.-Q., et al. (2011). The Lhasa Terrane: Record of a microcontinent and its histories of drift and growth. *Earth and*

Planetary Science Letters, *301*(1), 241–255. https://doi.org/10.1016/j.epsl.2010.11.005

Zhu, D.-C., Wang, Q., Zhao, Z.-D., Chung, S.-L., Cawood, P. A., Niu, Y., et al. (2015). Magmatic record of India-Asia collision. *Scientific Reports*, *5*, srep14289. https://doi.org/10.1038/srep14289

Zhu, D.-C., Wang, Q., Cawood, P. A., Zhao, Z.-D., & Mo, X.-X. (2017). Raising the Gangdese Mountains in southern Tibet. *Journal of Geophysical Research: Solid Earth*, *122*(1), 214–223. https://doi.org/10.1002/2016JB013508

– Chapter 2 –
Hf and Nd Isotopic Models

Note: This chapter is modified from Alexander, E. W., Wielicki, M. M., Harrison, T. M., DePaolo, D. J., Zhao, Z.-D., & Zhu, D.-C. (2019). Hf and Nd Isotopic Constraints on Pre- and Syn-collisional Crustal Thickness of Southern Tibet. *Journal of Geophysical Research: Solid Earth*, 124, 11038–11054.

2.1 Introduction

Isotopic signatures of magmatic rocks are governed by the composition of the primary melt source, as well as potential contribution from crustal material subsequently assimilated into the magma. Our interpretations emphasize the role of crustal assimilation in the genesis of granitic magmas, an issue which remains subject to debate (e.g. Chapman et al., 2017); a detailed discussion of the importance of crustal assimilation is given in DePaolo et al. (2019). The temperature of the country rock into which a magma intrudes is the most important limiting factor on the degree of assimilation between the juvenile melt and crustal material (Reiners et al., 1995). In general, cold crust is unlikely to be heated to anatexis by the injection of juvenile melt and thus the melt will not undergo significant alteration of its isotopic signature by assimilation of crustal material, while hot crust will be more readily available for assimilation. When the assimilation rate competes with the rate at which fractional crystallization is occurring, there can be a large crustal contribution to the isotopic signature (DePaolo, 1981; Spera & Bohrson, 2002). Storage at high temperature, whether due to high country rock initial temperature or periodic magma recharge, will result in greater total assimilation and thus a more crustal-like isotopic signature (DePaolo, 1981; Reiners et al., 1995). We proceed on the assumption that higher degrees of assimilation are associated with higher wall-rock temperature and that the majority of melt hybridization occurs at or near the Moho (DePaolo, 1981; Klaver et al., 2018; Rapp et al., 2003; Reiners et al., 1995; DePaolo et al., 2019).

While steady-state magma flux and assimilation cannot be assumed for upper-crustal volcanic systems, in which a large quantity of low-crystallinity magma must be generated prior to eruption (Simon et al., 2014; DePaolo et al., 2019), granitic batholiths are commonly characterized by episodic growth and zircon crystallization histories spanning 10^5 to 10^6 years

(Wiebe & Collins, 1998; McNulty et al., 2000; Walker et al., 2007). Accordingly, typical granitoids form from low magma flux, with the ratio of assimilation rate and recharge rate only slightly lower than steady state. The "Temperature-Flux" model developed by DePaolo et al. (1992; 2019) defines the "Neodymium Crustal Index" (NCI), which relates the whole-rock ε_{Nd} of a pluton to the ε_{Nd} of recharging magma and assimilated (crustal) material, can be used to approximate Moho temperature, and therefore depth, as a function of the pluton's degree of crustal assimilation. DePaolo et al. (2019) use model parameters based on calibrated isotopic studies of layered intrusions (Hammersley and DePaolo, 2006). In open systems it is difficult to constrain the validity of Temperature-Flux model parameters; factors such as cooling rate, pluton volume, and crystallization rate necessarily change during recharge and assimilation in an evolving magma body. The use of this model to reconstruct crustal thickness relies on several assumptions, the most important being the geothermal gradient of the system. The crustal thickness is derived from the calculated Moho temperature and the assumed geothermal gradient; while the paleo-geotherm of Southern Tibet has not been directly reconstructed, other continental arcs have a relatively shallow geothermal gradient in the mid- to lower-crust, consistent with the model geotherm used by DePaolo et al. (2019) (Rothstein and Manning, 2003). Other assumed parameters, including those that address rate of crystallization DePaolo et al. (2019) further demonstrated with a Monte Carlo simulation that the model is relatively robust at predicting NCI and Moho temperature with variation of unconstrained parameters within a geophysically reasonable range.

In this study, we adapt the Temperature-Flux model to the Hf isotopic variation in pre- and syn-collisional granitic zircons, which are resistant to secondary alteration or addition of radiogenic Hf. The Lu-Hf isotopic system behaves similarly to Sm-Nd; the distribution

coefficient ratio during partial melting D_{Lu}/D_{Hf} is approximately twice that of D_{Sm}/D_{Nd}, resulting in greater radiogenic enrichments or depletions of Hf isotopes relative to Nd in derived magmas. Thus, the Lu-Hf system magnifies differential evolution of DM and crustal $^{176}Hf/^{177}Hf$ relative to Sm-Nd. Modern DM is characterized by a maximum $\varepsilon_{Hf} \approx +18$ (Vervoort & Blichert-Toft, 1999, and references therein). As with Nd, the average ε_{Hf} of continental material is dependent on the timing of fractionation of crustal material from DM. Reconstructing crustal evolution using Hf requires a temporal anchor to which isotopic data may be attached. Zircon ($ZrSiO_4$) has proved ideal for constraining not only the age of magmatic rocks of a wide variety of compositions, but also as a record of the thermal history and isotopic signature of its source magma (Harrison et al., 2014). Zircon typically incorporates up to 1-2 wt% Hf and is characterized by extremely low Lu/Hf (< 0.0005) (Finch & Hanchar, 2003; Kinny & Maas, 2003). The $^{176}Lu/^{177}Hf$ in zircon at the time of crystallization therefore is sufficiently low as to have a negligible and easily corrected contribution to the final $^{176}Hf/^{177}Hf$ of the crystal. The $^{176}Hf/^{177}Hf$ of the source melt from which the zircon crystallized is preserved, permitting reconstruction of crustal differentiation and magmatic assimilation processes when combined with zircon U-Pb age. Relating zircon isotopic composition to bulk-melt assimilation processes requires an understanding of the link between the thermal history of a pluton – which relates to its ability to crystallize zircon – and the degree of assimilation possible within the constraints of that thermal history. Prolonged recharge will suppress crystallization and lead to a broader range of isotopic compositions of the melt during the period that zircon is crystallizing, resulting in an isotopically heterogeneous population of zircon within a single pluton (Lovera et al., 2015). Plutons with a high zircon ε_{Hf} MSWD are not suitable for the Temperature-Flux model due to the complicating effects of extensive magma recharge on the relationship between ambient crustal temperature

and assimilation.

To calculate a "Hafnium Crustal Index" (HCI) requires estimates of both the mantle and crustal endmember components that contribute to the formation of granitic magma. The majority of Lhasa block zircon ε_{Hf} reported by Zhu et al. (2011) are consistent with a broadly Proterozoic crustal model age of the southern Lhasa terrane (i.e. average crustal $\varepsilon_{Hf} \approx -15$), with some grains inherited from Archean crust, assuming a source $^{176}Lu/^{177}Hf = 0.015$. Results of Hf and Nd isotopic compositions of pre-batholithic metasedimentary rocks presented here allow us to refine our estimate of crustal ε_{Hf} for the southern Tibetan basement rocks that predate the Mesozoic to Cenozoic granitoids (see discussion).

Interpreting magmatic mixing and assimilation histories from radiogenic isotopes can lead to mistaken assumptions about provenance, as a mixing relationship between juvenile mantle and ancient crust cannot be distinguished a priori from anatexis of old and fractionated mantle-derived material, such as lower-crustal cumulates. Oxygen isotopes are independent of crustal age, and whole-rock $\delta^{18}O$ of magmatic rocks is directly derived from the source material, whether that be the DM ($\delta^{18}O = +5.5‰$; Ito et al., 1987) or supracrustal material (from +15‰, for hydrothermally altered MORB, up to +42‰ for pelagic clays; Eiler, 2001), or some combination thereof. Oxygen isotopes in zircon record the magmatic signature at the time of crystallization – with an approximate -2‰ $\Delta^{18}O$(zircon-whole rock) – and have been shown to be resistant to resetting due to hydrothermal or deuteric alteration relative to other minerals (King et al., 1997; Valley, 2003; Bindeman, 2008; Trail et al., 2009). The diffusive lengthscale of ^{18}O in zircon is ~1 μm/Ma at 500ºC and ~275 μm/Ma at 900ºC under hydrothermal conditions (Watson and Cherniak, 1997), making zircon reasonably retentive of its most recent magmatic conditions, and more resistant to subsolidus alteration than other minerals. Petrographic and geochemical

evidence shows Gangdese batholith granitoids have all undergone some degree of hydrothermal or deuteric alteration (Blattner et al., 2002; Zhang et al., 2015). As long as care is taken to avoid zircons whose intra-sample oxygen isotope heterogeneity suggest secondary mixing with a hydrothermal or meteoric water source, zircon will provide the most robust mineral record of the primary magmatic oxygen isotope signature in these rocks. In this study we explore the multiple uses of zircon as a geochemical time capsule to explore the spatiotemporal crustal evolution of Southern Tibet throughout the India-Asia collision.

2.2 Methods

2.2.1 Whole-rock chemistry

Granitoid samples used in this study were collected during numerous field trips between 1994 and 2014. Sample locations are depicted in Figure 1, and numbers and GPS coordinates are reported in the supplementary material and in Alexander et al. (2019). Whole-rock major and trace element analyses were either performed at Pomona College on a 3.0 kW Panalytical Axios wavelength-dispersive XRF spectrometer or taken from Harrison et al. (2000). Pulverized samples were prepared with a 2:1 ratio of dilithium tetraborate and rock powder, which was then fused at 1000°C for 10 minutes, reground and fused again, and polished on diamond laps prior to analysis. Concentrations were determined using reference calibration curves using 55 certified reference materials. See Johnson et al. (1999) and Lackey et al. (2012) for detailed methodology and error assessment.

Finely pulverized whole-rock samples were analyzed for Hf isotopes at the PCIGR labs at the University of British Columbia. Aliquots of 100 mg of each sample was dissolved using high-pressure acid digestion in PTFE bombs. Hf was separated by column chemistry and analyzed by static MC-ICP-MS for masses 180, 179, 178, 177, 176 and 174 with monitoring of

^{176}Lu and ^{172}Yb; results are corrected for ^{176}Lu, ^{176}Yb, and ^{174}Yb interferences using natural abundances corrected for instrumental mass fractionation (see Weis et al., 2007 for details).

2.2.2 Zircon U-Pb, Ti $\delta^{18}O$, and ε_{Hf}

Zircon grains were separated from a crushed and sieved portion of each rock and mounted in epoxy, along with age and Hf standard material for internal reproducibility, and the surface of the grain mounts were polished flat. Mounts were coated with a ~100 Å layer of Au for SIMS measurements. Each grain was analyzed simultaneously for U-Pb age and Ti concentration on a CAMECA *ims*1270 at UCLA, using a 10-15 nA primary O^- beam. U-Pb age standard AS3 (1099±1 Ma; Paces & Miller, 1993) was used for the U-Pb age calibration, and NIST SRM-610 glass (Jochum et al., 2011) and AS3 (Aikman, 2007) were used to standardize Ti concentration. In separate sessions, the same zircons were analyzed on the CAMECA *ims*1270 at UCLA for ^{18}O /^{16}O using a 4 nA primary Cs^+ beam in multicollection mode, with a mass resolving power of over 4000. Grains were analyzed in 12 cycles with 10 seconds each of counting time, with 1 second of waiting time between cycles. Zircon standards AS3 ($\delta^{18}O$ = +5.34‰, Trail et al., 2007) and 91500 ($\delta^{18}O$ = +9.86‰; Wiedenbeck et al., 2004) were used, with 91500 used for tuning and AS3 grains on each mount for isotopic calibration (see Mojzsis et al., 2001 and Booth et al., 2005, for details).

In situ zircon Lu-Hf measurements were made with a 193-nm excimer laser coupled to a ThermoFinnigan Neptune MC-ICPMS at UCLA. Zircons were analyzed in their original epoxy mounts using apertures with nominal laser spot diameters of 52 and 69 μm, with zircon standards Mud Tank, Monastery, and Temora (Woodhead & Hergt, 2005) as well as AS3 (Harrison et al., 2008). The in-situ LA-ICPMS method has insufficient mass resolving power to separate isobaric interferences on Hf at masses 174 and 176. Yb, which is present in trace levels in zircon (Finch

& Hanchar, 2003), interferes on both 174 and 176; Lu, while generally in low abundance in zircon (Patchett et al., 1982), interferes on mass 176. The correction on masses 174 and 176 is achieved by measuring non-interfering Yb and Lu masses and calculating the contribution of the interfering masses to the 174 and 176 peaks using natural isotopic abundances. Contamination from cracks or inclusions is monitored with ^{181}Ta, though it was never detected above baseline in these measurements. Masses ^{171}Yb, ^{173}Yb, ^{174}Hf, ^{175}Lu, ^{176}Hf, ^{177}Hf, ^{178}Hf, ^{179}Hf, and ^{181}Ta were measured in 15 cycles per analysis, with a blank run for baseline correction between each block. For each sample, 6-10 grains were analyzed to account for individual grain heterogeneities due to inherited igneous cores or multi-stage growth histories. Data were corrected using the peak-stripping procedures detailed in Bell et al. (2011).

The zircon crystallization temperature (T_{zir}) was calculated using the Ti-in-zircon thermometer calibration of Ferry & Watson (2007). The concentration of Ti in zircon is given by:

$$\log\left(ppm\ Ti\right) = (5.711 \pm 0.072) - \frac{4800 \pm 86}{T(K)} - \log a_{SiO_2} + \log a_{TiO_2}$$

The inclusion of a_{TiO_2}permits expansion of the thermometer's utility to rutile-undersaturated systems; $a_{SiO_2} \approx 1$ was found to be appropriate not only for natural systems whose mineral assemblages imply silica saturation, but also for experimental run products with unbuffered a_{SiO_2}. The uncertainty in the linear fit to the experimental data results in an uncertainty in calculated T of ±12ºC (2σ); uncertainty in Ti concentration added ±11° to ±40° (1σ) to the temperature estimates. The activity of rutile in the system, a_{TiO_2}, is necessary for the temperature calculation but is difficult to precisely constrain in granitic systems. As the whole rock chemistry is not a good proxy for a_{TiO_2} in granitic rocks, we estimate a_{TiO_2}based on the assemblage of Ti-bearing minerals in the granites of interest. I use a_{TiO_2}= 0.6±0.15 due to the

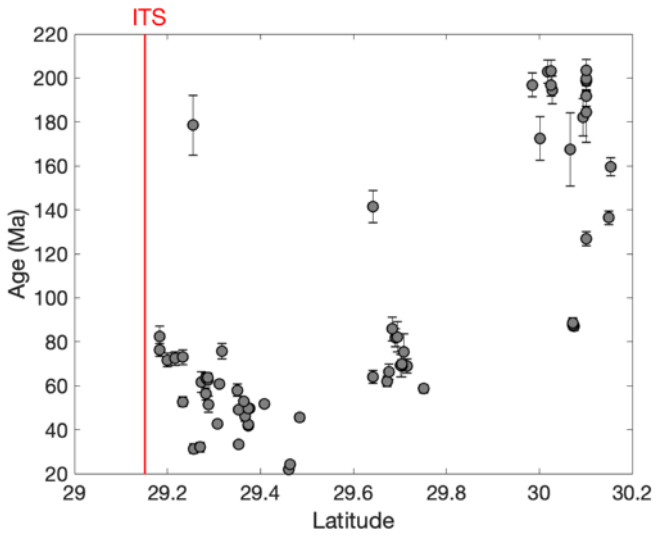

Figure 0.1 North-South distribution of sample ages; error bars are 2 s.e.; the red line is the modern latitude of the Indus-Tsangpo suture (ITS) at 92ºE.

absence of rutile (TiO_2), and presence of sphene ($CaTiSiO_5$) and ilmenite ($FeTiO_3$), in the majority of Gangdese Batholith granitoids, which implies 0.6< a_{TiO_2}<0.9 (Kapp et al., 2009)(Ghiorso & Gualda, 2013; Kapp et al., 2009). The potential error induced by underestimation of a_{TiO_2}averages 46ºC for maximum a_{TiO_2}= 1.0; 36ºC for maximum a_{TiO_2}= 0.9.

2.3 Results

Granitoid $^{206}Pb/^{238}U$ ages, locations, zircon Ti, T_{zir}, and major element data are reported in Table 1. Whole-rock ε_{Nd} and ε_{Hf}, zircon ε_{Hf} and $\delta^{18}O$, sample latitudes, and U-Pb ages (where available) are reported in Table 2.

2.3.1 U-Pb Ages of Southern Lhasa Block Granitoids

The zircon $^{206}Pb/^{238}U$ ages of granitoids in this study show a similar age distribution to previous work on Lhasa block granitoids (Fig. 2.1) (Quidelleur et al., 1997; Harrison et al., 2000; Zhu et al., 2009, 2011, 2015). Geochronological datasets such as these are generally incomplete, as sample collection cannot perfectly account for every unit and weight the number of analyses appropriately based on volumetric abundance of discrete plutons. Units found in or near roadcuts or otherwise accessible areas will tend to be overrepresented relative to more inaccessible

outcrops. Apparent gaps or spikes in magmatism must therefore be regarded skeptically, especially in an intrusive magmatic complex as expansive as the Gangdese batholith; we therefore abstain from interpreting the absolute quantity of ages for various age brackets as "spikes" in magmatism. While there is a general trend of youngest granites clustered nearest to the ITS, and oldest >75 km north of the suture, there are precollisional samples (up to 180 Ma) adjacent to the ITS (Fig. 2.1). Younger granodiorite units may exist in the subsurface further north; young (~10 Ma) two-mica granites have been reported ~100 km north of the ITS (DePaolo et al, 2019) but are not found in our dataset. Syncollisional (<50 Ma) granites are found exclusively within ~40 km of the ITS in our study, consistent with previously reported Tertiary granitoids found in abundance near the ITS and relatively sparse to the north (e.g. Harrison et al., 2000; Mo et al., 2005; Yin & Harrison, 2000; Zhu et al., 2015, 2011). We define "precollisional" rocks as those with zircon U-Pb ages >70 Ma, and "early syn-collisional" rocks as 50-70 Ma according to maximum and minimum estimates of the onset of collision between ~65 and ~50 Ma (Le Fort, 1996; Rowley, 1996; Yin & Harrison, 2000).

2.3.2 Hf Isotopes of Pre-Batholithic Metasedimentary Rocks

Figure 2.2 shows results for southern Lhasa block metasedimentary rocks and granitoids in the region between 89.5 and 92.5°E. The schist ε_{Nd} values fall between -9 and -12; this is consistent with the range used by DePaolo et al. (2019) for the crustal endmember in the Nd isotope Temperature-Flux model. Fig. 2.3 shows the relationship between zircon ε_{Hf}, granitoid whole-rock ε_{Nd}, and the pre-batholithic endmembers. In the region north of 29.8ºN, there are 2-mica granites with $\varepsilon_{Nd} \approx$ -12 to -14, so the crustal component north of 29.8º must have slightly lower ε_{Nd}. The same schist samples show a range of ε_{Hf} values from -3 to -23, with the discontinuity shifted south to ~29.6°N. Previously reported Mesozoic granites from ~ 30°N have

ε_{Hf} in the range -12 to -16, so it is likely that the ε_{Hf} value of the crust is closer $\varepsilon_{Hf} \leq -17$, consistent with our results for schists north of 29.6ºN. South of 29.6ºN, the data are consistent with crustal $\varepsilon_{Hf} \approx -10$. Previous compilations of granitoid zircon and whole-rock ε_{Hf} data from the southern Lhasa block, including those from Paleozoic granitic gneisses, suggest that the pre-Mesozoic crust south of 29.6ºN had ε_{Hf} values in the range of -5 to -10, consistent with these new data (Zhu et al., 2011; Chapman & Kapp, 2017). One of the metasediments analyzed is a metavolcanic sample with $\varepsilon_{Hf} \approx +13$, consistent with a mantle endmember $\varepsilon_{Hf} \approx +18$ used in our Hf isotope Temperature-Flux model (see discussion).

2.3.3 Zircon Hf Isotopes

There is good correlation between whole-rock ε_{Hf} and zircon ε_{Hf}, independent of unit age (Fig. 2.3a) such that we are confident that the zircon ε_{Hf} can be used as a proxy for the whole-rock signal. The relationship is quantified by least squares-maximum likelihood regression (after York et al., 2004), with slope $b = 0.97 \pm 0.21$ and intercept $a = 0.85 \pm 1.1$; error 1 σ. Cases where zircon ε_{Hf} is markedly more positive than the whole rock ε_{Hf} – indicative of isotopic disequilibrium between zircons and their host rocks – are associated with high whole-rock SiO_2 (>75%) (Fig. 2.3b), typically have T_{zir} below the hydrous granite solidus, and high MSWD in zircon O and/or Hf isotopes (Table S1). These factors may indicate that the zircon was always saturated at magmatic conditions, and the Hf isotopic composition of inherited or restitic zircon was preserved rather than crystallizing new zircon. The youngest plutons, <50 Ma, show substantially more variable zircon ε_{Hf}, compared to >50 Ma samples, and a strong correlation

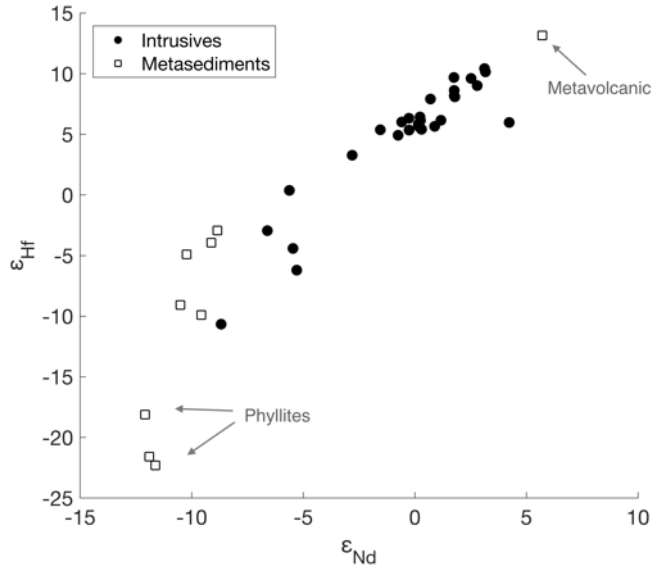

Figure 0.2: Whole-rock ε_{Nd} and ε_{Hf} of pre-batholithic metasedimentary rocks as well as granitoid intrusive and hypabyssal rocks. The metavolcanic sample, with ε_{Nd} = +5.7 and ε_{Hf} = +13.2, is consistent with a DM-like juvenile mantle endmember; crustal phyllites with ε_{Nd} = -8 to -12 and ε_{Hf} = -9 to -20 show a likely crustal endmember of $\varepsilon_{Nd} \approx$ -8 to -12 and $\varepsilon_{Hf} \approx$ -10 to -20; both increase with latitude.

between zircon ε_{Hf} and whole rock ε_{Hf}.

While in situ analysis for zircon Hf isotopes using LA-ICP-MS provides improved spatial resolution compared to solution methods, the relatively large laser spot size necessary for adequate sensitivity introduces uncertainty due to the likely averaging of multiple growth domains. In many zircon grains, especially those with inherited cores or long-lived, multi-stage magmatic growth histories, LA-ICP-MS analyses will average multiple discrete zones which may represent a wide range of crystallization conditions. This concern is partly addressed by analyzing multiple grains from each sample and interpreting the distribution of isotopic values and ages among the population. The isotopic composition of grains with substantial age inheritance (>20% difference) is not included in the computed weighted mean sample values, as the signal is not representative of final crystallization conditions. Excluding inheritance, inter-grain heterogeneity was typically within 2σ of analytical error for each sample; paired with good correlation between zircon ε_{Hf} and whole-rock ε_{Hf}, spatial averaging from laser ablation has a minimal effect on the results. Overall MSWD values for zircon ε_{Hf} have a median of 0.72, with a relatively broad distribution ($1\sigma_{MSWD}$ = 4.8); anomalously low MSWD for some populations

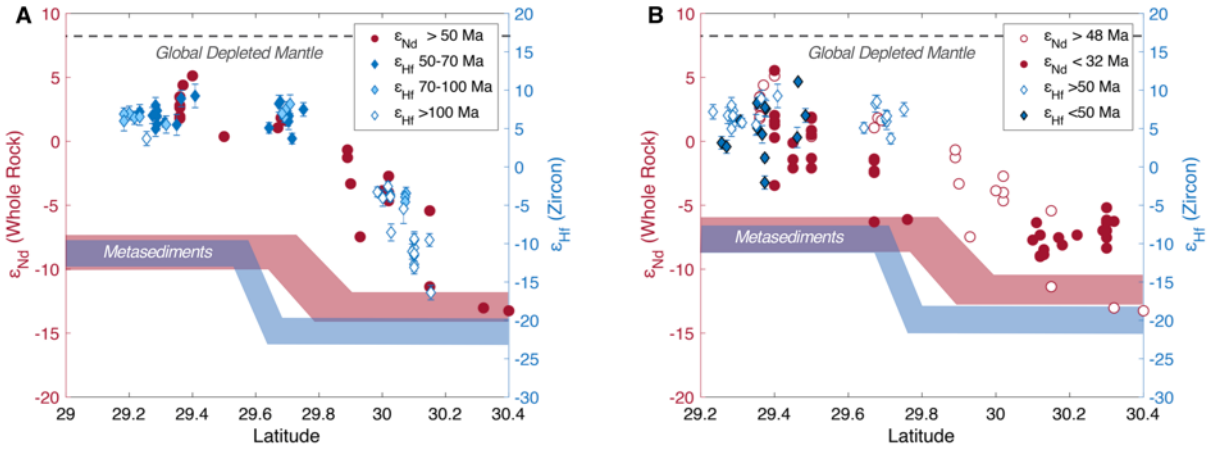

Figure 0.3: Zircon ε_{Hf} (blue, this study) and whole-rock ε_{Nd} (red, DePaolo et al., 2019) of pre- and early syn-collisional samples (A) as well as later syn-collisional samples (B) versus latitude. Red symbols correspond to left axis; blue to right axis. Shaded fields show likely crustal assimilant endmembers for Nd (red) and Hf (blue); Nd endmember becomes more positive for <32 Ma samples (DePaolo et al., 2019). Error bars on ε_{Hf} are 2 s.e.; dashed lines represent isotopic values for global average DM (ε_{Hf} = +18; ε_{Nd} = +8). Vertical axes are scaled to match both the global DM and crustal endmember values.

likely reflect the overestimation of analytical error from counting statistics. Cases with high MSWD with a small number of outliers in individual grain analyses could be spurious variation in ε_{Hf}, which can result from ablation of restitic inclusions or other inherited material which may not have been caught by our age inheritance filter. High MSWD relating to an overall broad inter-grain distribution of ε_{Hf} could reflect the effects of prolonged magma recharge during zircon crystallization (Lovera et al., 2015; see introduction).

2.3.4 Zircon Ti Thermometry

Zircon Ti analyses have analytical errors of <1 to 4 ppm. Calculated T_{zir} for Lhasa block

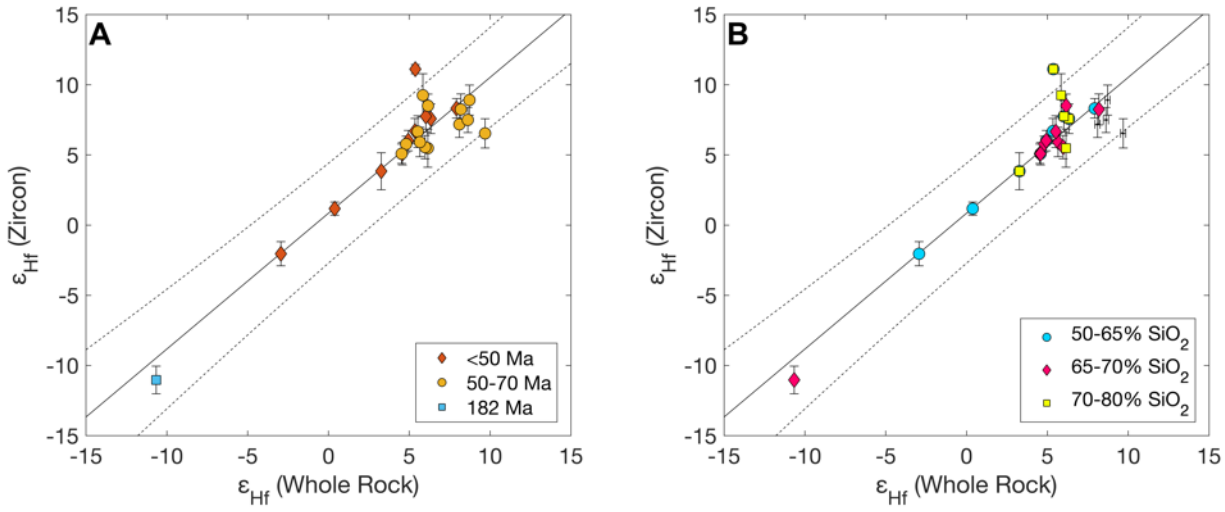

Figure 0.4: Whole-rock and zircon ε_{Hf} values according to age (a) and whole-rock weight percent SiO_2 (b). Error bars for zircon ε_{Hf} is 2 s.e.; error bars for whole-rock ε_{Hf} are narrower than the data markers. Black solid line is the least squares-maximum likelihood fit (after York et al., 2004) described by $\varepsilon_{Hf(z)} = (0.968\pm0.207)\varepsilon_{Hf(wr)} + (0.850\pm1.05)$, MSWD = 2.86; black dashed lines are the 95% confidence bounds of the linear fit.

granitoids ranges between 620±28ºC and 924±35ºC; maximum and minimum values occur at 65.9 and 60.9 Ma, respectively (Fig. 2.5). As many as 22% of all samples have T_{zir} below the hydrous granite solidus (ca. 620°C), which is either due to overestimation of $\boldsymbol{a_{TiO_2}}$, which leads to underestimation of temperature, or due to sub-solidus zircon crystallization, likely in a fluid-

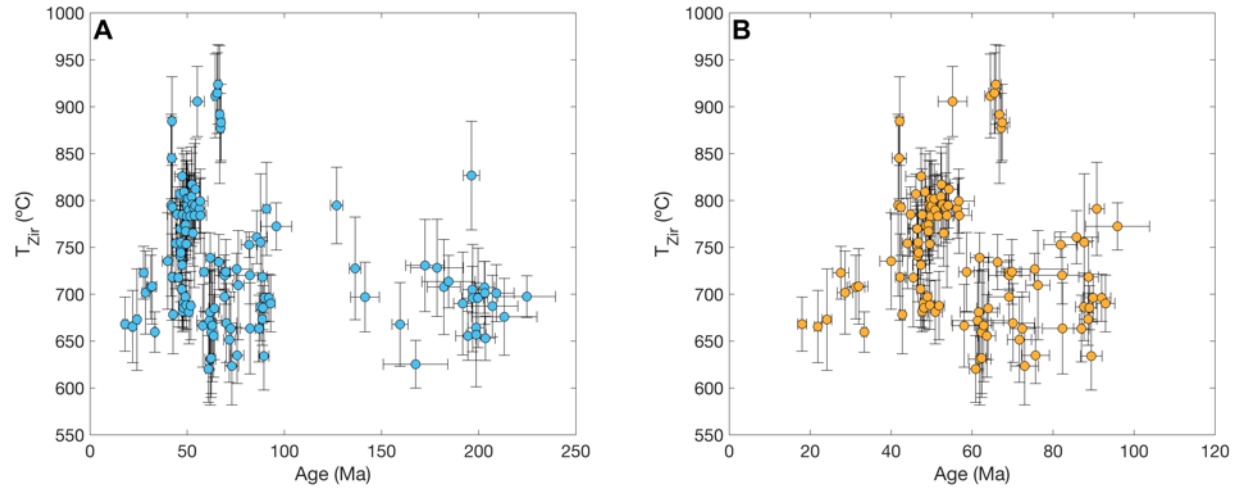

Figure 0.5: Ti-in-zircon temperatures and ages of all samples (A) and samples up to 100 Ma (B), calculated using the calibration of Ferry and Watson (2007). Age error bars are 2 s.e.; T_{zir} error bars include the 1σ analytical uncertainty in Ti concentration as well as the uncertainty of the thermometer calibration at the 95% confidence level. For all samples, $\boldsymbol{a_{TiO_2} = 0.6}$ and $\boldsymbol{a_{SiO_2} = 1}$ was used.

rich, undercooled stage of pluton solidification. Total error in T_{zir} induced by the uncertainties in calibration, analytical Ti measurements, and estimation of $\boldsymbol{a_{TiO_2}}$, can lead to 4-5% uncertainty in temperature. The total range of calculated temperatures far exceeds variation induced by uncertainty, so broad trends in the distribution of T_{zir} can still be resolved.

2.3.5 Zircon Oxygen Isotopes

Oxygen isotope results are reported using standard delta notation relative to Vienna Standard Mean Ocean Water (VSMOW); error is reported at one standard deviation. The average δ18O value for all samples irrespective of age was 5.77±0.80‰ (1σ of total distribution), with average analytical error of 0.34‰. Syncollisional samples (U-Pb age ≤ 70 Ma) have mean δ18O = 5.59±0.77‰ (1σ). Median MSWD of oxygen values is 2.6, with some anomalously high values derived from greater intra-sample heterogeneity. There is no obvious correlation between age and δ18O; there is greater heterogeneity in >100 Ma samples, possibly due to inheritance, increased geographic distribution, or higher occurrence of secondary alteration. There is

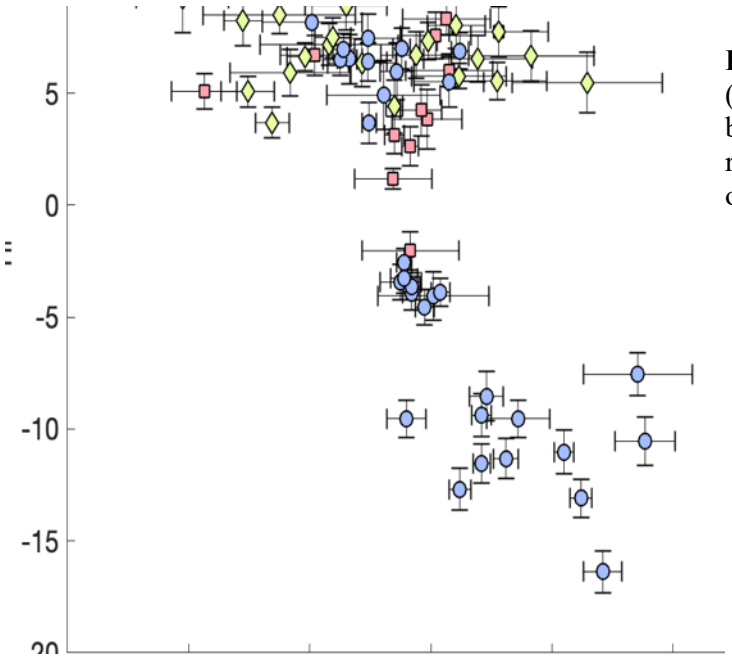

Figure 0.6: Zircon ε_{Hf} and $\delta^{18}O_{VSMOW}$ (Vienna Standard Mean Ocean Water); error bars are 2 s.e. The >70 Ma group ranges relatively continuously in age up to the oldest at 203.5±5 Ma.

additionally minimal correlation with zircon εHf (Fig. 2.6) and no correlation with T_{zir}.

2.4 Discussion

2.4.1 Assimilation Evidence

While magmatic inflation may account for ~15 km of Tibetan crustal thickening throughout collision (Mo et al., 2007; Chen et al., 2018; DePaolo et al., 2019), magmatic heat added to the crust is insignificant compared to total orogenic heat flow, and therefore cannot explain increased assimilation (De Yoreo et al., 1989). Magma recharge, as opposed to increased crustal thickness (i.e. higher wall-rock temperature), could promote heterogeneity of zircon ε_{Hf} based on results of RAFC modeling of ε_{Hf} in zircon (Lovera et al., 2015). Prolonged recharge increases the crystallization window of zircon, allowing zircon to record the prolonged assimilation process induced by recharge. The current analytical restrictions that generally limit zircon ε_{Hf} measurements to a single datum per grain precludes resolving depth-dependent Hf isotopic variations that could reveal complex thermoisotopic histories in individual zircons. However, inter-grain heterogeneity of ε_{Hf} in magmatic zircons within each sample can provide a sense of overall zircon ε_{Hf} heterogeneity. The inter-grain zircon ε_{Hf} variability for individual samples of Lhasa-block syncollisional plutons reported here are within analytical error, so inter-sample heterogeneity among <50 Ma plutons cannot be explained by an increase in magma recharge alone. Increased assimilation from higher wall-rock temperature at the base of a thicker crust is most consistent with a greater crustal component in the zircon ε_{Hf} of syncollisional granitoids. The similar spatial trends of whole-rock ε_{Nd} and zircon ε_{Hf} (Fig. 2.3) suggest that where assimilation occurred, thermal and chemical conditions were such that there was moderate to low discrimination between Nd and Hf isotopic assimilation mechanisms, even in cases where

both zircon and whole rock retained a relatively mantle-like signature in both systems.

Hf crustal model age estimates for the Lhasa block range between 1.5-3.0 Ga based on central- to northern-Lhasa inherited zircon ages and Hf isotopes (Zhu et al., 2011). Mantle-like $\delta^{18}O$ values for all but a few early-Jurassic samples indicate the crustal assimilant is likely ≥1.5 Ga mantle-derived rock, rather than isotopically evolved supracrustal material, which additionally supports our interpretation that granite hybridization proceeds mostly at the base of the crust. $\delta^{18}O$ values for all samples are within ±2‰ of the average mantle value $\delta^{18}O$ = +5.5‰ (Ito et al., 1987), which is substantially less enriched than the minimum $\delta^{18}O$ values expected for metasedimentary material. As zircon $\delta^{18}O$ is unlikely to be increased by secondary processes (King et al., 1997), values that are more negative than average mantle are consistent with lower-crustal gabbros, which range from +3.5‰ to +5.5‰, or interactions with meteoric water (Gregory & Taylor, 1981; Eiler, 2001). Moreover, samples with $\delta^{18}O$ lower than average mantle do not show signs of heterogeneity that would be expected from partial resetting (average MSWD of this subset is no greater than the data in aggregate). Granitoid samples (>55% SiO_2) range in aluminosity, with molar $Al_2O_3/(CaO+Na_2O+K_2O)$ from 0.74 to 1.19 (Fig. 2.7). Major element trends are broadly consistent with fractional crystallization (Fig. 2.7); assimilation would have had to occur with a protolith whose major element ratios were not substantially different from the juvenile melt.

The origin of mafic melts that contribute to granitic magmatism impacts the isotopic and chemical signature of the resultant granitoids; the most plausible source of a basaltic endmember melt must be evaluated in the context of the isotopic and geochemical data presented here. Partial melting and assimilation of eclogite with a hydrous basalt in arc settings has been shown to produce granitic melt in equilibrium with the eclogite residue (Rapp et al., 2003; Bouihol et al.,

2015). Continual production of slab-derived melts with an eclogitic restite is a tempting explanation for the production of these melts and would not require substantial juvenile DM component in the melts to produce relatively radiogenic Hf isotopes. However, partial melts of slab materials would have more positive $\delta^{18}O$ due to the incorporation of altered basaltic crust; only 100% slab melt could produce a mantle-like $\delta^{18}O$ with no juvenile component, and there would be no eclogitic restite (Eiler, 2001). Thermodynamic modeling of subduction zone melting further suggests that slab dehydration occurs at much shallower pressures than slab melting, and the fluids released during dehydration can produce substantial melting of a thick, hydrated mantle wedge (Bouihol et al., 2015). This melt then readily travels to the base of the overriding plate and fractionates, potentially without removal of garnet or amphibole, leading to an "adakitic" signature in some fractionated products. Depending on the depth of fractionation, if garnet and amphibole are removed, the same primary melting process (melting of a hydrated mantle wedge) may produce both adakitic and calc-alkaline felsic products. This process may provide an explanation for the appearance of a range of adakitic signature in syncollisional

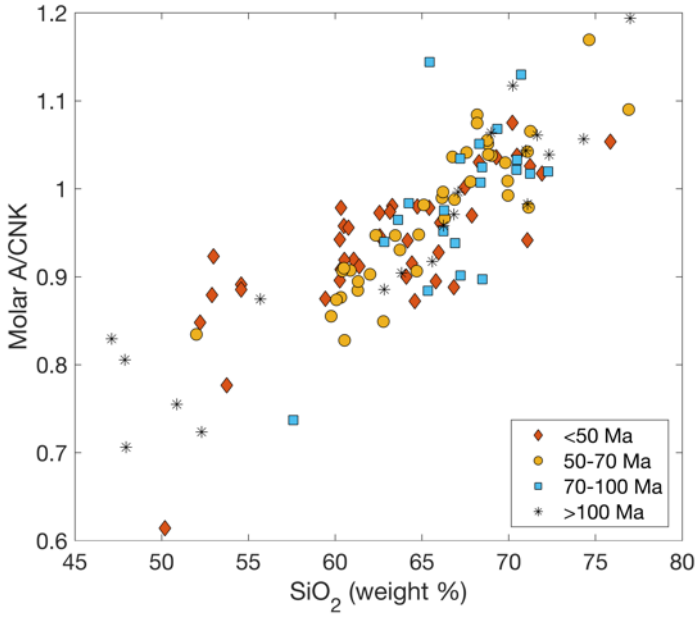

Figure 0.7: A/CNK = Molar $Al_2O_3/(CaO + Na_2O + K_2O)$ for granitoid samples (>60% SiO_2) and mafic enclaves (<60% SiO_2), representing typical fractional crystallization from a metaluminous mafic source; this pattern is unchanged from precollisional samples to later-syncollisional samples (< 50 Ma).

magmas, which have previously been attributed to geodynamically disfavored processes such as "slab breakoff" (e.g. Chung et al., 2005; Chen et al., 2014; Zhu et al., 2017; cf. Garzanti et al., 2018), or have been used to imply cessation of calc-alkaline Gangdese arc magmatism by 45 Ma (e.g. Ji et al, 2016) – which is clearly not the case based on the persistence of calc-alkaline melts well after 45 Ma, as presented here (Figs. 2.1, 2.7).

Fractional crystallization of a pure mantle melt is more favored by the major element relationships seen in <70 Ma granites across the Lhasa block (Fig. 2.7). If these granites were derived from a pure DM source, however, they would be expected to have exclusively mantle-signature $\varepsilon_{Hf} \approx +18$ and $\delta^{18}O \approx +5.5$ (Ito et al., 1987; Vervoort & Blichert-Toft, 1999), as isotopic ratios cannot be altered by closed-system magmatic fractionation. What we observe in early- and later-syncollisional granites is an ε_{Hf} signature that is moderately depressed relative to DM, and an average $\delta^{18}O$ that is slightly elevated relative to average DM value (Fig. 2.6). Nd isotopes additionally demonstrate an isotopic mixing trend that favors large fractions of mantle melt mixed with some assimilated crustal material (DePaolo et al., 2019). Intermediate values of ε_{Hf} are interpreted as the result of assimilation between juvenile mantle-derived melt (DM, $\varepsilon_{Hf} \approx +18$) and less radiogenic basement rocks of the Lhasa block (ε_{Hf} -5 to -20). The bulk of assimilation is assumed to occur at or near the Moho, where the temperature contrast between juvenile magma and surrounding lower-crustal rocks is small, favoring higher assimilation. While additional assimilation may occur following fractionation and emplacement of granitic melts, the necessarily lower magmatic temperature and greater polymerization of a silicic melt would lower the diffusivity of rare earths in the melt (Mungall et al., 1999); and low-T wallrock would minimize the ability of the melt to extract substantial crustal material. The fractionation of melt sourced from DM, and possibly assimilated with eclogitic residue, additionally requires that

hybridization and fractionation occur at the base of the crust.

2.4.2 Isotopic Constraints on Crustal Thickness

The granitoids along the 92º E traverse provide a window into the plutonic evolution of the southern Lhasa block: this area provides a near-continuous plutonic history from <20 Ma to ca. 225 Ma (Fig. 2.1), as greater exhumation of the eastern Lhasa block has exposed younger (syncollisional) plutons (Harrison et al., 1992; Zhu et al., 2015). For any given age range of Gangdese granitoids within the Lhasa block, east-west variation in geochemistry and age distributions is less significant relative to the substantial variation associated with northward distance from the southern margin of Eurasia, at the Indus-Tsangpo Suture (ITS) (Harrison et al., 2000; Yin & Harrison, 2000; Kapp et al., 2005; Chung et al., 2009; Zhu et al, 2011; Chen et al., 2014). We therefore consider north-south distance from the ITS to be the main variable in spatial isotopic trends.

We interpret our results through the lens of the thermoisotopic framework developed by DePaolo et al. (1992) and quantified with respect to the Tibetan granites by DePaolo et al. (2019), using the NCI "Temperature-Flux" model. DePaolo et al. (2019) proposed that the whole-rock Nd isotopic signatures of a suite of Lhasa-area granitic plutons could be used as a quantitative proxy for crustal thickness based on the degree of isotopic assimilation between juvenile mantle and old crust. They use the parameterized Temperature-Flux model to approximate crustal thickness of Gangdese granitoids emplaced before and after the onset of continental collision. They identify a systematic decrease in whole-rock ε_{Nd} from south to north, from ε_{Nd} = +5 adjacent to the ITS to ε_{Nd} = -13, 110 km to the north. For the purpose of their model, DePaolo et al. (2019) use 48 Ma as a lower limit age for precollisional granites based on the compilations of Zhu et al. (2017). In ≥48 Ma Lhasa block granites, their model suggests a 25-

35 km-thick crust adjacent to the ITS which thickens rapidly to >45 km-thick approximately 100 km north of the ITS. The ε_{Nd} of "postcollisional" granites (<32 Ma as defined by DePaolo et al., 2019) show evidence of a much thicker crust within ~50 km of the ITS; the crust was up to 75 km-thick adjacent to the suture by the latest Paleogene. The results of DePaolo et al. (2019) can be compared to patterns in zircon ε_{Hf}, age, and distance to the ITS, given similar behavior between Nd and Hf isotopic systems in crustal processes.

The isotopic data from this study are largely from locations farther east than those of DePaolo et al (2019). Nevertheless, the equivalent north-south trend in both whole-rock and zircon ε_{Hf} reported here suggest the early syncollisional (48 Ma) structure inferred from the Nd data by DePaolo et al. (2019) extends to the east at least to 92.5°E, and that the two isotopic systems have preserved evidence of the same tectono-magmatic history of the region (Fig. 2.3). Given the strong correlation between whole-rock and zircon ε_{Hf} (Fig. 2.4), the latter may be used in conjunction with U-Pb ages to track the spatiotemporal evolution of the S. Tibetan crust. Though it is likely that initial collision began earlier than 50 Ma and gradually propagated to encompass the entire northern margin of India over the course of many Ma, reconstructed isotopic assimilation signatures as calculated by DePaolo et al. (2019) suggest that substantial changes in petrogenesis of Gangdese granites do not appear until <50 Ma; younger granites are treated here as "later-syncollisional" as a reflection of ongoing full continental collision from ~50 Ma to the present. The Hf isotopic data presented here represent samples aged 225±15 Ma to 22±1 Ma; only four units in our study fall within the <32 Ma criteria used by DePaolo et al. (2019) to infer later syncollisional thickening.

Using zircon Hf values as a basis, we applied the Temperature-Flux model to calculate NCI; herein we refer to it as "HCI": Hafnium Crustal Index (Fig. 2.8). $\varepsilon_{Hf(r)} = +18$ was used for

the juvenile mantle value (Vervoort & Blichert-Toft, 1999). For the case of a latitudinally homogeneous crustal assimilant, we use $\varepsilon_{Hf(a)}$ = -15 as the endmember, consistent with a typically Proterozoic Tibetan basement (Zhu et al., 2011) (Fig. 2.8a-b). HCI ranges from ~0.2 to 1, implying relatively high degrees of assimilation for all samples. Based on inherited zircon ε_{Hf} values presented in Zhu et al. (2011) and our pre-batholithic schist analyses, however, it is more likely that the crustal assimilant values are dependent on latitude. Recalculating HCI based on

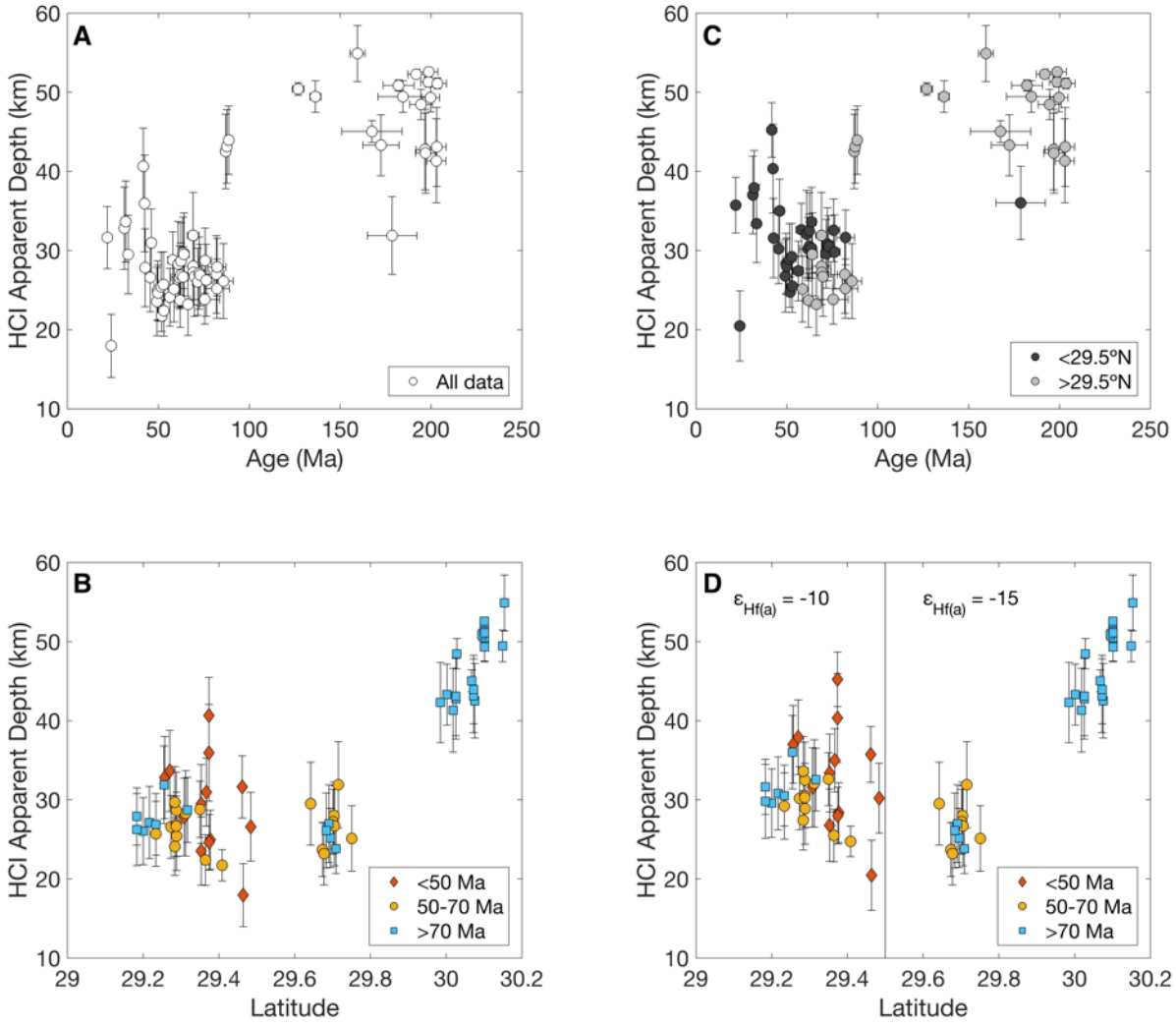

Figure 0.8: Zircon Hafnium Crustal Index ("HCI") apparent Moho depths with age (a) and latitude, sorted by age (b). Depths calculated from zircon HCI, assuming DM εHf = +18 and crustal εHf = -15. Depth calculation using Temperature-Flux model of DePaolo et al. (2019) using similar parameters, such that depth H = 2.4 + 80.6(HCI) – 29(HCI)2. Error bars on HCI derive from 2 s.e. of zircon Hf measurements. Age error bars are 2 s.e.

$\varepsilon_{Hf(a)}$ = -10 for samples south of 29.6ºN and $\varepsilon_{Hf(a)}$ = -15 north of 29.6º leads to commensurately higher HCI for the southern samples. Using the Temperature-Flux model of DePaolo et al. (2019) with identical parameters, apparent crustal thicknesses range from ~18 km to ~55 km when $\varepsilon_{Hf(a)}$ = -15 for all samples. When samples south of 29.6º have $\varepsilon_{Hf(a)}$ = -10, the range is ~20 km to 55 km. Using the model geotherm of DePaolo et al. (2019), HCI apparent depth increases within a narrow range of variations in sample ε_{Hf} until their values approach the composition of the crustal assimilant. An extremely steep model geotherm of 50ºC/km forces a steeper association with HCI and depth, though such a steep geotherm would be unrealistically high for a typical arc setting, especially for depths greater than ~15 km (Rothstein & Manning, 2003). The assumption of $\varepsilon_{Hf(r)}$ = +18 may be an overestimate, as the lithospheric mantle below the Tibetan crust may not be as depleted as global MORB or may have interacted with unradiogenic contaminant prior to melting and forming the magmas of interest, though the metavolcanic sample with ε_{Hf} = +13 suggests the lithospheric mantle under southern Lhasa was near to modern DM Hf composition. A more negative $\varepsilon_{Hf(r)}$ would lead to apparently thinner crust using the HCI Temperature-Flux model.

Calculated apparent depths can be associated with sample age (Fig. 2.8a) and latitude (Fig. 2.8b). When compared to age alone, HCI Moho depths imply a thinning crust between ~100 and 50 Ma, and a thickening crust following 50 Ma, though the spatial variations with latitude are obscured with this simple comparison. There is a clear discontinuity at ~29.8ºN in precollisional samples in whole-rock ε_{Nd} and zircon ε_{Hf} (Fig. 2.3a) which implies preexisting crustal structure that must be considered when evaluating relative thicknesses through time. Fig. 2.8 shows little change from precollisional (> 70 Ma) to the early syncollisional period (50 – 70 Ma), and markedly increased apparent depths in later syncollisional samples near the ITS. The

HCI results emulate the thickening inferred by DePaolo et al. (2019) from their ε_{Nd} – based Temperature-Flux model depths. Above an HCI of 1, corresponding to a Moho depth of ~55 km, our parameterization of the Temperature-Flux model saturates. That is, an HCI ≥ 1 implies 100% assimilation of the crustal component, and can therefore not be distinguished from isotopic assimilation occurring at greater depths. Cases where the apparent depth is ≥55 km represent this upper bound. For all syncollisional samples, however, the calculated HCI <1 implies these units formed within the limits of the model. The large range of HCI apparent Moho depths, especially among <50 Ma samples, could imply increased heterogeneity of the juvenile melt or the assimilant material, greater variation in the duration and volume of magma recharge during pluton construction, or may even betray inconsistencies in the assumed model parameters. It is possible the hybridization, assimilation, and crystallization environment of each individual sample was sufficiently different that applying the same model parameters to multiple samples obfuscates accurate calculation of HCI. Inferences may be drawn from systematic differences through time, regardless of depth accuracy, but the HCI model does not prove a priori whether the southern Tibetan crust was thick or thin prior to collision.

2.4.3 Structural Implications

The persistent gradient of positive, mantle-like zircon ε_{Hf} near the ITS, decreasing to more negative, evolved crustal signature to the north implies a strong controlling process on Hf isotopes in the Southern Lhasa Block for the past 200 Ma. Lack of deviation from strong mantle signature within ~ 80 km of the ITS in precollisional (> 50 Ma) and early syncollisional (40–50 Ma) plutons is additionally consistent with minimal assimilation of crustal material by a juvenile mantle melt source. Following the model of melt production occurring at the base of the crust, and degree of assimilation proportional to wall-rock temperature, minimal assimilation in all

mid-Cretaceous to early Tertiary granites within ~80 km of the ITS implies granitic melt hybridization at the base of a thin crust, where country rock T was too low for substantial assimilation with juvenile melt. Increased heterogeneity in zircon ε_{Hf} of <50 Ma samples, all of which are found within 40 km of the ITS, supports this evidence of increased assimilation with crustal material, which in turn is consistent with higher-temperature storage and fractionation of these evolving melts. Accretion of subducted Indian upper-crustal material onto the base of the Eurasian crust at the ITS following the onset of continental collision would provide a new source of less radiogenic Hf at the base of the Eurasian crust; it would additionally contribute to the ongoing thickening process. A thickened Eurasian lower crust broadens the range of depths at which hybridized granitic melts would likely be emplaced, promoting additional heterogeneity in the degree of crustal assimilation for each discrete pluton (DePaolo, 1981; Pearce, 1996; Kemp et al., 2007).

The robust spatial trends in ε_{Nd} and ε_{Hf} as a function of N-S distance from the ITS must represent long-lived processes controlling the production and chemistry of the Gangdese batholith in the Lhasa block. There are three scenarios that could produce large volumes of granitic melt in Southern Tibet over many tens of Ma throughout the India-Asia collision: 1) Pure crustal anatexis of the (older) mid-crust in the Lhasa block; 2) fractional crystallization of partial-melt of the mantle wedge; or 3) hybridization of juvenile mantle melt with crustal material at the Moho. Pure crustal anatexis is incapable of explaining the relatively homogeneous, mantle-like signature of both ε_{Hf} and $\delta^{18}O$ just prior to and during the early stages of collision. Jurassic granites in the central and northern Lhasa blocks have negative ε_{Hf} consistent with formation from melting of Proterozoic basement rocks with $^{176}Lu/^{177}Hf = 0.015$ (Zhu et al., 2011), with $\varepsilon_{Hf} \sim -15$; pre- and syncollisional melts forming from the same crustal

root would be expected to have similarly negative ε_{Hf}.

Long-term maintenance of this regime of minimal assimilation at the ITS throughout the Jurassic and Cretaceous precludes major changes in the structure and crustal thickness of the southern Lhasa block throughout this time period. Despite the substantial magmatic inflation associated with the near-continuous emplacement of the Gangdese batholith during this period, there is no indication of significant precollisional crustal thickening, which would have resulted in greater degrees of crustal assimilation and anatexis in progressively younger rocks. The possibility that, in a thickened crust, younger Gangdese granites assimilated only with older mantle-derived Gangdese plutons (i.e., no crustal material), is precluded, as the Lhasa block bedrock includes substantial Cretaceous sedimentary strata (Kidd et al., 1988; Leier et al., 2007). An external process must therefore have controlled the geometry of the southern margin of the Lhasa block.

Prior to collision, the southern margin of the Lhasa block was a long-lived continental arc accommodating the closure of the neo-Tethys ocean basin (Allégre et al., 1984; Yin & Harrison, 2000). The crustal thickness at the arc margin, now the modern ITS, was a function of thickening due to magmatic inflation and tectonic accretion and thinning due to erosion or exhumation (Lee et al., 2015). As the formation of the Gangdese batholith contributed to magmatic inflation of the Lhasa block, there must also have been continuous removal of crustal material at the ITS in order to maintain the wedge-shaped N-S geometry of the crust in southern Lhasa. Structural and paleoelevation studies of the Lhasa block (England & Searle, 1986; Murphy et al., 1997; Ingalls et al., 2016) suggest that the southern Tibetan plateau was at high elevation prior to continental collision (although England & Searle (1986) argued for precollisonal thickening occurring only in the Gangdese Batholith whereas our data suggest that the southernmost margin remained

relatively thin until continental collision began).

The high convergence rate at the ITS prior to India-Asia continental collision (Rowley, 1996) and the evidence of steep subduction angle from ultra-high-pressure metamorphic rocks (Leech et al., 2005) suggest that moderate levels of subduction erosion may have controlled the thickness of the southern Tibetan crust without substantial input of slab material into the overriding plate. The rapid decrease in convergence rate, increase of subducted continental material, and flattening of the underriding slab following the onset of collision all would have contributed to increased addition of crustal material to syncollisional magmas, as observed in Hf, O, and Nd isotope systematics of syncollisional granitoids.

The HICLIMB study (Nableck et al., 2009) imaged the Tibetan crust and upper mantle along a N-S transect about 150 km west of Lhasa. This 2D profile was interpreted as showing ~80 km thick crust across the block at this location, including ~35 km of Indian crust, although there are significant crustal thickness variations along strike (Zurek et al., 2007). Nableck et al. (2009) interpreted anisotropy at the crust/mantle interface to reflect sustained shearing during formation. If this section is representative of the crustal structure beneath our transect then the lack of significant post-collisional upper crustal deformation in the southern Lhasa Block, as documented by the widespread unconformity between the Paleocene Linzizong Volcanics and Late Cretaceous Takena Formation (Dewey et al., 1988), and ~10 km of denudation adjacent the suture zone (e.g., Copeland et al., 1987) requires that ca. 50 km of crustal thickening has occurred since ~50 Ma (including the ~10 km lost via denudation) via accretion from below – most likely the result of underplating of Indian crust.

Four isotopic systems therefore are broadly consistent with the view that juvenile melts were hybridized and fractionated in the lower crust, with small degrees of crustal assimilation

between ~90 to 50 Ma. Post-50 Ma samples at the ITS show greater degree of crustal assimilation, suggesting rapid thickening of the crust adjacent to the ITS since the onset of collision, which is consistent with interpretations of modern seismic data. In general agreement with results of recent geochemical models (Zhu et al, 2017; DePaolo et al., 2019), we infer that the southern margin of Tibet was relatively thin for at least 150 Ma prior to the onset of collision at ~50 Ma, and underwent rapid crustal thickening for at least the next 25 Ma.

2.5 Conclusions

A suite of Gangdese granites from a north-south transect around ~92ºE in the Lhasa block of southern Tibet show significant north-south variation in Hf isotopes with distance from the southern margin of the Lhasa block, at the Indus-Tsangpo Suture (ITS). There is a strong correlation between zircon and whole-rock ε_{Hf} in units spanning >200 Ma to <40 Ma, permitting the use of zircon as a proxy for whole-rock ε_{Hf} in pre- and syncollisional plutons. Northward distance from the ITS is negatively correlated with zircon ε_{Hf}, with less radiogenic values in older, northward granites, while the bulk of <100 Ma granites within ~75 km of the ITS show more radiogenic, near mantle-like values. Whole-rock major element geochemistry, zircon ε_{Hf} and $\delta^{18}O$ of 50–180 Ma granites are consistent with continuous juvenile magma input to the lower crust of the southern margin of Tibet for the past ~200 Ma. Lack of heterogeneity in ITS-adjacent precollisional samples is consistent with low degrees of crustal assimilation during fractionation and emplacement of granitic magmas in the southern Lhasa block throughout the Jurassic and Cretaceous periods. Syncollisional (<50 Ma) samples show increasing geochemical evidence of assimilation with crustal material, both in greater heterogeneity of zircon ε_{Hf} as well as whole-rock major and trace element evidence (this study; Chen et al., 2018). Minimal precollisional crustal assimilation, and increased syncollisional assimilation in granites formed

near the ITS is consistent with thermoisotopic modeling of whole-rock ε_{Nd} that indicates progressive thickening of the crust immediately adjacent to the ITS between ~50 and 32 Ma. Zircon U-Pb, Hf, and O isotopes, as well as whole-rock Hf isotopes and bulk geochemistry, indicate that the southern margin of the Lhasa block was thin for up to 150 Ma prior to collision, and thickened rapidly following the onset of hard collision at ~50 Ma. The persistence of calc-alkaline, mantle-like granitic melts throughout the lifetime of the precollisional continental arc is consistent with a wedge-shaped crustal geometry of the southern margin of the Lhasa block for 150 Ma prior to collision.

2.6 References

Aikman, A. (2007). Tectonics of thse eastern Tethyan Himalaya, (Doctoral Dissertation). Retrieved from Open Research. (https://openresearch-repository.anu.edu.au/handle/1885/146541) Canberra, Australia: Australian National University.

Allégre, C. J., Courtillot, V., Tapponnier, P., Hirn, A., Mattauer, M., Coulon, C., et al. (1984). Structure and evolution of the Himalaya–Tibet orogenic belt. Nature, 307(5946), 17–22. https://doi.org/10.1038/307017a0

Bell, E. A., Harrison, T. M., McCulloch, M. T., & Young, E. D. (2011). Early Archean crustal evolution of the Jack Hills Zircon source terrane inferred from Lu–Hf, $^{207}Pb/^{206}Pb$, and $\delta^{18}O$ systematics of Jack Hills zircons. Geochimica et Cosmochimica Acta, 75(17), 4816–4829. https://doi.org/10.1016/j.gca.2011.06.007

Bindeman, I. (2008). Oxygen Isotopes in Mantle and Crustal Magmas as Revealed by Single Crystal Analysis. Reviews in Mineralogy and Geochemistry, 69(1), 445–478.

https://doi.org/10.2138/rmg.2008.69.12

Blattner, P., Abart, R., Adams, C. J., Faure, K., & Hui, L. (2002). Oxygen isotope trends and anomalies in granitoids of the Tibetan plateau. Journal of Asian Earth Sciences, 21(3), 241–250. https://doi.org/10.1016/S1367-9120(02)00046-9

Booth, A. L., Kolodny, Y., Chamberlain, C. P., McWilliams, M., Schmitt, A. K., & Wooden, J. (2005). Oxygen isotopic composition and U-Pb discordance in zircon. Geochimica et Cosmochimica Acta, 69(20), 4895–4905. https://doi.org/10.1016/j.gca.2005.05.013

Bouilhol, P., Magni, V., van Hunen, J., & Kaislaniemi, L. (2015). A numerical approach to melting in warm subduction zones. Earth and Planetary Science Letters, 411, 37–44. https://doi.org/10.1016/j.epsl.2014.11.043

Chapman J. B., & Kapp, P. (2017). Tibetan Magmatism Database. Geochemistry, Geophysics, Geosystems, 18(11), 4229–4234. https://doi.org/10.1002/2017GC007217

Chapman, J.B., Ducea, M.N., Kapp, P., Gehrels, G.E. and DeCelles, P.G., 2017. Spatial and temporal radiogenic isotopic trends of magmatism in Cordilleran orogens. Gondwana Research, 48, 189-204. https://doi.org/10.1016/j.gr.2017.04.019

Chen, J.L., Yin, A., Xu, J.F., Dong, Y.H., & Kang, Z.Q. (2018). Late Cenozoic magmatic inflation, crustal thickening, and >2 km of surface uplift in central Tibet. Geology, 46(1), 19–22. https://doi.org/10.1130/G39699.1

Chen, Y., Zhu, D.C., Zhao, Z.D., Meng, F.Y., Wang, Q., Santosh, M., et al. (2014). Slab breakoff triggered ca. 113Ma magmatism around Xainza area of the Lhasa Terrane, Tibet. Gondwana Research, 26(2), 449–463. https://doi.org/10.1016/j.gr.2013.06.005

Chiaradia, M., (2015). Crustal thickness control on Sr/Y signatures of recent arc magmas: an

Earth scale perspective. Scientific reports, 5, 8115.

Chung, S.L., Chu, M.F., Ji, J., O'Reilly, S. Y., Pearson, N. J., Liu, D. et al. (2009). The nature and timing of crustal thickening in Southern Tibet: Geochemical and zircon Hf isotopic constraints from postcollisional adakites. Tectonophysics, 477(1), 36–48. https://doi.org/10.1016/j.tecto.2009.08.008

Copeland, P., Harrison, T.M., Kidd, W. S. F., Xu, R., & Zhan, Y . (1987). Rapid early Miocene acceleration of uplift in the Gangdese Belt, Xizang (southern Tibet), and its bearing on accommodation mechanisms of the India-Asia collision. Earth and Planetary Science Letters, 86(2), 240–252. https://doi.org/10.1016/0012-821X(87)90224-X

De Yoreo, J. J., Lux, D. R., & Guidotti, C. V. (1989). The role of crustal anatexis and magma migration in the thermal evolution of regions of thickened continental crust. Geological Society, London, Special Publications, 43(1), 187–202. https://doi.org/10.1144/GSL.SP.1989.043.01.12

DePaolo, D. J., & Wasserburg, G. J. (1976). Nd isotopic variations and petrogenetic models. Geophysical Research Letters, 3(5), 249–252. https://doi.org/10.1029/GL003i005p00249

DePaolo, Donald J. (1981). Trace element and isotopic effects of combined wallrock assimilation and fractional crystallization. Earth and Planetary Science Letters, 53(2), 189–202. https://doi.org/10.1016/0012-821X(81)90153-9

DePaolo, Donald J., Perry, F. V., & Baldridge, W. S. (1992). Crustal versus mantle sources of granitic magmas: a two-parameter model based on Nd isotopic studies. Earth and Environmental Science Transactions of The Royal Society of Edinburgh, 83(1–2), 439–

446. https://doi.org/10.1017/S0263593300008117

DePaolo, D.J., Harrison, T.M., Wielicki, M., Zhao, Z.D., Zhu, D.C., Zhang, H., & Mo, X.X., (2019). Geochemical evidence for thin syn-collision crust and major crustal thickening between 45 and 32 Ma at the southern margin of Tibet. Gondwana Research. https://doi.org/ 10.1016/j.gr.2019.03.011

Dewey, J.F., Shackleton, R.M., Chang, C.F., & Sun, Y.Y., (1988). The tectonic evolution of the Tibetan Plateau. Philosophical Transactions of the Royal Society of London. Series A, Mathematical and Physical Sciences, 327(1594), 379–413. https://doi.org/10.1098/rsta.1988.0135

Eiler, J. M. (2001). Oxygen Isotope Variations of Basaltic Lavas and Upper Mantle Rocks. Reviews in Mineralogy and Geochemistry, 43(1), 319–364. https://doi.org/10.2138/gsrmg.43.1.319

England, P., & Houseman, G. (1986). Finite strain calculations of continental deformation: 2. Comparison with the India-Asia Collision Zone. Journal of Geophysical Research: Solid Earth, 91(B3), 3664–3676. https://doi.org/10.1029/JB091iB03p03664

England, P., & McKenzie, D. (1982). A thin viscous sheet model for continental deformation. Geophysical Journal of the Royal Astronomical Society, 70(2), 295–321. https://doi.org/10.1111/j.1365-246X.1982.tb04969.x

England, P., & Searle, M. (1986). The Cretaceous-tertiary deformation of the Lhasa Block and its implications for crustal thickening in Tibet. Tectonics, 5(1), 1–14. https://doi.org/10.1029/TC005i001p00001

Farner, M. J., & Lee, C. T. A. (2017). Effects of crustal thickness on magmatic differentiation in

subduction zone volcanism: A global study. Earth and Planetary Science Letters, 470, 96–107. https://doi.org/10.1016/j.epsl.2017.04.025

Ferriss, E. D. A., Essene, E. J., & Becker, U. (2008). Computational study of the effect of pressure on the Ti-in-zircon geothermometer. European Journal of Mineralogy, 20(5), 745–755. https://doi.org/10.1127/0935-1221/2008/0020-1860

Ferry, J. M., & Watson, E. B. (2007). New thermodynamic models and revised calibrations for the Ti-in-zircon and Zr-in-rutile thermometers. Contributions to Mineralogy and Petrology, 154(4), 429–437. https://doi.org/10.1007/s00410-007-0201-0

Finch, R. J., & Hanchar, J. M. (2003). Structure and Chemistry of Zircon and Zircon-Group Minerals. Reviews in Mineralogy and Geochemistry, 53(1), 1–25. https://doi.org/10.2113/0530001

Gregory, R. T., & Taylor, H. P. (1981). An oxygen isotope profile in a section of Cretaceous oceanic crust, Samail Ophiolite, Oman: Evidence for $\delta^{18}O$ buffering of the oceans by deep (>5 km) seawater-hydrothermal circulation at mid-ocean ridges. Journal of Geophysical Research: Solid Earth, 86(B4), 2737–2755. https://doi.org/10.1029/JB086iB04p02737

Gromet, L. P., & Silver, L. T. (1983). Rare earth element distributions among minerals in a granodiorite and their petrogenetic implications. Geochimica et Cosmochimica Acta, 47(5), 925–939. https://doi.org/10.1016/0016-7037(83)90158-8

Hammersley, L., & DePaolo, D. J. (2006). Isotopic and geophysical constraints on the structure and evolution of the Clear Lake volcanic system. Journal of Volcanology and Geothermal

Research, 153(3–4), 331–356. https://doi.org/10.1016/j.jvolgeores.2005.12.003

Harrison, T. M., Aikman, A., Holden, P., Walker, A. M., McFarlane, C., Rubatto, D., et al.(2005). Testing the Ti-in-Zircon Thermometer. AGU Fall Meeting Abstracts, 41, V41F-1540.

Harrison, T. M., Wielicki, M. M., Lovera, O. M., DePaolo, D. J., Zhu, D.C., Zhao, Z., et al. (2014). Testing tectonic models using time-varying crustal thickness variations across Southern Tibet. Paper presented at GSA Annual Meeting, Vancouver, B.C.

Harrison, T. M., Yin, A., Grove, M., Lovera, O. M., Ryerson, F. J., & Zhou, X. (2000). The Zedong Window: A record of superposed Tertiary convergence in southeastern Tibet. Journal of Geophysical Research: Solid Earth, 105(B8), 19211–19230. https://doi.org/10.1029/2000JB900078

Harrison, T. Mark, Schmitt, A. K., McCulloch, M. T., & Lovera, O. M. (2008). Early (≥4.5 Ga) formation of terrestrial crust: Lu–Hf, $\delta^{18}O$, and Ti thermometry results for Hadean zircons. Earth and Planetary Science Letters, 268(3), 476–486. https://doi.org/10.1016/j.epsl.2008.02.011

Hawkesworth, C. J., & Kemp, A. I. S. (2006). Using hafnium and oxygen isotopes in zircons to unravel the record of crustal evolution. Chemical Geology, 226(3), 144–162. https://doi.org/10.1016/j.chemgeo.2005.09.018

Houseman, G. A., McKenzie, D. P., & Molnar, P. (1981). Convective instability of a thickened boundary layer and its relevance for the thermal evolution of continental convergent belts. Journal of Geophysical Research: Solid Earth, 86(B7), 6115–6132.

https://doi.org/10.1029/JB086iB07p06115

Ingalls, M., Rowley, D. B., Currie, B., & Colman, A. S. (2016). Large-scale subduction of continental crust implied by India–Asia mass-balance calculation. Nature Geoscience, 9(11), 848. https://doi.org/10.1038/ngeo2806

Ito, E., White, W. M., & Göpel, C. (1987). The O, Sr, Nd and Pb isotope geochemistry of MORB. Chemical Geology, 62(3), 157–176. https://doi.org/10.1016/0009-2541(87)90083-0

Ji, W.Q., Wu, F.Y., Chung, S.L., Li, J.X., & Liu, C.Z. (2009). Zircon U–Pb geochronology and Hf isotopic constraints on petrogenesis of the Gangdese batholith, southern Tibet. Chemical Geology, 262(3), 229–245. https://doi.org/10.1016/j.chemgeo.2009.01.020

Ji, W.Q., Wu, F.Y., Chung, S.L., Wang, X.C., Liu, C.Z., Li, Q.L., et al. (2016). Eocene Neo-Tethyan slab breakoff constrained by 45 Ma oceanic island basalt–type magmatism in southern Tibet. Geology, 44(4), 283–286. https://doi.org/10.1130/G37612.1

Jochum, K., Weis, U., Stoll, B., Kuzmin, D., Jacob, D., Stracke, A., et al. (2011). Determination of reference values for NIST SRM 610–617 glasses following ISO Guidelines (Vol. 35). https://doi.org/10.1111/j.1751-908X.2011.00120.x

Johnson, D. M., Hooper, P. R., & Conrey, R. M. (1999). XRF Analysis of Rocks and Minerals for Major and Trace Elements on a Single Low Dilution Li-tetraborate Fused Bead. Advances in X-Ray Analysis, 41, 843–867.

Johnson, M.R.W. (2002) Shortening budgets and the role of continental subduction during the India-Asia collision. Earth-Science Reviews, 59(1-4), 101-123.

Kapp, J. L. D., Harrison, T. M., Kapp, P., Grove, M., Lovera, O. M., & Lin, D. (2005).

Nyainqentanglha Shan: A window into the tectonic, thermal, and geochemical evolution of the Lhasa block, southern Tibet. Journal of Geophysical Research: Solid Earth, 110(B8). https://doi.org/10.1029/2004JB003330

Kapp, P., Manning, C. E., & Tropper, P. (2009). Phase-equilibrium constraints on titanite and rutile activities in mafic epidote amphibolites and geobarometry using titanite–rutile equilibria. Journal of Metamorphic Geology, 27(7), 509–521. https://doi.org/10.1111/j.1525-1314.2009.00836.x

Kemp, A. I. S., Hawkesworth, C. J., Foster, G. L., Paterson, B. A., Woodhead, J. D., Hergt, J. M., Gray, C.M., & Whitehouse, M.J. (2007). Magmatic and Crustal Differentiation History of Granitic Rocks from Hf-O Isotopes in Zircon. Science, 315(5814), 980–983. https://doi.org/10.1126/science.1136154

Kidd, W. S. F., Yusheng, P., Chengfa, C., Coward, M. P., Dewey, J. F., Gansser, A., et al. (1988). Geological mapping of the 1985 Chinese—British Tibetan (Xizang—Qinghai) Plateau Geotraverse route. Phil. Trans. R. Soc. Lond. A, 327(1594), 287–305. https://doi.org/10.1098/rsta.1988.0130

King, E. M., Barrie, C. T., & Valley, J. W. (1997). Hydrothermal alteration of oxygen isotope ratios in quartz phenocrysts, Kidd Creek mine, Ontario: Magmatic values are preserved in zircon. Geology, 25(12), 1079–1082. https://doi.org/10.1130/0091-7613(1997)025<1079:HAOOIR>2.3.CO;2

Kinny, P. D., & Maas, R. (2003). Lu–Hf and Sm–Nd isotope systems in zircon. Reviews in Mineralogy and Geochemistry, 53(1), 327–341. https://doi.org/10.2113/0530327

Klaver, M., Blundy, J. D., & Vroon, P. Z. (2018). Generation of arc rhyodacites through

cumulate-melt reactions in a deep crustal hot zone: Evidence from Nisyros volcano. Earth and Planetary Science Letters, 497, 169–180. https://doi.org/10.1016/j.epsl.2018.06.019

Kong, X., Yin, A., & Harrison, T. M. (1997). Evaluating the role of preexisting weaknesses and topographic distributions in the Indo-Asian collision by use of a thin-shell numerical model. Geology, 25(6), 527–530. https://doi.org/10.1130/0091-7613(1997)025<0527:ETROPW>2.3.CO;2

Kong, X., & Bird, P. (1995). SHELLS: A thin-shell program for modeling neotectonics of regional or global lithosphere with faults. Journal of Geophysical Research: Solid Earth, 100(B11), 22129–22131. https://doi.org/10.1029/95JB02435

Lackey, J. S., Cecil, M. R., Windham, C. J., Frazer, R. E., Bindeman, I. N., & Gehrels, G. E. (2012). The Fine Gold Intrusive Suite: The roles of basement terranes and magma source development in the Early Cretaceous Sierra Nevada batholith. Geosphere, 8(2), 292–313. https://doi.org/10.1130/GES00745.1

Le Fort, P. (1996). Evolution of the Himalaya. In T. M. Harrison & A. Yin (Eds.), The Tectonics of Asia (pp. 95–106). Cambridge University Press.

Lee, C.T. A., Thurner, S., Paterson, S., & Cao, W. (2015). The rise and fall of continental arcs: Interplays between magmatism, uplift, weathering, and climate. Earth and Planetary Science Letters, 425, 105–119. https://doi.org/10.1016/j.epsl.2015.05.045

Leech, M. L., Singh, S., Jain, A. K., Klemperer, S. L., & Manickavasagam, R. M. (2005). The onset of India–Asia continental collision: Early, steep subduction required by the timing of UHP metamorphism in the western Himalaya. Earth and Planetary Science Letters,

234(1), 83–97. https://doi.org/10.1016/j.epsl.2005.02.038

Leier, A. L., Kapp, P., Gehrels, G. E., & DeCelles, P. G. (2007). Detrital zircon geochronology of Carboniferous–Cretaceous strata in the Lhasa terrane, Southern Tibet. Basin Research, 19(3), 361–378. https://doi.org/10.1111/j.1365-2117.2007.00330.x

Lovera, O. M., Harrison, M., Schmitt, A. K., Wielicki, M. M., & Tierney, C. R. (2015). Numerical Simulation of Magma Reservoirs to Interpret Chrono-Chemical Signal. Paper presented at the AGU Fall Meeting, San Francisco, CA.

McNulty, B. A., Tobisch, O. T., Cruden, A. R., & Gilder, S. (2000). Multistage emplacement of the Mount Givens pluton, central Sierra Nevada batholith, California. GSA Bulletin, 112(1), 119–135. https://doi.org/10.1130/0016-7606(2000)112<119:MEOTMG>2.0.CO;2

Mo, X.X., Dong, G., Zhao, Z.D., Zhou, S., Wang, L. L., Qiu, R. Z., & Zhang, F. Q. (2005). Spatial and temporal distribution and characteristics of granitoids in the Gangdese, Tibet and implication for crustal growth and evolution. Geological Journal of China Universities, 11(3), 281–290.

Mo, X.X., Hou, Z., Niu, Y., Dong, G., Qu, X., Zhao, Z. and Yang, Z., (2007). Mantle contributions to crustal thickening during continental collision: evidence from Cenozoic igneous rocks in southern Tibet. Lithos, 96(1-2), 225-242.

Mojzsis, S. J., Harrison, T. M., & Pidgeon, R. T. (2001). Oxygen-isotope evidence from ancient zircons for liquid water at the Earth's surface 4,300 Myr ago. Nature, 409(6817), 178–181. https://doi.org/10.1038/35051557

Moyen, J.F. (2009). High Sr/Y and La/Yb ratios: The meaning of the "adakitic signature".

Lithos, 112(3), 556-574. http://doi.org/10.1016/j.lithos.2009.04.001

Murphy, M. A., Yin, A., Harrison, T. M., Dürr, S. B., Chen, Z., Ryerson, F. J., Kidd, W.S.F., et al. (1997). Did the Indo-Asian collision alone create the Tibetan plateau? Geology, 25(8), 719–722. https://doi.org/10.1130/0091-7613(1997)025<0719:DTIACA>2.3.CO;2

Nábělek, J., Hetényi, G., Vergne, J., Sapkota, S., Kafle, B., Jiang, M., et al. (2009). Underplating in the Himalaya-Tibet Collision Zone Revealed by the Hi-CLIMB Experiment. Science, 325(5946), 1371–1374. https://doi.org/10.1126/science.1167719

Paces, J. B., & Miller, J. D. (1993). Precise U-Pb ages of Duluth Complex and related mafic intrusions, northeastern Minnesota: Geochronological insights to physical, petrogenetic, paleomagnetic, and tectonomagmatic processes associated with the 1.1 Ga Midcontinent Rift System. Journal of Geophysical Research: Solid Earth, 98(B8), 13997–14013. https://doi.org/10.1029/93JB01159

Patchett, P. J., Kouvo, O., Hedge, C. E., & Tatsumoto, M. (1982). Evolution of continental crust and mantle heterogeneity: Evidence from Hf isotopes. Contributions to Mineralogy and Petrology, 78(3), 279–297. https://doi.org/10.1007/BF00398923

Pearce, J. A. (1996). Sources and settings of granitic rocks. Episodes, 19(4), 120–125. https://doi.org/10.1111/j.1751-908X.2011.00120.x

Peltzer, G., & Saucier, F. (1996). Present-day kinematics of Asia derived from geologic fault rates. Journal of Geophysical Research: Solid Earth, 101(B12), 27943–27956. https://doi.org/10.1029/96JB02698

Peltzer, G., & Tapponnier, P. (1988). Formation and evolution of strike-slip faults, rifts, and basins during the India-Asia Collision: An experimental approach. Journal of

Geophysical Research: Solid Earth, 93(B12), 15085–15117. https://doi.org/10.1029/JB093iB12p15085

Profeta, L., Ducea, M. N., Chapman, J. B., Paterson, S. R., Gonzales, S. M. H., Kirsch, M., et al. (2015). Quantifying crustal thickness over time in magmatic arcs. Scientific Reports, 5, 17786. https://doi.org/10.1038/srep17786

Quidelleur, X., Grove, M., Lovera, O. M., Harrison, T. M., Yin, A., & Ryerson, F. J. (1997). Thermal evolution and slip history of the Renbu Zedong Thrust, southeastern Tibet. Journal of Geophysical Research: Solid Earth, 102(B2), 2659–2679. https://doi.org/10.1029/96JB02483

Rapp, R. P., & Watson, E. B. (1986). Monazite solubility and dissolution kinetics: implications for the thorium and light rare earth chemistry of felsic magmas. Contributions to Mineralogy and Petrology, 94(3), 304–316. https://doi.org/10.1007/BF00371439

Rapp, R. P., Shimizu, N., & Norman, M. D. (2003). Growth of early continental crust by partial melting of eclogite. Nature, 425(6958), 605–609. https://doi.org/10.1038/nature02031

Reiners, P. W., Nelson, B. K., & Ghiorso, M. S. (1995). Assimilation of felsic crust by basaltic magma: Thermal limits and extents of crustal contamination of mantle-derived magmas. Geology, 23(6), 563–566. https://doi.org/10.1130/0091-7613(1995)023<0563:AOFCBB>2.3.CO;2

Rothstein, D. A., & Manning, C. E. (2003). Geothermal gradients in continental magmatic arcs: Constraints from the eastern Peninsular Ranges batholith, Baja California, México. In Tectonic Evolution of Northwestern México and the Southwestern USA (Vol. 374).

Geological Society of America.

Rowley, D. B. (1996). Age of initiation of collision between India and Asia: A review of stratigraphic data. Earth and Planetary Science Letters, 145(1), 1–13. https://doi.org/10.1016/S0012-821X(96)00201-4

Simon, J. I., Weis, D., DePaolo, D. J., Renne, P. R., Mundil, R., & Schmitt, A. K. (2014). Assimilation of preexisting Pleistocene intrusions at Long Valley by periodic magma recharge accelerates rhyolite generation: rethinking the remelting model. Contributions to Mineralogy and Petrology, 167(1), 955. https://doi.org/10.1007/s00410-013-0955-5

Tapponnier, P., Mercier, J. L., Proust, F., Andrieux, J., Armijo, R., Bassoullet, J. P., et al. (1981). The Tibetan side of the India–Eurasia collision. Nature, 294(5840), 405–410. https://doi.org/10.1038/294405a0

Trail, D., Mojzsis, S. J., Harrison, T. M., Schmitt, A. K., Watson, E. B., & Young, E. D. (2007). Constraints on Hadean zircon protoliths from oxygen isotopes, Ti-thermometry, and rare earth elements. Geochemistry, Geophysics, Geosystems, 8(6), Q06014. https://doi.org/10.1029/2006GC001449

Trail, D., Bindeman, I. N., Watson, E. B., & Schmitt, A. K. (2009). Experimental calibration of oxygen isotope fractionation between quartz and zircon. Geochimica et Cosmochimica Acta, 73(23), 7110–7126. https://doi.org/10.1016/j.gca.2009.08.024

Valley, J. W. (2003). Oxygen Isotopes in Zircon. Reviews in Mineralogy and Geochemistry, 53(1), 343–385. https://doi.org/10.2113/0530343

Vervoort, J. D., & Blichert-Toft, J. (1999). Evolution of the depleted mantle: Hf isotope evidence from juvenile rocks through time. Geochimica et Cosmochimica Acta, 63(3), 533–556.

https://doi.org/10.1016/S0016-7037(98)00274-9

Walker, B. A., Miller, C. F., Lowery Claiborne, L., Wooden, J. L., & Miller, J. S. (2007). Geology and geochronology of the Spirit Mountain batholith, southern Nevada: Implications for timescales and physical processes of batholith construction. Journal of Volcanology and Geothermal Research, 167(1), 239–262. https://doi.org/10.1016/j.jvolgeores.2006.12.008

Watson, E. B., & Cherniak, D. J. (1997). Oxygen diffusion in zircon. Earth and Planetary Science Letters, 148(3), 527–544. https://doi.org/10.1016/S0012-821X(97)00057-5

Watson, E. B., & Harrison, T. M. (1984). Accessory minerals and the geochemical evolution of crustal magmatic systems: a summary and prospectus of experimental approaches. Physics of the Earth and Planetary Interiors, 35(1), 19–30. https://doi.org/10.1016/0031-9201(84)90031-1

Watson, E. B., & Harrison, T. M. (2005). Zircon Thermometer Reveals Minimum Melting Conditions on Earliest Earth. Science, 308(5723), 841–844. https://doi.org/10.1126/science.1110873

Weis, D., Kieffer, B., Hanano, D., Nobre Silva, I., Barling, J., Pretorius, W., et al. (2007). Hf isotope compositions of U.S. Geological Survey reference materials. Geochemistry, Geophysics, Geosystems, 8(6), Q06006. https://doi.org/10.1029/2006GC001473

Wiebe, R. A., & Collins, W. J. (1998). Depositional features and stratigraphic sections in granitic plutons: implications for the emplacement and crystallization of granitic magma. Journal of Structural Geology, 20(9), 1273–1289. https://doi.org/10.1016/S0191-8141(98)00059-

5

Wiedenbeck, M., Hanchar, J. M., Peck, W. H., Sylvester, P., Valley, J., Whitehouse, M., et al. (2004). Further Characterization of the 91500 Zircon Crystal. Geostandards and Geoanalytical Research, 28(1), 9–39. https://doi.org/10.1111/j.1751-908X.2004.tb01041.x

Wood, S.A. & Ricketts, A. (2000). Allanite –(Ce) from the Eocene Casto granite, Idaho: Response to hydrothermal alteration. The Canadian Mineralogist, 38(1), 81-100. https://doi.org/10.2113/gscanmin.38.1.81

Woodhead, J. D., & Hergt, J. M. (2005). A Preliminary Appraisal of Seven Natural Zircon Reference Materials for In Situ Hf Isotope Determination. Geostandards and Geoanalytical Research, 29(2), 183–195. https://doi.org/10.1111/j.1751-908X.2005.tb00891.x

Yin, A., & Harrison, T. M. (2000). Geologic Evolution of the Himalayan-Tibetan Orogen. Annual Review of Earth and Planetary Sciences, 28(1), 211–280. https://doi.org/10.1146/annurev.earth.28.1.211

York, D., Evensen, N. M., Martínez, M. L., & De Basabe Delgado, J. (2004). Unified equations for the slope, intercept, and standard errors of the best straight line. American Journal of Physics, 72(3), 367–375. https://doi.org/10.1119/1.1632486

Zhang, Z., Dong, X., Xiang, H., Ding, H., He, Z., & Liou, J. G. (2015). Reworking of the Gangdese magmatic arc, southeastern Tibet: post-collisional metamorphism and anatexis. Journal of Metamorphic Geology, 33(1), 1–21. https://doi.org/10.1111/jmg.12107

Zhu, D.C., Mo, X.X., Niu, Y., Zhao, Z.D., Wang, L.Q., Pan, G.T., et al. (2009). Zircon U–Pb

dating and in-situ Hf isotopic analysis of Permian peraluminous granite in the Lhasa terrane, southern Tibet: Implications for Permian collisional orogeny and paleogeography. Tectonophysics, 469(1), 48–60. https://doi.org/10.1016/j.tecto.2009.01.017

Zhu, D.C., Zhao, Z.D., Niu, Y., Mo, X.X., Chung, S.L., Hou, Z.Q., et al. (2011). The Lhasa Terrane: Record of a microcontinent and its histories of drift and growth. Earth and Planetary Science Letters, 301(1), 241–255. https://doi.org/10.1016/j.epsl.2010.11.005

Zhu, D.C., Wang, Q., Zhao, Z.D., Chung, S.L., Cawood, P. A., Niu, Y., et al. (2015). Magmatic record of India-Asia collision. Scientific Reports, 5, srep14289. https://doi.org/10.1038/srep14289

Zhu, D.C., Wang, Q., Cawood, P. A., Zhao, Z.D., & Mo, X.X. (2017). Raising the Gangdese Mountains in southern Tibet. Journal of Geophysical Research: Solid Earth, 122(1), 214–223. https://doi.org/10.1002/2016JB013508

Zurek, B., Meltzer, A., & Sol, S. (2007). Metamorphism and deformation of the lower crust and crust-mantle interface at the eastern syntaxis of Tibet derived from converted seismic waves. T22C-05. Paper presented at the AGU Fall Meeting, San Francisco, CA.

– Chapter 3 –

Trace Element "Pseudobarometers"

3.1 Introduction

3.1.1 What are "pseudobarometers"?

Recent studies of global geochemical databases of arc volcanics have found an empirical correlation between the ratios of whole-rock concentrations of La/Yb, Gd/Yb, and Sr/Y; and estimated crustal thickness (Chapman et al., 2015; Chiaradia, 2015; Profeta et al., 2015; Farner & Lee, 2017; Hu et al., 2017). Profeta et al. (2015) named these ratios "pseudobarometers" as they are indirect proxies for the pressure, and therefore depth, of formation of arc magmas. The aforementioned studies infer that these ratios change with crustal thickness as a result of variable partitioning of these elements into pressure-dependent phase assemblages during partial melting of fertilized mantle wedge under an arc.

Traditional thermobarometers employ pressure- and temperature-dependence of phase equilibria or mineral composition to calculate *P* and *T* of formation, using equilibrium thermodynamics of balanced reactions between phase assemblages or endmember mineral compositions. This is achieved either by applying experimentally constrained thermodynamic data for pure phases to calculate *P* and *T* conditions necessary for naturally-observed solid solution in one or more minerals (e.g. Mercier, 1980; Putirka et al., 1996; Dale et al., 2000; Watson & Harrison, 2005; Thomas et al., 2010), or with forward calculation of "pseudosections": *P-T* phase diagrams predicting mineral assemblages for a discrete composition as pressure and temperature vary (e.g. Powell & Holland, 1988, 2008; Connolly, 1990, 2005). These pseudosections are then compared to naturally occurring phase assemblages to constrain the range of *P* and *T* of rock formation.

Pseudobarometers, by contrast, are not based on balanced thermodynamic reactions, but rather an empirical association between whole-rock composition and crustal thickness, with

inferred associations between phase stabilities and their experimentally constrained partition coefficients for the elements of interest. In this chapter I examine the reliability of these pseudobarometers and their pitfalls when applied to individual case studies, in particular their applicability to the India-Asia collision.

3.2 Geologic basis of pseudobarometers

3.2.1 Empirical evidence

Sr/Y Models

Chiaradia (2015) identified an empirical correlation between the ratio of Sr/Y and crustal thickness for low-MgO (2-6 wt%), low Fe_2O_{3tot} (<8 wt%) lavas in young arcs. They used crustal thickness estimates from Zellmer (2008) and compiled data from GEOROC (Sarbas et al., 2019). Chiaradia took median values of Sr/Y for 22 Pliocene-Quaternary arcs in incremental batches of 0.5 wt% MgO, which were then averaged (Fig. 3.1). Notably, these "averages of median values" often do not overlap with the highest-density regions for $n \approx 10^4$ subsets of the database when sorted by crustal thickness. Sr/Y values range from 0-60 in arcs <20 km thick, and 0-100 in arcs >30 km thick. Additionally, the largest continental arc invoked in this study, the Central Andes, deviates greatly from the overall pattern, with much greater crustal thicknesses for given Sr/Y values relative to all other arcs. The deviation of Central Andes data imply that Sr/Y values for mature continental arcs akin to the Gangdese Arc–which preceded the Tibetan-Himalayan orogen–may be a less reliable proxy for crustal thickness when calibrated against smaller and younger arcs.

Profeta et al. (2015) and Chapman et al. (2015) used a similar dataset to Chiaradia (2015) to derive an empirical model that estimates depth of the Mohorovičić discontinuity (Moho) based on Sr/Y. They use GEOROC data from 25 Pliocene-Quaternary arcs (Sarbas et al., 2019),

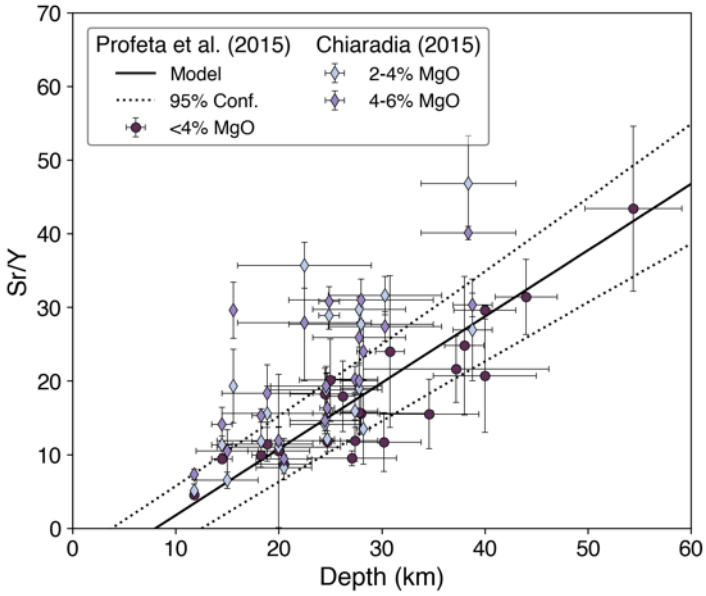

Figure 0.1: Data from Chiaradia (2015) (CA, diamonds) and Profeta et al. (2015) (PR, circles), divided by whole-rock MgO (wt. %). Error bars are 1σ. Solid line is Eq. (1), the linear regression of PR, with 95% confidence interval as dotted lines. CA data includes a wider range of SiO2 than PR, which is restricted to 55-68 wt. %.

filtered to include only low-Mg intermediate calc-alkaline rocks with <4 wt.% MgO and 55-68 wt.% SiO_2, and excluded data from the Central Andes Volcanic Zone (CCVZ) due to the presence of the Altiplano Puna magma body–though they do not elaborate on its exclusion. They removed outliers and calculated median and standard deviation values of Sr/Y, and compiled crustal thickness (Moho depth) estimates from Dimalanta et al., 2002; Eberhart-Phillips et al., 2006; Yuan et al., 2006; Zellmer, 2008; Laske et al., 2013; and Lücke, 2014. They assumed isostatic equilibrium and an average crustal density of 2700 kg m^{-3} to calculate crustal thickness based on average elevations of areas with stratovolcanoes in each arc. They find a linear relationship between Moho depth in km (dm) and Sr/Y,

$$Sr/Y = a \cdot \mathrm{dm} - b \quad (1)$$

which can be rearranged to solve for dm with a known value of Sr/Y:

$$\mathrm{dm} = \frac{Sr/Y - b}{a} \quad (2)$$

Both studies use ordinary least-squares linear regression, with a = 0.90±0.06 and b = –7.25±1.89; R^2 = 0.90.

Profeta et al. (2015) assert their calibration can be used to reconstruct paleo-crustal

thickness using the Sr/Y ratios of rocks from ancient arcs that fall within the stipulated compositional range. Exclusion of the CCVZ data, however, implies that this model is disfavored for igneous rocks produced in conditions similar to those underlying the Altiplano-Puna volcanic complex (APVC). The APVC is associated with steepening slab dip causing decompression melting and high mantle heat flow (Babeyko et al., 2002; Ouimet & Cook, 2010); resultant juvenile basaltic melts assimilated with weak, hot crustal material to create ignimbrite lavas with ca. 1:1 mantle-to-crust source ratio (Kay et al., 2010). It is therefore possible that such conditions produce anomalous Sr/Y relative to typical young arcs (see §3.2.2 and §3.5.1).

Hu et al. (2017) expanded on the work of Chapman et al. (2015) and Profeta et al. (2015) by performing a similar calibration for Sr/Y in young (Miocene-present) rocks from continental

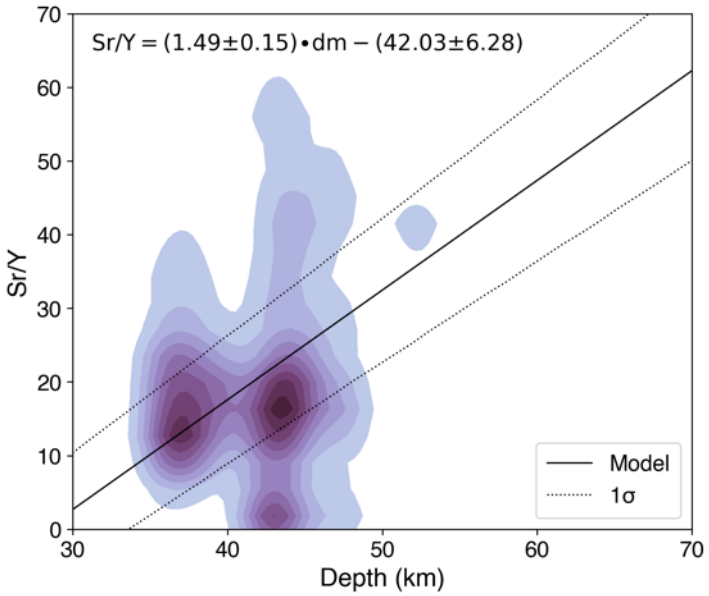

Figure 0.2: Sr/Y model of Hu et al. (2017) plotted with a KDE of the natural data used t calibrate the model (n = 1277). Model confidence interval was calculated with a Monte Carlo simulation of the uncertainties c the regression coefficients.

collision zones. They observed that collisional samples generally had Sr/Y lower than arc samples for a given dm when dm< 60 km; their regression followed the same form as **Eq. (1)** with a = 1.49±0.15 and b = –42.03±6.28; R^2 = 0.91. When Sr/Y = 0, for the collisional model dm ≈ 28 km, while for the arc model dm ≈8 km. While these numbers are not geologically meaningful *sensu stricto*, they hint that differing geochemical partitioning processes occur during

magma genesis in arcs relative to continental collision.

La/Yb Models

Profeta et al. (2015) and Farner & Lee (2017) evaluate the association between La/Yb and crustal thickness, again in Pliocene-Quaternary arcs. The median values of La/Yb_N and crustal thickness (Moho depth in km) were regressed by nonlinear least squares with an exponential fit of the form:

$$La/Yb_N = Ae^{B \cdot \mathrm{dm}} \tag{3}$$

which can be rearranged to solve for dm with a known value of La/Yb_N:

$$dm = \frac{\ln\left(\frac{La}{Yb_N}/\mathrm{A}\right)}{\mathrm{B}} \tag{4}$$

Profeta et al. (2015) used the same methodology described in §3.2.1.1 to calculate crustal thicknesses and median and standard deviation values of La/YbN, where La/YbN is the ratio of whole-rock concentrations of La and Yb normalized to chondritic abundance. Farner & Lee (2017) compiled GEOROC data of Pleistocene-Holocene arc volcanic rocks and use the un-normalized whole-rock ratio of La/Yb; i.e. La/Yb is uniformly a factor of 1.48 higher than the values used by Profeta et al. (2015). They also estimated crustal thickness from elevation, assuming isostatic equilibrium, though they assume average crustal density of 2870 kg m-3, compared to 2700 kg m-3 used by Profeta et al. Farner & Lee acknowledged that sampling bias could affect the calculated relationship between La/Yb and dm, as readily accessible sampling sites in a given arc will be overrepresented in the raw dataset. Rather than grouping values of La/Yb by their arc source, they computed median and mean values for 100 m elevation bins, calculated using a digital elevation model with 100 km2 grid spacing to filter small-lengthscale,

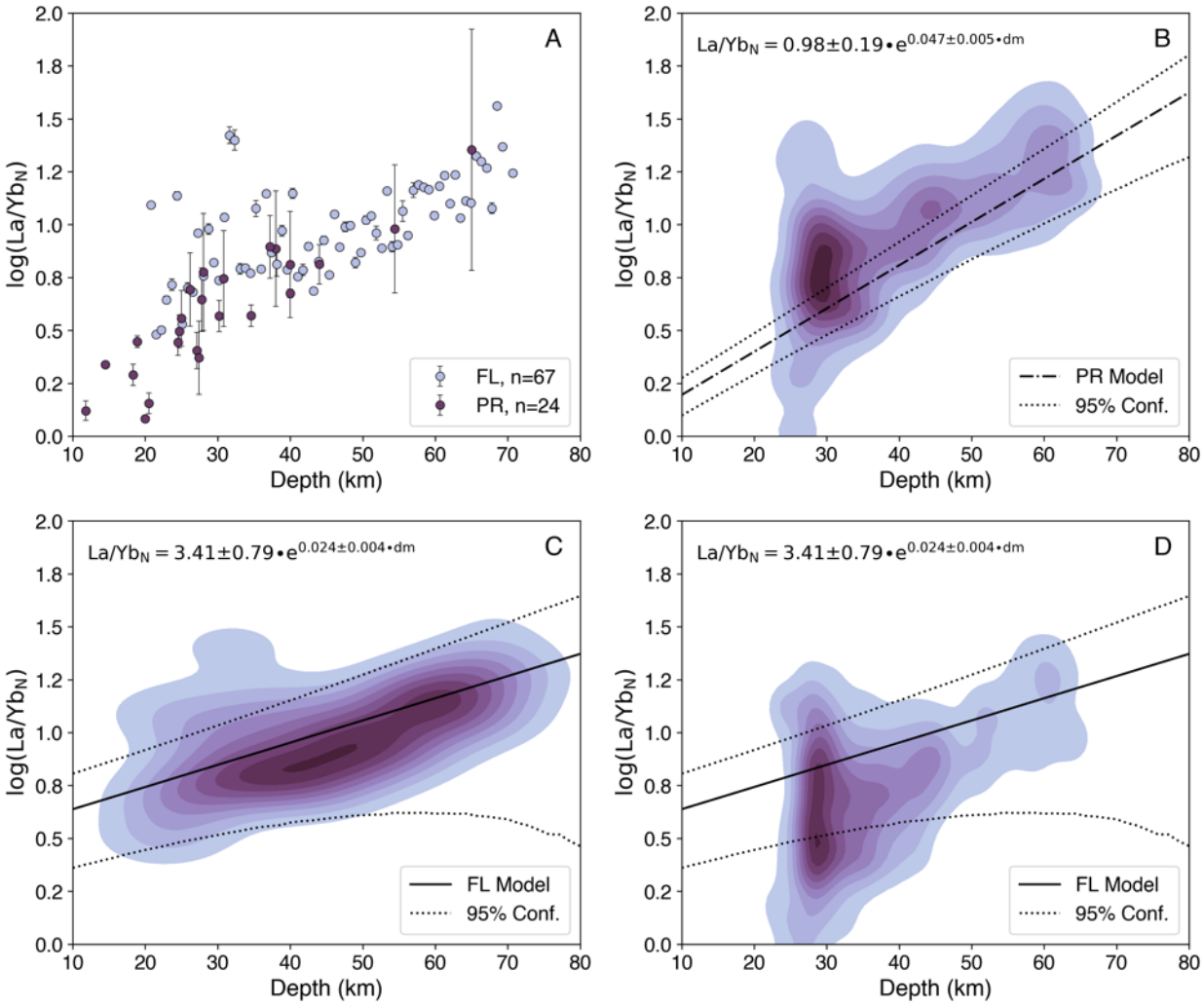

Figure 0.3: Empirical data and models for Moho depth vs. La/Yb_N. Data from Farner & Lee, 2017 (FL) and Profeta et al., 2015 (PR). FL data were converted to La/Yb_N for comparison. (A) Median values of La/Yb with 1σ error bars; FL data are for 100 m elevation intervals; PR data are for each of 22 arcs. (B) Kernel density estimation of arc data filtered for 55% < SiO_2 < 68% and MgO < 4%, plotted with PR model fit and 95% confidence interval. (C) FL median data from 100 m elevation bins, plotted with FL model and 95% confidence interval of fit. (D) All data from arcs, unfiltered, with model as in (C). Note that the FL model fit is calculated from the median values (plotted in (A) as points and (C) as KDE); the model is therefore an inferior fit to the bulk data.

non-isostatic topography.

In order to directly compare Farner & Lee to Profeta et al.'s model, Farner & Lee's La/Yb data can be converted to their equivalent chondrite-normalized values, La/Yb_N. Using the medians and standard deviations of Farner & Lee's elevation bin data, with corresponding calculated crustal thicknesses, the relationship between dm and La/Yb_N follows the same

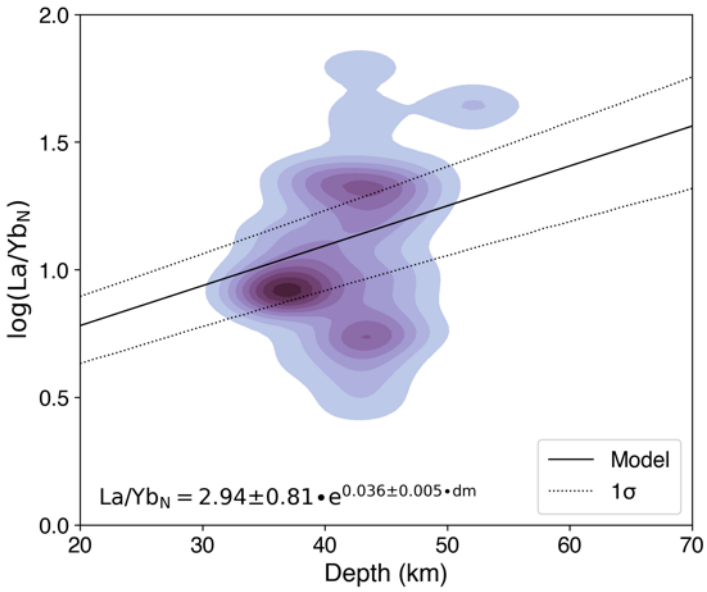

Figure 0.4: La/Yb$_N$ model of Hu et al. (2017) plotted with a KDE of the natural data used to calibrate the model (n = 1277). Model confidence interval was calculated with a Monte Carlo simulation of the uncertainties on the regression coefficients.

functional form of Eq. 3. The two fits are shown in Fig. 3.3; 95% confidence interval of the model fits plotted were calculated using a Monte Carlo simulation of model coefficients and their standard deviations. Because both Farner & Lee (2017) and Profeta et al. (2015) calibrated their models on median data rather than the entire dataset, the 95% confidence intervals in Fig. 3.3b

and (D) do not actually include 95% of the data.

Hu et al. (2017) additionally calculated the relationship of La/Yb_N and dm for young collisional samples, from a dataset of 830 natural samples from 25 locations. Like Profeta et al. (2015), their model is calculated using the median and standard deviation values of each locality. Unlike their Sr/Y calibration, they found that La/Yb_N was offset to higher values for collisional samples relative to Profeta et al. (2015)'s and Farner & Lee (2017)'s calibrations (Fig. 3.5a). Samples from collisional terranes would therefore yield an unreasonably high value for dm if Farner & Lee (2017) or Profeta et al. (2015)'s arc-based La/Yb models were used.

3.2.2 Experimental constraints

There is a clear empirical relationship between crustal thickness and La/Yb and Sr/Y. The aforementioned studies invoke the partition coefficients of these elements in phases whose stability is dependent on *P*. The partition coefficient is the ratio of the concentration of a given component *i* in the mineral (*m*) relative to a coexisting liquid (*l*): $D_i = C_m/C_l$. In this section I will review the experimental evidence for the temperature, pressure, and compositional effects of

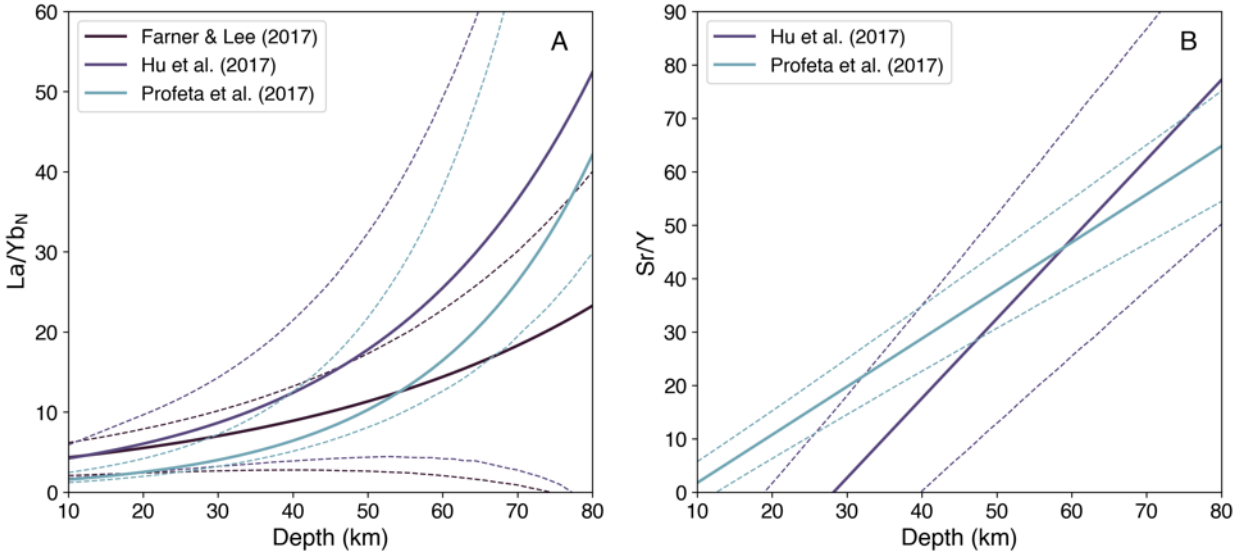

Figure 0.5: All pseudobarometer models for La/Yb_N (A) and Sr/Y (B), with 95% confidence intervals (dashed lines) calculated by Monte Carlo simulation with the model coefficients and their uncertainties.

D_i in the phases that potentially control these ratios.

Garnet, a common lower-crustal and upper-mantle mineral that is stable beginning at ca. 10 kbar in metapelites (Hensen & Green, 1971) and beginning at ca. 20 kbar in pyrolite (Green & Ringwood, 1967), is typically invoked as the main control on pseudobarometers. Restitic garnet has been shown to have relatively low partition coefficients of LREE and HFSE relative to extracted melt (Mysen, 1978; Johnson, 1998; Sun & Liang, 2013; Taylor et al., 2015). Yb and Y are compatible in garnet relative to La, Gd, and Sr, and this process is inferred to be the primary cause of the crustal thickness-dependence on La/Yb and Sr/Y in arc rocks (Chiaradia, 2015; Profeta et al., 2015; Farner & Lee, 2017).

Garnet is not alone in controlling these ratios. Clinopyroxene is ubiquitous in mantle lherzolite (ca. 5-20 vol %) and experimental studies have demonstrated it is typically a restitic phase in the generation of basaltic melts from low degrees of partial melting of mantle lherzolite starting material (Adam & Green, 1994; Johnson, 1998). The composition of restitic clinopyroxene affects mineral-liquid D_{REE}, as do melt f_{O_2} and P (Adam & Green, 1994; Sun & Liang, 2013; Michely et al., 2017). Pressure, [Ti], and [Al] can affect D_{La}, for example, by up to a factor of 7 (Sun & Liang, 2013). The specific source composition of mantle-derived juvenile melts is therefore an important factor controlling the La/Yb and Sr/Y ratios of arc- and collision-produced magmas.

There is additionally compositional heterogeneity of trace elements in the lithospheric mantle, which can be exacerbated by the degree of mantle metasomatism. Lithospheric mantle xenoliths have a median La/Yb of 2.85, but La concentrations range significantly, with a median of 0.77 ppm, mean of 2.60 ppm, and standard deviation of 5.70 ppm (McDonough, 1990). The La/Yb of the average values is 10.00; significantly higher than the median value. Sr/Y is

similarly variable, with a median of 6.45 and average of 11.14. Local or inter-arc heterogeneity of the source material is therefore a potential cause of uncertainty in both the calibrations and application of pseudobarometers to rocks of unknown crustal thickness.

3.3 Data analysis: do they work for case studies?

3.3.1 The problem of resampling in small datasets

The Central Limit Theorem is a concept of probability theory that describes the tendency of resampled values–from a dataset of independently random variables–to approach a normal distribution, regardless of the distribution of the original population. In the case of igneous rock samples, we can consider the global compositional distribution of Earth's igneous rocks as the "original" population. Sampling of these rocks is thus equivalent to a statistical resampling of a subset of these original data. As the number of resampled values (n) increases, the mean of samples S_n and its variance (σ^2) approaches the mean of the original population (μ), i.e.,

$$\lim_{n\to\infty} \sqrt{n}(S_n - \mu) = N(0, \sigma^2) \quad (5)$$

where N is a normal (gaussian) distribution with mean 0 and variance σ^2. That is, large-n resamples of the original population will generally be representative of the mean and standard deviation of the original population, even if the original distribution is not preserved.

In the case of pseudobarometers calibrated from large-n, global geochemical datasets, we can infer that the calibration is generally representative of μ and σ^2 of Earth as a whole. The application of pseudobarometers to discrete localities with values of n orders of magnitude lower than the n of the datasets used in the calibration, however, carries no such guarantee. The calibrations of the relationship between dm and Sr/Y and La/Yb use median values deliberately to avoid the influence of outliers (Profeta et al., 2015; Farner & Lee, 2017; Hu et al., 2017; Lieu & Stern, 2019). With small-n datasets, one cannot assume *a priori* that the sample distribution is

equivalent or representative of the bulk Earth distribution. To demonstrate the problem of small-*n* sample sets falling outside of the global distribution, I performed a Monte Carlo simulation with bootstrap resampling of La/Yb values from Farner & Lee's unfiltered dataset (n = 12506). Populations were randomly resampled over 10^5 iterations from the original data, with $n = 10^1$, 10^2, 10^3, and 10^4. Fig. 3.6 shows the results of this simulation: low-*n* resampled populations have a significantly broader distribution of sample mean (μ_n), sample standard deviation (σ_n), and the difference between the sample mean and the population mean (μ_n - μ_X). The probability

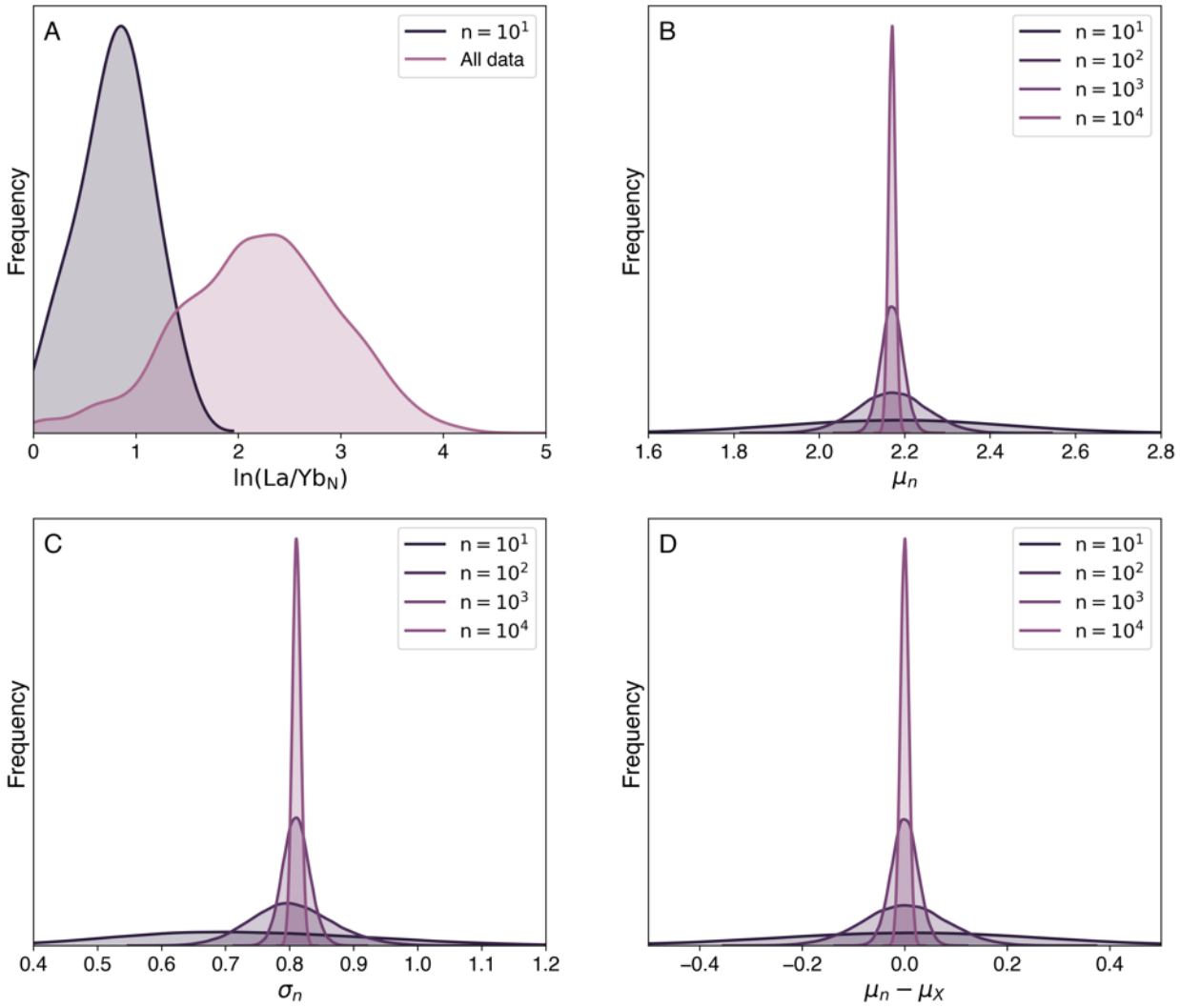

Figure 0.6: Kernel density estimation (KDE) functions of resampled data; all data in ln(La/Yb$_N$). (A) Values for all data compared to an example subset of data, n = 10. (B) Distribution of means of resampled data for 10^5 iterations of each n value. (C) Distribution of standard deviations of resampled data as in (B). (D) Distribution of difference between means of resampled values and mean of all data, μ_X, as in (B).

distribution function of an example instance of 10^1 resampled values is significantly different than the distribution of the original data (Fig. 3.1a). This simulation demonstrates the risk that small-*n* rock sample sets, taken from a single locality, will not yield data that are consistent with the global relationship between dm and La/Yb.

3.3.2 Probabilities of pseudobarometer model fits

The general probability of any given arc rock sample falling within pseudobarometer model calibrations can additionally be calculated using the dataset compiled by Farner & Lee (2017) and the Sr/Y and La/Yb_N models of Profeta et al (2015) and Farner & Lee (2017). As dm is well-constrained for these samples, a model value of Sr/Y and La/Yb_N can be calculated for each sample's value of dm, which is then compared to the sample's actual ratios. For the Sr/Y model of Profeta et al. (2015), only 9% of all young arc samples (filtered for composition, n = 3118) fall within 1σ of the model fit; only 18% of samples fall within 2σ. Their La/Yb_N model fares similarly, with 10% of filtered samples falling within 1σ and 15% falling within 2σ. For Farner & Lee (2017)'s La/Yb_N model, 22% of unfiltered samples (n = 12506) fall within 1σ, and 67% fall within 2σ. When the data are filtered for composition as in Profeta et al. (2015)'s model (n = 4012), 31% fall within 1σ and 62% within 2σ of Farner & Lee (2017)'s model. As their dataset used to fit the model was not filtered by composition, their model is more widely applic able to arc rocks of a wide range of compositions. Their efforts to correct for sampling bias by calibrating the model on the medians from areally-averaged elevation bins provided a more robust foundation for the calibration than averages of each arc. The total number of median values used for their calibration (67) is higher than the number of arcs averaged by Profeta et al. (2015), and the elevation bins allowed for possible heterogeneity in crustal thickness throughout

large arcs, expressed as differences in elevation of each 100 km^2 grid space.

Data from young collisional rock samples, with well-constrained dm, applied to the collisional models of Hu et al. (2017) fit the La/Yb_N model 40% (1σ) and 75%(2σ) of the time, and the Sr/Y model 47%(1σ) and 69%(2σ) of the time. The geologic factors affecting Sr/Y and La/Yb may be more limited in continental collision zones relative to the range of factors affecting both oceanic and continental arcs; it is also possible the model is overfit to the data due to relatively small *n* compared to the global arc databases. For Hu et al. (2017)'s models, *n* was one to two orders of magnitude smaller for Sr/Y ($n = 1277$) and La/Yb ($n = 829$) relative to the arc datasets ($n = 9800$, Profeta et al. (2015); $n = 12506$, Farner & Lee (2017)). As discussed in §3.3.1, small datasets represent a low-*n* resample of Earth's composition and may not be representative. When a model is calibrated from relatively low-*n*, it may therefore be propagating resampling bias. A pseudobarometer model that propagates resampling bias will further obfuscate results of

These problems multiply when additional uncertainties are introduced. While large sample sets ($n \geq 10^2$) of modern arc and collisional magmatic rocks may yield results that are reasonably consistent with the pseudobarometer models, there are unconstrained effects of geologic processes experienced by older samples–such as weathering, deuteric alteration, and regional metamorphism.

3.3.3 Compiled data from southern Tibetan igneous rocks

Magmatism in the Tibetan Plateau straddles a tectonic transition from a continental arc environment that produced the Gangdese Arc, to a collisional environment beginning at the onset of the India-Asia collision by ca. 57 Ma (Leech et al., 2005). Application of pseudobarometers to Tibetan granitoids must therefore take this tectonic transition into account by applying

appropriate models to pre- and syn-collisional samples. It follows that the La/Yb_N and Sr/Y models of Hu et al. (2017) should be applied to units <57 Ma, and that arc-based models be applied to older units. Given that Farner & Lee (2017)'s La/Yb_N model fits a wider range of natural data than the model of Profeta et al. (2015), the former model is used for the La/Yb_N model in pre-collisional samples. Profeta et al. (2015)'s model is used for Sr/Y model depths in

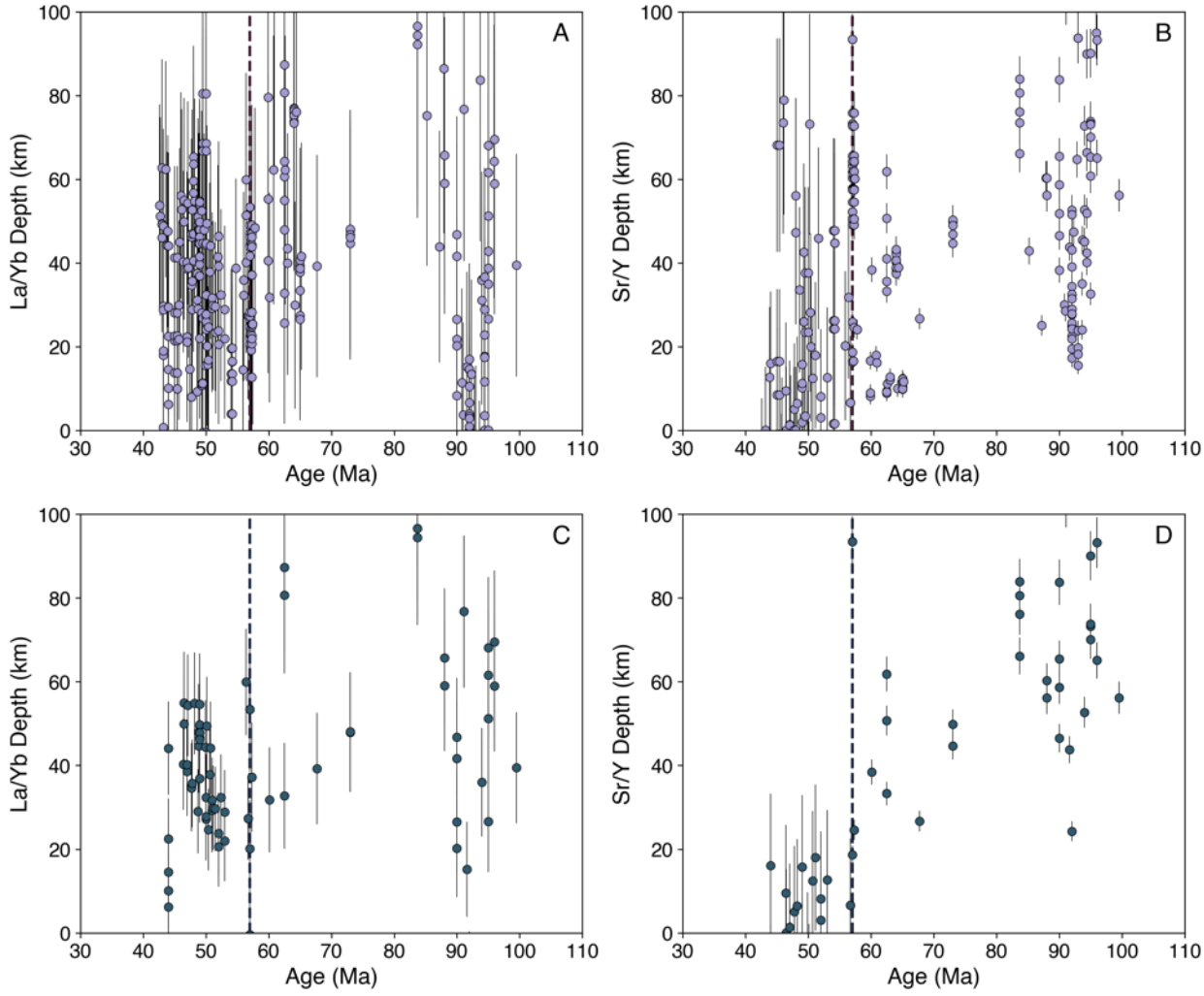

Figure 0.7: Pseudobarometer model Moho thickness of Tibetan magmatic rocks; arc models are used for >57 Ma samples, and collisional models for younger samples. Dashed lines are at 57 Ma; error bars are 1σ. (A) La/Yb_N models of Hu et al. (2017) (≤57 Ma) and Farner & Lee (2017) (>57 Ma), unfiltered for composition. (B) Sr/Y models of Hu et al. (2017) (≤57 Ma) and Profeta et al. (2015) (>57 Ma), unfiltered for composition. (C) La/Yb_N models as in (A), filtered for composition $55\% \leq SiO_2 \leq 68\%$; $MgO \leq 4\%$. (D) Sr/Y models as in (B), filtered for composition as in (C).

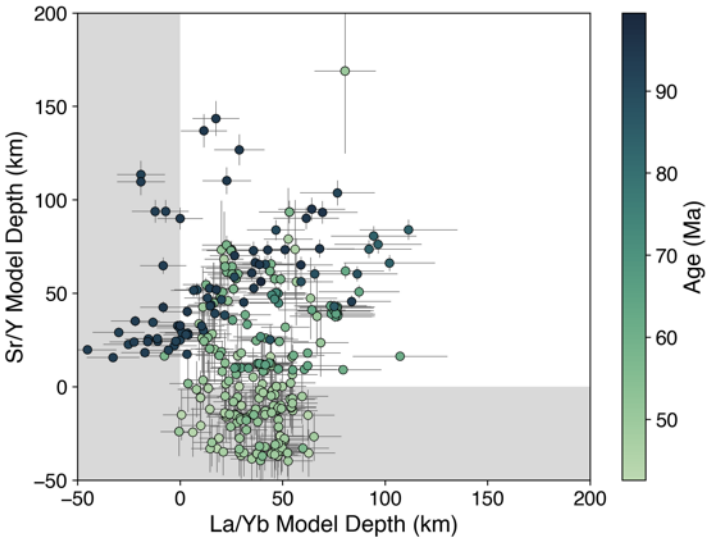

Figure 0.8 Comparison of La/Yb_N and Sr/Y models in samples from southern Tibet. Error bars 1σ; colormap is sample age. Gray areas are where Moho depth <0 km for either model.

pre-collisional samples.

Fig. 3.7 shows the results of these combined models for Tibetan magmatic rocks age 40 – 100 Ma, located between 85º – 95ºE and 29.2º – 30ºN. Not only do the model Moho depths show no clear crustal thickening pattern from the pre- to syn-collisional transition; they result in pathologically deep Moho depths even, and especially, for pre-collisional samples. When the data are filtered to only include rocks of intermediate composition, there is an apparent trend of *shallower* Moho depth in syn-collisional samples. There is no obvious benefit to filtering the data by major element composition, even for Profeta et al. (2015)'s model which is calibrated to intermediate compositions. A significant portion of the data are outside of geologically reasonable Moho depths, with many points at either negative Moho depths, or depths > 100 km, for one or both models (Fig. 3.8). There is additionally a change in the relationship between the two models from older to younger samples: older than ca. 80 Ma, Sr/Y model depths are ~50 km higher than La/Yb model depths, while the trend is generally reversed in samples < 60 Ma. There is some correlation with wt. % SiO_2 and $\Delta DM = DM_{La/Yb} - DM_{Sr/Y}$ (Fig. 3.4); more felsic

samples tend to have ΔDM > 0, while relatively more mafic samples have ΔDM < 0.

3.4 Discussion

Given that trace element pseudobarometers are predicated on pressure-dependent partitioning of the elements of interest during partial melting, both the Sr/Y and La/Yb_N models should agree. However, in the case example for Tibetan rocks, it is clear that these models not only do not agree, but yield geologically improbable or impossible model Moho depths. Even with < 57 Ma samples, for which both model depths are calculated using Hu et al. (2017)'s collisional models, there is some compositionally-related dispersion in ΔD that cannot be explained by differing model calibrations. It is likely that unconstrained processes following the generation of juvenile melt are differentially modifying Sr/Y and La/Yb in the resultant magmas (Fig. 3.9).

As discussed in Chapter 2, southern Lhasa terrane granitoids show ample evidence of crustal assimilation. If we assume that whole-rock stable isotopes are a proxy for assimilation between juvenile mantle and old crust-derived endmembers, as in Ch.2, it is clear that crustal assimilation contributes to the degree of magmatic differentiation/evolution toward more felsic compositions. This same process is tracked in ΔDM, with more felsic, assimilated samples

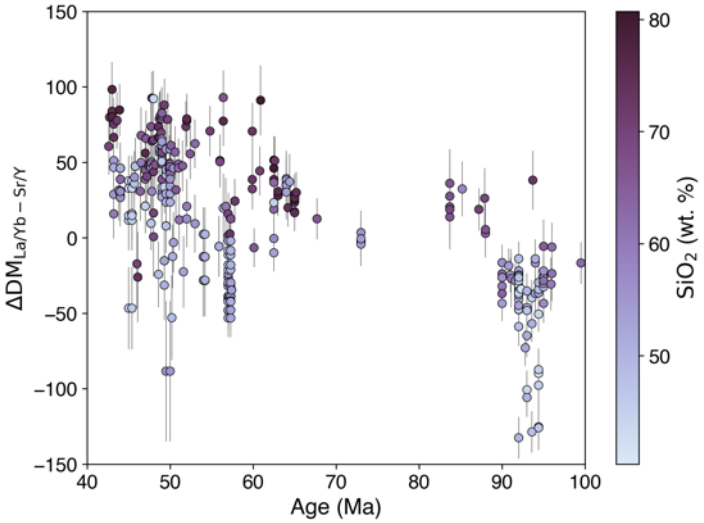

Figure 0.9: Difference between La/Yb_N model and Sr/Y model Moho depth (km) with age, color-coded by wt. % SiO_2.

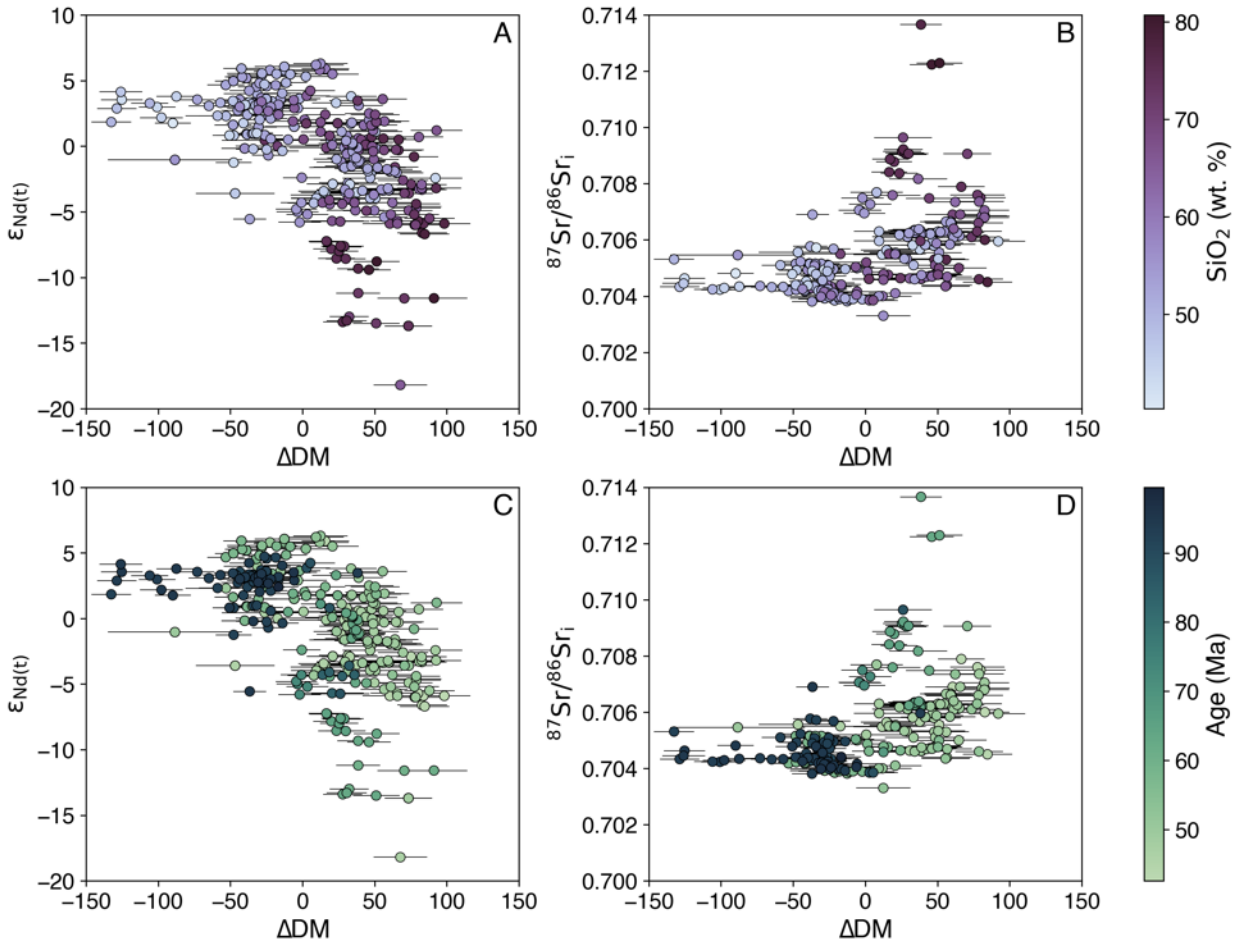

Figure 0.10: Difference between La/Yb_N and Sr/Y model depths (ΔDM) with whole-rock isotopes; error bars are 1σ. (A) $\varepsilon_{Nd(t)}$ and ΔDM, color-coded by sample wt. % SiO_2. (B) $^{87}Sr/^{86}Sr_i$ and ΔDM, colors as in (A). (C) $\varepsilon_{Nd(t)}$ and ΔDM, color-coded by sample age. (D) $^{87}Sr/^{86}Sr_i$ and ΔDM, colors as in (C).

enriched in radiogenic isotopes ($\varepsilon_{Nd(t)}$ and $^{87}Sr/^{86}Sr_i$), and a general trend toward higher degrees of crustal assimilation in younger samples (Fig. 3.10). It is geochemically consistent for ΔDM to become more positive with more radiogenic values of $\varepsilon_{Nd(t)}$, as Nd and La are both light rare-earth elements who are likely to behave similarly during the aforementioned processes. Whole-rock modification of $^{87}Sr/^{86}Sr_i$ from the juvenile endmember similarly implies exchange of Sr during crustal assimilation; increasing ΔDM with $^{87}Sr/^{86}Sr_i$ suggests that assimilation may be reducing the overall concentration of Sr relative to Y in the magma. The trace element ratios used in pseudobarometers must therefore be significantly modified by the degree of magmatic

differentiation and assimilation.

The datum with maximum $\varepsilon_{Nd(t)}$, +6.3, also has unradiogenic $^{87}Sr/^{86}Sr_i$ (0.7033), but has ΔDM = 12.5 km. The data with the most negative ΔDM have slightly more radiogenic isotopic values, and are also not necessarily the most mafic, so there are likely other controlling factors beyond degree of crustal assimilation. Most of the data with the most negative ΔDM are relatively older, so secondary alteration may additionally be playing a role differential exchange of La/Yb vs. Sr/Y. Differential weathering rates of Sr- and Y-bearing minerals, for example, may exacerbate changes in whole-rock Sr/Y ratio following emplacement. For example, though plagioclase has a significantly higher D_{Sr}/D_Y than biotite (Fedele et al., 2015), it was shown that biotite in glaciated Sierra Nevada granites weathered 4-6 times faster than plagioclase (Blum et al., 1993). Depending on the relative abundances and weathering rates of plagioclase and biotite in Tibetan magmatic rocks, exposure to weathering processes for many 10's of Ma in older samples may differentially deplete Y relative to Sr, leading to deeper apparent $DM_{Sr/Y}$ in those samples. The highly negative ΔDM values in old samples likewise imply a depletion of La relative to Yb relative to Sr/Y. Accessory minerals including apatite, allanite, and sphene are significant contributors to the whole-rock budget of LREE, and are generally quite soluble during hydrothermal alteration in acidic fluids (Exley, 1980; Guidry & Mackenzie, 2003). Dissolution of LREE-rich phases during weathering would deplete the whole-rock budget of La relative to Yb, leading to pathologically low $DM_{La/Yb}$, as seen in many older, unradiogenic samples with negative ΔDM.

During crustal assimilation, partitioning of La, Yb, Sr, and Y into the melt are dependent on composition, as they are governed by the saturation and partition coefficients of the minerals controlling the whole-rock budget of these elements. Dissolution of LREE-bearing phases out of

the country rock and into the melt is limited by the melt composition; more mafic melts will dissolve a greater fraction of apatite, for example, than felsic melts (Watson & Harrison, 1984); the melt water content will also impact apatite dissolution (Harrison & Watson, 1984). Positive ΔDM implies differential enrichment of La/Yb relative to Sr/Y, and correlates with crustal assimilation indicators in Tibetan rock data (Fig. 3.10). It is therefore likely that crustal assimilation modifies juvenile melt La/Yb more readily than Sr/Y, and this effect becomes more dramatic with highly felsic melts.

3.5 Conclusions

Trace element pseudobarometers using the ratios of La/Yb and Sr/Y are subject to a number of confounding factors that impact their reliability for reconstructing crustal thicknesses in ancient and evolving terranes. The existing calibrations do not consistently reproduce the crustal thicknesses of young arcs and collision zones whose Moho depth is well-constrained by seismic and elevation proxies. Sampling bias in small-*n* datasets has the potential to generate spurious results leading to incorrect assumptions regarding the crustal thickness of ancient terranes. Processes including crustal assimilation, magmatic differentiation, and secondary alteration appear to modify these pseudobarometers, causing significant disagreement between models.

This has implications not only for the use of pseudobarometers for reconstructing crustal thickness in southern Tibet, but also for their use more broadly. There appear to be significant unconstrained factors that affect these trace element ratios outside of the scope of the model calibrations, and it is not yet clear to what extent these factors operate on the geochemistry of discrete magmatic terranes. In the case of southern Tibet, it is likely that a combination of a complex, evolving tectonic setting, crustal assimilation, degree of differentiation, deuteric

alteration, and weathering coalesced to produce spurious results in pseudobarometer models. This study indicates that trace element pseudobarometers are not suitable for reconstructing ancient crustal thicknesses, even for relatively large datasets.

3.6 References

Adam, J., & Green, T. H. (1994). The effects of pressure and temperature on the partitioning of Ti, Sr and REE between amphibole, clinopyroxene and basanitic melts. *Chemical Geology*, *117*(1), 219–233. https://doi.org/10.1016/0009-2541(94)90129-5

Babeyko, A. Y., Sobolev, S. V., Trumbull, R. B., Oncken, O., & Lavier, L. L. (2002). Numerical models of crustal scale convection and partial melting beneath the Altiplano–Puna plateau. *Earth and Planetary Science Letters*, *199*(3), 373–388. https://doi.org/10.1016/S0012-821X(02)00597-6

Blum, J. D., Erel, Y., & Brown, K. (1993). 87Sr/86Sr ratios of sierra nevada stream waters: Implications for relative mineral weathering rates. *Geochimica et Cosmochimica Acta*, *57*(21), 5019–5025. https://doi.org/10.1016/S0016-7037(05)80014-6

Chapman, J. B., Ducea, M. N., DeCelles, P. G., & Profeta, L. (2015). Tracking changes in crustal thickness during orogenic evolution with Sr/Y: An example from the North American Cordillera. *Geology*, *43*(10), 919–922. https://doi.org/10.1130/G36996.1

Chiaradia, M. (2015). Crustal thickness control on Sr/Y signatures of recent arc magmas: an Earth scale perspective. *Scientific Reports*, *5*, 8115. https://doi.org/10.1038/srep08115

Connolly, J. A. D. (1990). Multivariable phase diagrams; an algorithm based on generalized thermodynamics. *American Journal of Science*, *290*(6), 666–718.

https://doi.org/10.2475/ajs.290.6.666

Connolly, J. A. D. (2005). Computation of phase equilibria by linear programming: A tool for geodynamic modeling and its application to subduction zone decarbonation. *Earth and Planetary Science Letters*, *236*(1), 524–541. https://doi.org/10.1016/j.epsl.2005.04.033

Dale, J., Holland, T., & Powell, R. (2000). Hornblende–garnet–plagioclase thermobarometry: a natural assemblage calibration of the thermodynamics of hornblende. *Contributions to Mineralogy and Petrology*, *140*(3), 353–362. https://doi.org/10.1007/s004100000187

Dimalanta, C., Taira, A., Yumul, G. P., Tokuyama, H., & Mochizuki, K. (2002). New rates of western Pacific island arc magmatism from seismic and gravity data. *Earth and Planetary Science Letters*, *202*(1), 105–115. https://doi.org/10.1016/S0012-821X(02)00761-6

Eberhart-Phillips, D., Christensen, D. H., Brocher, T. M., Hansen, R., Ruppert, N. A., Haeussler, P. J., & Abers, G. A. (2006). Imaging the transition from Aleutian subduction to Yakutat collision in central Alaska, with local earthquakes and active source data. *Journal of Geophysical Research: Solid Earth*, *111*(B11). https://doi.org/10.1029/2005JB004240

Exley, R. A. (1980). Microprobe studies of REE-rich accessory minerals: Implications for Skye granite petrogenesis and REE mobility in hydrothermal systems. *Earth and Planetary Science Letters*, *48*(1), 97–110. https://doi.org/10.1016/0012-821X(80)90173-9

Farner, M. J., & Lee, C.-T. A. (2017). Effects of crustal thickness on magmatic differentiation in subduction zone volcanism: A global study. *Earth and Planetary Science Letters*, *470*, 96–107. https://doi.org/10.1016/j.epsl.2017.04.025

Fedele, L., Lustrino, M., Melluso, L., Morra, V., Zanetti, A., & Vannucci, R. (2015). Trace-

element partitioning between plagioclase, alkali feldspar, Ti-magnetite, biotite, apatite, and evolved potassic liquids from Campi Flegrei (Southern Italy). *American Mineralogist*, *100*(1), 233–249. https://doi.org/10.2138/am-2015-4995

Green, D. H., & Ringwood, A. E. (1967). The stability fields of aluminous pyroxene peridotite and garnet peridotite and their relevance in upper mantle structure. *Earth and Planetary Science Letters*, *3*, 151–160. https://doi.org/10.1016/0012-821X(67)90027-1

Guidry, M. W., & Mackenzie, F. T. (2003). Experimental study of igneous and sedimentary apatite dissolution: Control of pH, distance from equilibrium, and temperature on dissolution rates. *Geochimica et Cosmochimica Acta*, *67*(16), 2949–2963. https://doi.org/10.1016/S0016-7037(03)00265-5

Harrison, T. M., & Watson, E. B. (1984). The behavior of apatite during crustal anatexis: Equilibrium and kinetic considerations. *Geochimica et Cosmochimica Acta*, *48*(7), 1467–1477. https://doi.org/10.1016/0016-7037(84)90403-4

Hensen, B. J., & Green, D. H. (1971). Experimental study of the stability of cordierite and garnet in pelitic compositions at high pressures and temperatures. *Contributions to Mineralogy and Petrology*, *33*(4), 309–330. https://doi.org/10.1007/BF00382571

Hu, F., Ducea, M. N., Liu, S., & Chapman, J. B. (2017). Quantifying Crustal Thickness in Continental Collisional Belts: Global Perspective and a Geologic Application. *Scientific Reports*, *7*(1), 1–10. https://doi.org/10.1038/s41598-017-07849-7

Johnson, K. T. M. (1998). Experimental determination of partition coefficients for rare earth and high-field-strength elements between clinopyroxene, garnet, and basaltic melt at high pressures. *Contributions to Mineralogy and Petrology*, *133*(1), 60–68.

https://doi.org/10.1007/s004100050437

Kay, S. M., Coira, B. L., Caffe, P. J., & Chen, C.-H. (2010). Regional chemical diversity, crustal and mantle sources and evolution of central Andean Puna plateau ignimbrites. *Journal of Volcanology and Geothermal Research*, *198*(1), 81–111. https://doi.org/10.1016/j.jvolgeores.2010.08.013

Laske, G., Masters, G., Ma, Z., & Pasyanos, M. (2013). Update on CRUST1.0 - A 1-degree Global Model of Earth's Crust. *Geophysical Research Abstracts*, *15*(EGU2013-2658), 1.

Leech, M. L., Singh, S., Jain, A. K., Klemperer, S. L., & Manickavasagam, R. M. (2005). The onset of India–Asia continental collision: Early, steep subduction required by the timing of UHP metamorphism in the western Himalaya. *Earth and Planetary Science Letters*, *234*(1), 83–97. https://doi.org/10.1016/j.epsl.2005.02.038

Lieu, W. K., & Stern, R. J. (2019). The robustness of Sr/Y and La/Yb as proxies for crust thickness in modern arcs. *Geosphere*, *15*(3), 621–641. https://doi.org/10.1130/GES01667.1

Lücke, O. H. (2014). Moho structure of Central America based on three-dimensional lithospheric density modelling of satellite-derived gravity data. *International Journal of Earth Sciences*, *103*(7), 1733–1745. https://doi.org/10.1007/s00531-012-0787-y

McDonough, W. F. (1990). Constraints on the composition of the continental lithospheric mantle. *Earth and Planetary Science Letters*, *101*(1), 1–18. https://doi.org/10.1016/0012-821X(90)90119-I

Mercier, J.-C. C. (1980). Single-pyroxene thermobarometry. *Tectonophysics*, *70*(1), 1–37.

https://doi.org/10.1016/0040-1951(80)90019-0

Michely, L. T., Leitzke, F. P., Speelmanns, I. M., & Fonseca, R. O. C. (2017). Competing effects of crystal chemistry and silicate melt composition on trace element behavior in magmatic systems; insights from crystal/silicate melt partitioning of the REE, HFSE, Sn, In, Ga, Ba, Pt and Rh. *Contributions to Mineralogy and Petrology*, *172*(6), Article 39. http://dx.doi.org/10.1007/s00410-017-1353-1

Mysen, B. O. (1978). Experimental determination of rare earth element partitioning between hydrous silicate melt, amphibole and garnet peridotite minerals at upper mantle pressures and temperatures. *Geochimica et Cosmochimica Acta*, *42*(8), 1253–1263. https://doi.org/10.1016/0016-7037(78)90119-9

Ouimet, W. B., & Cook, K. L. (2010). Building the central Andes through axial lower crustal flow. *Tectonics*, *29*(3). https://doi.org/10.1029/2009TC002460

Powell, R., & Holland, T. J. B. (1988). An internally consistent dataset with uncertainties and correlations: 3. Applications to geobarometry, worked examples and a computer program. *Journal of Metamorphic Geology*, *6*(2), 173–204. https://doi.org/10.1111/j.1525-1314.1988.tb00415.x

Powell, R., & Holland, T. J. B. (2008). On thermobarometry. *Journal of Metamorphic Geology*, *26*(2), 155–179. https://doi.org/10.1111/j.1525-1314.2007.00756.x

Profeta, L., Ducea, M. N., Chapman, J. B., Paterson, S. R., Gonzales, S. M. H., Kirsch, M., et al. (2015). Quantifying crustal thickness over time in magmatic arcs. *Scientific Reports*, *5*, 17786. https://doi.org/10.1038/srep17786

Putirka, K., Johnson, M., Kinzler, R., Longhi, J., & Walker, D. (1996). Thermobarometry of

mafic igneous rocks based on clinopyroxene-liquid equilibria, 0–30 kbar. *Contributions to Mineralogy and Petrology*, *123*(1), 92–108. https://doi.org/10.1007/s004100050145

Sarbas, B., Kalbskopf, B., Nohl, U., & Busch, U. (2019, September 1). Geochemistry of Rocks of the Oceans and Continents. Max Planck Institute for Chemistry. Retrieved from http://georoc.mpch-mainz.gwdg.de/georoc/

Sun, C., & Liang, Y. (2013). The importance of crystal chemistry on REE partitioning between mantle minerals (garnet, clinopyroxene, orthopyroxene, and olivine) and basaltic melts. *Chemical Geology*, *358*, 23–36. https://doi.org/10.1016/j.chemgeo.2013.08.045

Taylor, R. J. M., Harley, S. L., Hinton, R. W., Elphick, S., Clark, C., & Kelly, N. M. (2015). Experimental determination of REE partition coefficients between zircon, garnet and melt: a key to understanding high-T crustal processes. *Journal of Metamorphic Geology*, *33*(3), 231–248. https://doi.org/10.1111/jmg.12118

Thomas, J. B., Bruce Watson, E., Spear, F. S., Shemella, P. T., Nayak, S. K., & Lanzirotti, A. (2010). TitaniQ under pressure: the effect of pressure and temperature on the solubility of Ti in quartz. *Contributions to Mineralogy and Petrology*, *160*(5), 743–759. https://doi.org/10.1007/s00410-010-0505-3

Watson, E. B., & Harrison, T. M. (1984). Accessory minerals and the geochemical evolution of crustal magmatic systems: a summary and prospectus of experimental approaches. *Physics of the Earth and Planetary Interiors*, *35*(1), 19–30. https://doi.org/10.1016/0031-9201(84)90031-1

Watson, E. B., & Harrison, T. M. (2005). Zircon Thermometer Reveals Minimum Melting Conditions on Earliest Earth. *Science*, *308*(5723), 841–844.

https://doi.org/10.1126/science.1110873

Yuan, X., Asch, G., Bataille, K., Bock, G., Bohm, M., Echtler, H., et al. (2006). Deep seismic images of the Southern Andes. In *Evolution of an Andean Margin: A Tectonic and Magmatic View from the Andes to the Neuquén Basin (35 Degrees-39 Degrees S Lat)* (pp. 61–72). Geological Society of America. Retrieved from https://books.google.com/books?hl=en&lr=&id=SnpmcLcnh04C&oi=fnd&pg=PA61&ots=-eaEbsMnUp&sig=S5K7EOXl-qNJ9kFcLEoNp35FqLc#v=onepage&q&f=false

Zellmer, G. F. (2008). Some first-order observations on magma transfer from mantle wedge to upper crust at volcanic arcs. *Geological Society, London, Special Publications*, *304*(1), 15–31. https://doi.org/10.1144/SP304.2

– Chapter 4 –

Titanium thermobarometry of quartz and zircon

4.1 Introduction

4.1.1 Granitoid Thermobarometry

Interpreting of the role of magmatic systems in the evolution of Earth's crust requires a foundational understanding of the conditions at which magmas are generated, hybridized, and emplaced. The fundamental motivation of the inverse problem of igneous petrogenesis is that we are unable to directly observe the formation mechanisms of natural magmas. We are therefore left to the *ex-post-facto* interpretation of petrogenetic conditions using geochemistry, geochronology, and petrography. Understanding the petrogenesis of magmas from their resultant rocks provides substantial insight into geologic processes driving the geochemical and structural evolution of a region of interest. One of the most significant factors influencing the rheology and composition of the crust is its thickness, which influences the thermal profile and pressure conditions experienced by its constituent rocks (Babeyko et al., 2002; Burov & Yamato, 2008; Schott & Schmeling, 1998). Thickness-dependent crustal rheology carries implications for available deformation mechanisms and the conditions at which melts can form and migrate (De Yoreo et al., 1989; Brown, 1994; de Silva & Gregg, 2014).

Reconstructing the spatiotemporal evolution of crustal thickness throughout dynamic geologic processes requires investigation of rock formation pressures through time. While indirect geochemical proxies for estimating crustal thickness have been proposed and evaluated (Chapman et al., 2015; Profeta et al., 2015; Farner & Lee, 2017; Hu et al., 2017; DePaolo et al., 2019; Lieu & Stern, 2019), there are a number of confounding factors that can negatively influence the reliability of these methods (see Ch. 3). Directly reconstructing the pressure at which rocks and their constituent minerals form is therefore a more robust method of constraining crustal thickness. Thermobarometry provides such a tool, relying on experimental

and empirical calibrations of deviations in phase relations and chemistries due to variations in *P* and *T*. Thermobarometric evidence of these conditions can then be used to better understand a variety of geologic processes, including depth of magma emplacement, melt storage, and metamorphism. Relevant to this study is the utility of thermobarometry to estimate the minimum crustal thickness during generation of silicic plutons, which in turn can constrain deformation mechanisms available during the tectonic evolution of continental orogens.

The first-order assumption necessary for igneous thermobarometry is that the mineral of interest was in thermodynamic equilibrium with the melt as it crystallized. At magmatic temperatures, this is generally true, as cation diffusivities in the liquid phase are sufficiently fast to equilibrate with crystallizing phases (Hofmann & Magaritz, 1977; Lowry et al., 1982; Mungall et al., 1999). Thermobarometry requires solution for two intensive variables, *P* and *T*, and therefore requires at least two phases whose *P*- and *T*-dependent chemistry has been quantified. *A priori* assumption that multiple phases of interest were in thermodynamic equilibrium is problematic; the crystallization sequence of a cooling magma necessarily precludes uniform *T* and chemical activities experienced by phases which may have saturated at discrete intervals. Continuous crystallization during melt migration and emplacement is a further complication. Selection of the two (or more) phases to pair when solving for *P* and *T* must include a likelihood of cotectic crystallization intervals, such that it can be reasonably assumed the phases of interest experienced similar, if not identical, thermodynamic conditions during crystallization. It is additionally ideal to select phases with few components, such that variation in thermodynamic parameters due to solid solutions or variable site occupancy is minimized. Naturally occurring phases with fewer components are simpler to simulate in experimental settings, reducing the uncertainty induced by discrepancies between highly variable natural compositions and their

experimental endmembers. Finally, near thermodynamically ideal behavior during *P*- and/or *T*-dependent substitution of a given species reduces uncertainty associated with variations in chemical potential. An ideal thermobarometer has $a_i \approx X_i$, where *i* is the substituting species of interest, such that analytical results of concentration are sufficient to solve for *P* and *T*.

Mineral geothermometers (which are pressure-insensitive) are routinely used in both plutonic and volcanic systems (e.g. Ti-in-zircon, Zr-in-rutile, pyroxene-liquid, and two-feldspar thermometers (Anderson, 1996; Putirka et al., 1996; Watson & Harrison, 2005; Ferry & Watson, 2007)). Thermobarometers, sensitive to both pressure and temperature, are commonly used in metamorphic petrology, but experimentally calibrated igneous thermobarometers are scarce, and less routinely applied. The Al-in-hornblende barometer (Hammarstrom & Zen, 1986; Schmidt, 1992; Anderson & Smith, 1995; Mutch et al., 2016) has been a relatively popular barometer for granitic systems and displays reasonably linear increase in total Al concentration with increasing pressure in experimental studies (Mutch et al., 2016, and references therein). However, the Al content of unaltered magmatic hornblende is likely reflective of emplacement pressure, as case studies demonstrate agreement between thermochronometric evidence of post-emplacement storage temperature and the expected ambient geotherm at the pressures indicated by Al-in-hornblende (e.g., Tremblay et al., 2015; Alexander et al., 2016). This thermobarometer is therefore useful mainly for reconstructing the final emplacement depth of granitoid plutons, provided the hornblendes are unaltered. Hydrothermal alteration is, however, exceedingly common in granitoids, as evidenced by commonly observed textural features including sericitization and myrmekitization of feldspars, and chloritization of biotite and hornblende (Bray, 1969; Ferry, 1979; Leake, 1998; Nishimoto & Yoshida, 2010), and granitoids in southern Tibet are no exception (e.g., Blattner et al., 2002; Kapp et al., 2005). Fluid-mediated

recrystallization and cation exchange will reduce the Al content of magmatic hornblende, leading to spuriously low calculated pressures (Agemar et al., 1999; Alexander et al., 2016). Moreover, pluton emplacement depths are minimally reflective of actual crustal thickness, given that magma bodies can migrate 10's of km over the course of melt generation, hybridization, and emplacement (De Yoreo et al., 1989; Brown, 1994). A thermobarometer that plumbs greater depths of petrogenetic processes is therefore required to approach a minimum estimate of crustal thickness, disqualifying the use of Al-in-hornblende barometry for this study.

The Ti-in-zircon thermometer (T_{zir}) is generally useful for all but the most mafic compositions of igneous rocks and has been extensively tested and calibrated (Watson & Harrison, 2005; Ferry & Watson, 2007; Harrison et al., 2007; c.f. Hofmann et al., 2009). Zircon's near-ubiquitous presence as an accessory mineral in intermediate to felsic igneous rocks, paired with its incompressibility at crustal pressures, makes T_{zir} an ideal thermometer for most igneous rocks. T_{zir} can therefore be used to constrain T in order to solve for P using a coexisting mineral thermobarometer. The Ti-in-quartz thermobarometer (P_{qtz}) (Thomas et al., 2010, 2015) is, for our purposes, an ideal barometric counterpart. The T- and P-dependent substitution of Ti into the quartz lattice is sensitive to both pressure and temperature, so pressure can therefore be constrained with temperature independently constrained using T_{zir}. An additional advantage to pairing these two systems is their mutual dependence on the activities of rutile and quartz. The presence of quartz necessarily dictates that a_{SiO_2} is unity, so a_{TiO_2} governs the availability of Ti to substitute into the quartz and zircon lattices.

Ensuring equilibrium between quartz and zircon poses an additional challenge to accurate calculation of P_{qtz}. While quartz and zircon generally crystallize over similar intervals in felsic magmas (Miller et al., 2003; Claiborne et al., 2010; Boehnke et al., 2013), localized

compositional differences in a highly viscous, cooling granitic melt could induce variance in a_{TiO_2}; protracted crystallization throughout melt generation, migration, and emplacement can induce zoning in [Ti] in both zircon and quartz (Harrison & Schmitt, 2007; Schoene et al., 2012; Thomas et al., 2015). Analysis of separate whole quartz and zircon grains therefore is not guaranteed to represent equilibrium partitioning of Ti between these two phases. In this study, I present both whole-grain analyses as well as a thorough investigation of T_{zir} and P_{qtz} of quartz inclusions in zircon. Primary, unaltered quartz inclusions are in equilibrium with their zircon hosts by nature of their proximity and the reasonably high diffusivity of Ti in the surrounding melt at magmatic temperatures (Mungall et al., 1999). While analysis of 5–30 µm quartz inclusions in zircon requires significantly higher spatial resolution than analysis of separate whole grains, the greater likelihood of thermodynamic equilibrium (i.e., identical a_{TiO_2} during crystallization) justifies this effort.

4.1.2 Thermodynamic Basis of T_{zir} and P_{qtz}

The T_{zir} calibration of Ferry and Watson (2007) assumes X_{Ti}^{zircon} behaves according to Henry's law, as [Ti] in zircon is typically limited to between 10^0 to 10^2 ppm Ti. First-principles calculations indicate the incorporation of Ti into the zircon lattice occurs through substitution of Ti into the Si site (Harrison et al., 2005; Ferriss et al., 2008):

$$ZrSiO_4 + TiO_2 = ZrTiO_4 + SiO_2 \quad (6)$$

The Ferry and Watson (2007) calibration allows for estimation of zircon crystallization temperature in rutile-undersaturated rocks by incorporating a term for a_{TiO_2}, as well as silica-

undersaturation with a_{SiO_2}. Assuming equilibrium,

$$\Delta H^0 - T\Delta S^0 + P\Delta V^0 + RT\ln a_{ZrTiO_4} + RT\ln a_{SiO_2} - RT\ln a_{ZrSiO_4} - RT\ln a_{TiO_2} = 0 \quad (7)$$

Where ΔH^0, ΔS^0, and ΔV^0 are the change in enthalpy, entropy, and volume of the reaction at standard state, R is the gas constant 8.314x10^{-3}, and T is the temperature of reaction. The activity of $ZrTiO_4$, $a_{ZrTiO_4} = k_1$, where

$$k_1 = \gamma * X_{ZrTiO_4}^{zircon} * f \quad (8)$$

γ is the Henry's Law coefficient, and f is the factor converting $X_{ZrTiO_4}^{zircon}$ to ppm Ti-in-zircon. Accordingly, equation (2) may be rearranged:

$$\log[\mathrm{Ti}]_{\mathrm{zircon}}\,(\mathrm{ppm}) = \log \mathrm{a}_{\mathrm{TiO_2}} - \log \mathrm{a}_{\mathrm{SiO_2}} + \left(\frac{\Delta \bar{\mathrm{S}}^0}{2.303\mathrm{R}} - \log k_1\right) - \frac{\Delta \bar{\mathrm{H}}^0 + \mathrm{P}\Delta \bar{\mathrm{V}}^0}{2.303\mathrm{RT}} \quad (9)$$

The experimental calibration of Ferry and Watson (2007) finds that $\Delta\bar{S}^0/2.303R - \log k_1 =$ 5.711±0.072, and $(\Delta\bar{H}^0 + P\Delta\bar{V}^0)/2.303R =$ – 4800±86 using standard state values for α-quartz and rutile at the relevant P and T. For felsic rocks with abundant quartz, as is the case in this study, it may be reasonably assumed that $a_{SiO_2} = 1$, such that $\log a_{SiO_2} = 0$. The equation thus reduces to:

$$\log[Ti]_{zircon}\,(ppm) = \log a_{TiO_2} + (5.711 \pm 0.072) + (4800 \pm 86)/T(\mathrm{K}) \quad (10)$$

which when solved for T becomes:

$$T_{zir}(\mathrm{K}) = \frac{-4800 \pm 86}{\log[Ti]_{zircon}(ppm) - \log a_{TiO_2} - (5.711 \pm 0.072)} \quad (11)$$

When temperature is constrained with T_{zir}, the P- and T-dependent substitution of Ti into

the quartz lattice may be leveraged to calculate the pressure of quartz crystallization. Substitution of Ti into the quartz lattice occurs at trace levels (10^1 – 10^2 ppm Ti) in magmatic quartz, and its *P*- and *T*-dependence was experimentally calibrated by Wark & Watson (2006) and Thomas et al. (2010, 2015) following the exchange reaction between rutile and a quartz-isostructural, fictive TiO_2 phase:

$$TiO_2^{\text{rutile}} \leftrightarrow TiO_2^{quartz} \tag{12}$$

where $a_{TiO_2}^{quartz} = k_2 X_{TiO_2}^{quartz}$; k_2 is the Henry's law coefficient, i.e. $a_{TiO_2}^{quartz} \approx X_{TiO_2}^{quartz}$. At equilibrium,

$$\Delta\bar{G}^0 = \Delta\bar{H}^0 - T(\Delta\bar{S}^0 - R\ln k_{TiO_2}) + P\Delta\bar{V}^0 + RT\ln X_{TiO_2}^{quartz} - RT\ln a_{TiO_2} = 0 \tag{13}$$

which may be rearranged as,

$$RT\ln X_{TiO_2}^{quartz} = -\Delta\bar{H}^0 + T\Delta\bar{S}^0 - P\Delta\bar{V}^0 + RT\ln a_{TiO_2} - RT\ln k_2 \tag{14}$$

Thomas et al. (2010, 2015) experimentally calibrated the above equation over a *P* range of 5 – 20 kbar and a *T* range of 600ºC – 1000ºC:

$$RT\ln X_{TiO_2}^{quartz} = -a + b * T - \mathrm{c} * P(kbar) + RT\ln a_{TiO_2} \tag{15}$$

where a = 60952±3122, b = 1.520±0.04, and c = 1741±63; representing the calibrated values for

$\Delta\bar{H}^0, \Delta\bar{S}^0,$ and $\Delta\bar{V}^0$, respectively. Rearranging for *P* gives:

$$P_{qtz}(kbar) = \frac{-a+b*T+RT\left(\ln a_{TiO_2} - \ln X_{TiO_2}^{quartz}\right)}{c} \quad (16)$$

where $T = T_{zir}$ in degrees K.

Constraining a_{TiO_2} in rutile-absent rocks remains problematic and must be addressed so as to avoid significant under- or over-estimation of T_{zir} and P_{qtz}. When T_{zir} and P_{qtz} are paired, the problem is somewhat self-correcting due to the presence of the a_{TiO_2} term in both the numerator and denominator. Unconstrained a_{TiO_2} can still result in an overestimation of P_{qtz} by up to ca. 2.5 kbar, so effort must be made to narrow the range of likely a_{TiO_2}. Various methods have been proposed, including calculation from whole-rock [Ti] (Hayden & Watson, 2007; Ryerson & Watson, 1987) as well as from coexisting Fe-Ti oxides (Ghiorso & Gualda, 2013). The whole-rock methods significantly overestimate rutile saturation in granitoids, likely due to sequestration of available Ti in other modal phases (e.g. ilmenite, titanite, hornblende, and biotite) such that bulk [Ti] is not representative of a_{TiO_2} of the melt during crystallization of zircon and quartz. Analysis of paired Fe-Ti oxides, likewise, presumes these oxides are in equilibrium with the residual melt at the time of zircon crystallization, but the low diffusivity of Ti in crystalline phases suggests this is likely not the case (Cherniak et al., 1997, 2007). The range of a_{TiO_2} typical of rutile-undersaturated metamorphic rocks with titanite present was calculated, based on phase relations to $a_{TiO_2} = 0.75 \pm 0.26$ (P. Kapp et al., 2009); a_{TiO_2} of late-stage melts in felsic magmatic rocks is typically somewhat lower (Ghiorso & Gualda, 2013). The necessary precision of a_{TiO_2} constraint required to apply Ti-thermobarometry is dependent on the level of precision needed in the resultant temperature and pressure calculations. For the purpose of this study, where I examine broad trends in crustal thickness spanning many kbar, it is permissible to

propagate relatively generous uncertainty in a_{TiO_2}, within the expected bounds for typical felsic igneous rocks. Accordingly, I use $a_{TiO_2} = 0.6 \pm 0.15$ (1σ) to account for the probable range present in rutile-undersaturated granitoids with abundant ilmenite and titanite.

The effects of secondary alteration on inclusion-host pairs can be explored by measuring $\Delta^{18}O$ of quartz inclusions and their zircon hosts. However, it is an imperfect proxy for the retention of primary [Ti] partitioning between quartz and zircon. Self-diffusion of O in both quartz and zircon is significantly faster than Ti (Cherniak et al., 1997, 2007; Watson & Cherniak, 1997). Moreover, Ti is quite insoluble in hydrothermal fluids at mid- to upper-crustal pressures, even at magmatic temperatures (Antignano & Manning, 2008; Thomas et al., 2019), so though $\delta^{18}O_{qtz}$ may be greatly modified relative to $\delta^{18}O_{zir}$ during hydrothermal alteration (King et al., 1997), primary magmatic Ti partitioning between quartz and zircon is much more likely to be preserved. Textural evidence that quartz inclusions in zircon are primary and unaffected by post-

crystallization recrystallization or diffusion at the quartz-zircon interface is likely a more reliable

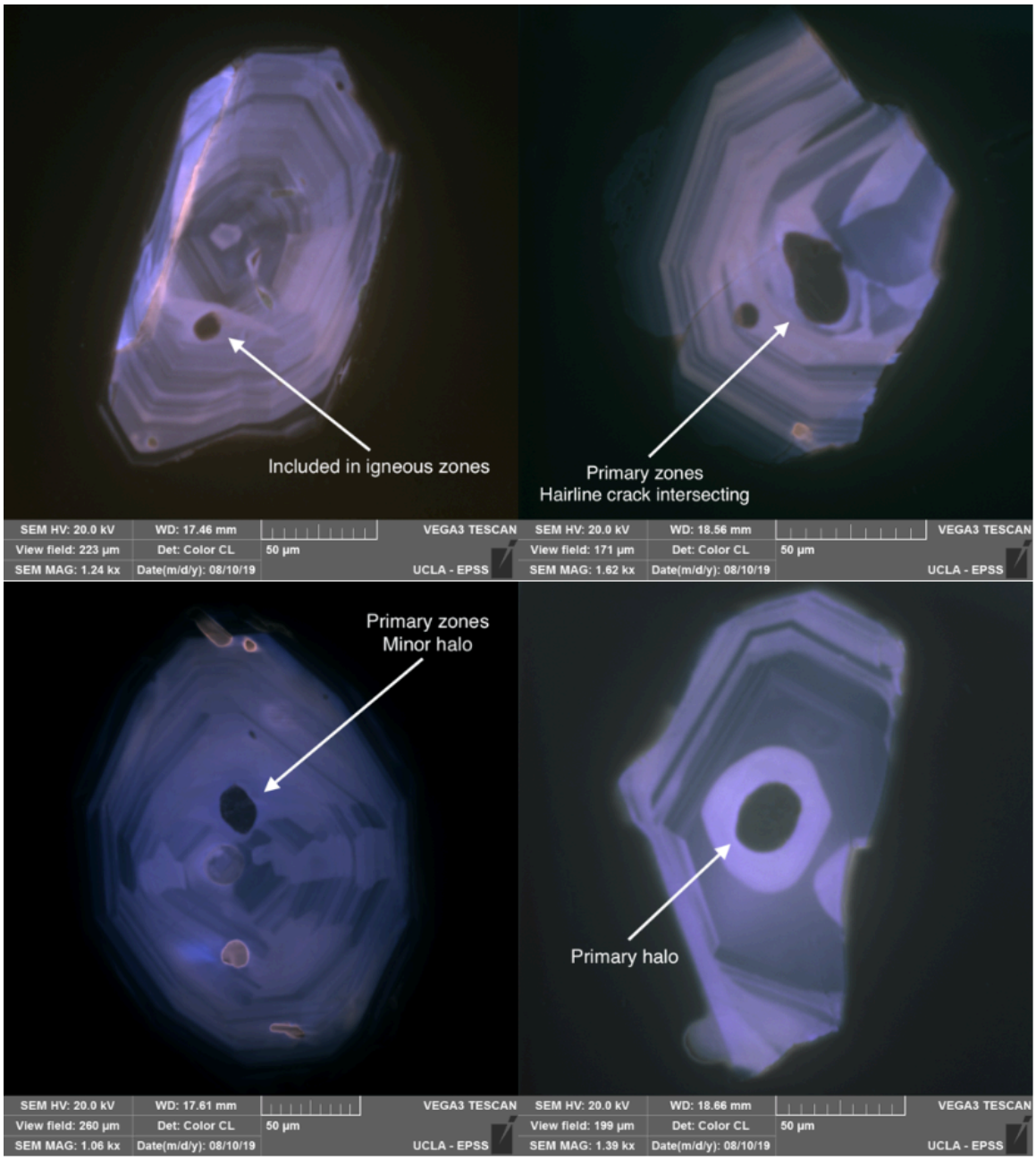

Figure 0.1 Color-CL images of zircons with primary quartz inclusions. CL intensities are not to scale between images. These zircons and their quartz inclusions did not have equilibrium $\Delta^{18}O_{qtz\text{-}zir}$, but did not show evidence of disturbed [Ti].

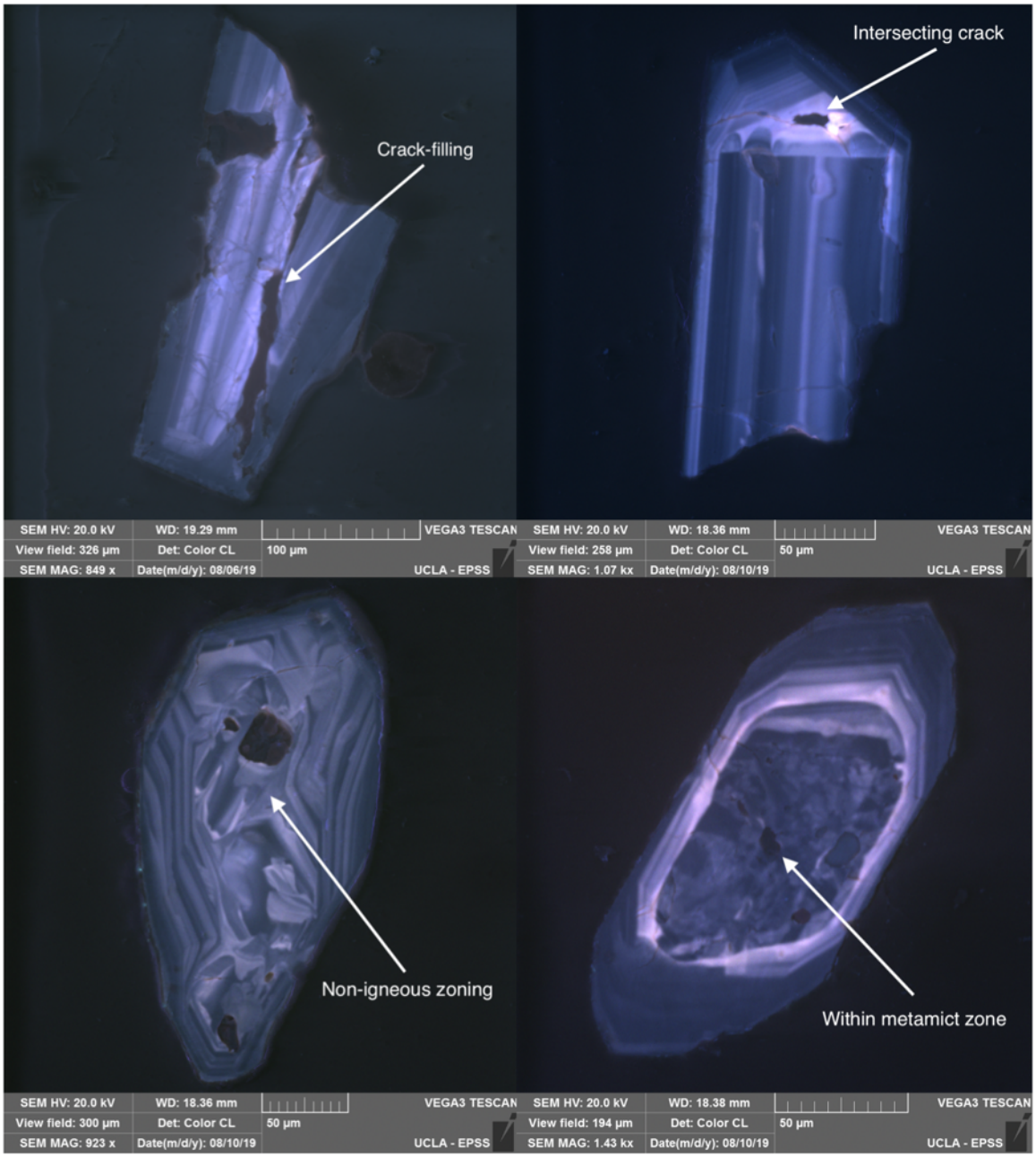

Figure 0.2: Examples of inclusion textures consistent with secondary alteration of quartz inclusions.

method for screening viable inclusion-host pairs.

4.2 Methods

4.2.1 Identification and Imaging of Quartz Inclusions

Zircons were mounted in epoxy, sectioned, and polished. Quartz inclusions in zircon

were identified using the Tescan Vega3 SEM equipped with EDAX Team EDS detector and software. Zircons with quartz inclusions were then imaged for textural analysis with the color-cathodoluminesence (CL) detector in order to determine whether inclusions were primary (Fig 4.1), secondary, or showed textural evidence of alteration (Fig. 4.2). CL imaging was performed following oxygen isotope analysis so as to preserve a smooth surface for maximum transmission and to minimize surface effects during ionization.

4.2.2 Titanium Concentration

Ti concentrations were measured with SIMS, which is sensitive enough to resolve [Ti] in zircon and quartz of as little as a fraction of a ppm; the ratio of $^{49}Ti/^{30}Si$ was measured in both unknowns and standards to account for variations in beam intensity and ionization efficiency. ^{49}Ti, though less abundant than other Ti isotopes, avoids mass interferences from Ca and V isotopes; ^{30}Si allows for use of the electron multiplier for both masses–more abundant Si isotopes would generate count rates too high for the EM. Whole quartz and zircon aliquots were analyzed on the CAMECA *ims*1270 at UCLA in monocollection mode using a ca. 12 nA beam focused to a ~30 µm spot. Zircons were simultaneously measured for U-Pb age using the same AS3 standard for both U-Pb and Ti. Ti concentrations for paired quartz inclusions and zircon hosts were measured on the CAMECA *ims*1290 at UCLA, using the Hyperion RF Plasma $^{16}O^-$ source with a ~5 nA beam focused to a ~2-3 µm spot. Zircon standards FC1 (21.6±0.8 ppm, Aikman, 2007) and 91500 (5.2 ± 1.5 ppm Ti, Wiedenbeck et al., 2004) and three reference glasses with 0, 100, and 500 ppm Ti (Gallagher & Bromiley, 2013) were used as zircon and quartz standards, respectively. Internal heterogeneity of standard materials exceeded analytical uncertainty, and was incorporated into the standard linear regression (using the New York regression method;

Mahon, 1996).

4.2.3 Titanium Thermobarometry

Zircon crystallization temperature (T_{zir}) was calculated using the calibration of Ferry and Watson (2007); quartz crystallization pressure (P_{qtz}) was calculated using the calibration of Thomas et al. (2010, 2015). Uncertainties in T_{zir} and P_{qtz} were calculated by propagating analytical, calibration, and a_{TiO_2} uncertainties by the Monte Carlo Method of error propagation using 10^5 iterations per value. The P_{qtz} calculation included the propagated error in T_{zir}; final values are taken from the mean and standard deviation of the 10^5 iterations. P_{qtz} of inclusions was calculated using T_{zir} of the adjacent zircon growth zone. P_{qtz} of whole quartz was calculated using T_{zir} calculated from the mean [Ti] (ppm) of an aliquot of 5-10 zircon grains. Depth equivalence of P_{qtz} was calculated using an average crustal density of 2750 kg m^{-3}, consistent with density profile estimates of continental arcs for a wide range of geothermal gradients (Lucassen et al., 2001).

4.2.4 Oxygen Isotopes

Oxygen isotope measurements of quartz inclusions and their host zircon were made simultaneously using the CAMECA *ims*1290 high-resolution ion microprobe at UCLA with a ~2.5 nA Cs^+ beam focused to a ~10 μm spot with mass resolving power >3000. Analyses were performed in multicollection mode with ^{16}O and ^{18}O measured with Faraday cups. Quartz standard QzCWRU ($\delta^{18}O$ = 24.52‰) and zircon standard AS3 ($\delta^{18}O$ = 5.34±0.04‰; Trail et al., 2007) were used to correct for instrumental mass fractionation in corresponding phases. Internal reproducibility was <0.2‰ for QzCWRU quartz and <0.3‰ for AS3 zircon. Linear drift in instrumental mass fractionation was monitored and corrected for as needed using the new York regression method (Mahon, 1996). $\Delta^{18}O_{qtz\text{-}zir}$ was calculated by subtracting the IMF-corrected

$\delta^{18}O_{qtz} - \delta^{18}O_{zir}$ (‰).

4.3 Results

The calibration of Thomas et al (2010; 2015) is constrained between 5 kbar and 20 kbar, with recent work suggesting that at >20 kbar, the calibration significantly overestimates pressure of crystallization (Thomas et al., 2019); results greatly exceeding 20 kbar (~ 75 km apparent depth) are therefore likely not accurate.

4.3.1 Whole quartz inclusions

Analysis of 27 plutons, with 10 quartz grains analyzed for each sample, ranging from 82.2±6.9 Ma to 42.1±0.8 Ma (2 s.e.) demonstrate a notable increase in apparent depths for samples younger than 65 Ma. Uncertainties in P_{qtz}, and calculated apparent depth, reflect the dispersion of [Ti] in both quartz and zircon aliquots as well as the propagated calibration uncertainties of T_{zir} and P_{qtz}. While collision is typically invoked to have begun as early as 57 Ma (Leech et al., 2005), maximum P_{qtz} depths begin increasing noticeably beginning 60 Ma. >65 Ma samples range in apparent depth from 21.5±9.4 km to 44.4±8.8 km (1σ), while <60 Ma samples range from 24.0±8.2 km to 66.9±10.0.1 km; the maximum depth is in the youngest sample at 42.1±0.8 Ma (Fig. 4.3). Median apparent depth increases from 36.5±6.9 km (1σ) to 43.2±11.3 km. The increased median and standard deviation post-60 Ma is driven by an increase in the maximum apparent depths, while minimum apparent depths remain approximately 20 km for all

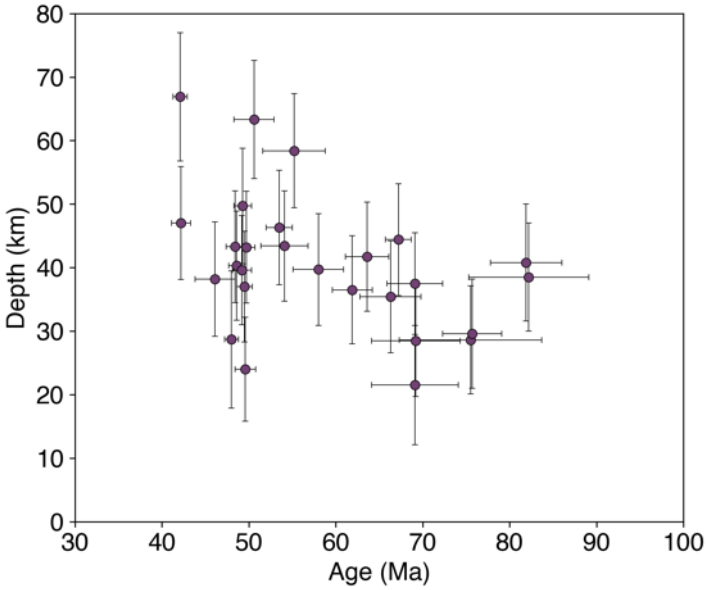

Figure 0.3: Apparent depths calculated from P_{qtz} of whole quartz grain aliquots using ρ_{crust} = 2750 kg m^{-3}. Error bars for depth are 1σ of calculated P_{qtz} apparent depth; age error is 2 s.e. of the weighted mean.

ages.

4.3.2 Quartz inclusions in zircon

154 quartz inclusions and their zircon hosts were each analyzed for T_{zir}, P_{qtz}, and $\Delta^{18}O_{qtz\text{-}zir}$, and U-Pb ages from aliquots of ~10 zircons per sample. Ranging in age from 96±7.9 Ma to 42±0.8 Ma, the inclusions, when unfiltered for primary magmatic textures, display a range of apparent depths that span the calibration limits of *TitaniQ* (Thomas et al., 2010; 2015) (Fig. 4.4).

These data include not only primary magmatic inclusions, but also inclusions which are

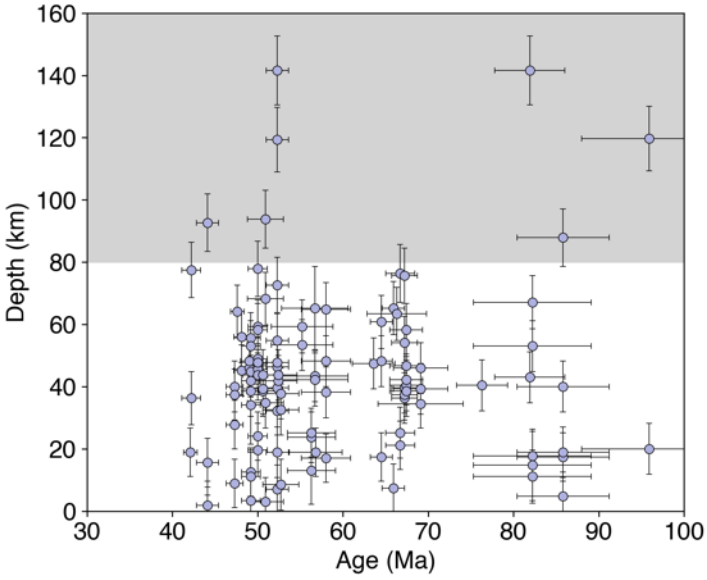

Figure 0.4. Apparent depths of all 154 inclusion-host pairs. Uncertainties in depth are 1σ; age error bars are 2 s.e. of the weighted mean. Gray box indicates region outside of *TitaniQ* calibration.

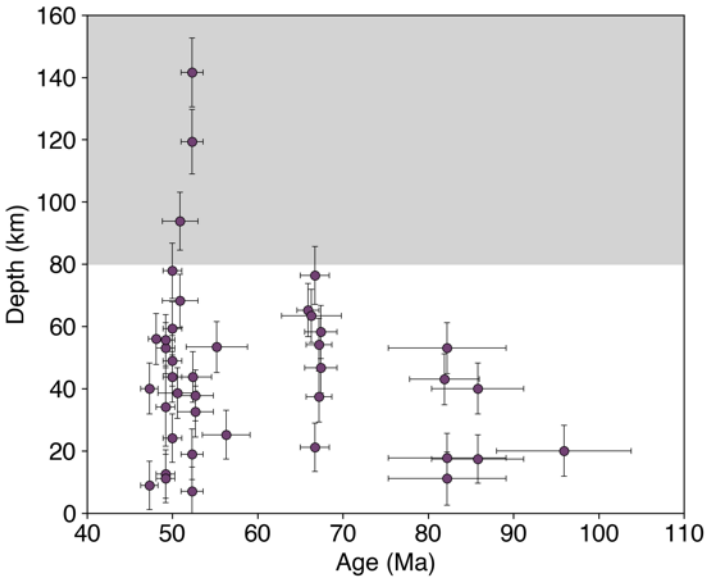

Figure 0.5: Apparent depths of only primary magmatic inclusions; error bars are the same as described in fig. 4.3.2. Gray box indicates pressure-equivalent depths outside of the TitaniQ calibration of Thomas et al. (2010; 2015).

either clearly secondary (e.g. filling cracks in the host zircon), or possess textural features consistent with secondary alteration (Fig. 4.2). Many primary inclusions are ringed by CL-bright haloes ranging from <2 μm to up to 30 μm, but this is likely a primary texture (fig. 4.1). CL-bright zones in zircon are governed mainly by the overlap of the ZrO_2 and SiO_2 bands, with additional minor contribution from variations in Dy concentration (Koschek, 1993). CL-bright haloes around quartz inclusions in zircon are therefore likely due to a zone of increased SiO_2 in the zircon lattice. Diffusion of Si and Ti in zircon is very slow even at magmatic temperatures (Cherniak et al., 1997; Cherniak & Watson, 2003; Cherniak, 2008); these CL-bright haloes are likely a primary texture resulting from the host zircon's contact with the SiO_2-saturated quartz interface.

Secondary inclusions are identified by fitting one or more of the following criteria: 1) filling cracks in the host zircon; 2) replacing metamict zones in the zircon; 3) highly irregular and anhedral grain shape; or 4) CL patterns in the host zircon suggestive of post-magmatic recrystallization. While most inclusions are not perfectly euhedral with a trigonal or hexagonal habit, primary inclusions are identified by their generally equant or prismatic shape (Fig. 4.1),

while secondary inclusions are more typically elongated, vermicular, or otherwise texturally inconsistent with a primary inclusion growth process (Fig. 4.2).

When inclusions with secondary textures are removed from the analyses, much of the spuriously high P_{qtz} data are filtered out (Fig. 4.5). There are three data which fall outside the limits of the Thomas et al. (2010; 2015) calibrations; though these cannot be relied upon at this time, it is possible they reflect pressures of ca. 22 – 32 kbar (i.e., 82 – 120 km), within the bounds of the as-yet-unpublished new calibration of high-*P* TitaniQ experiments (Thomas et al., 2019).

4.3.3 Oxygen Isotopes

Oxygen isotope fractionation of inclusion-host pairs was calculated by $\Delta^{18}O_{qtz\text{-}zir} = \delta^{18}O_{qtz} - \delta^{18}O_{zir}$, where $\delta^{18}O$ is the per-mil (‰) difference between the measured ratio of $^{18}O/^{16}O$ and the ratio of Vienna Standard Mean Ocean Water (VSMOW), corrected for instrumental mass fractionation with matrix-matched standards. Experimental calibration of oxygen isotope

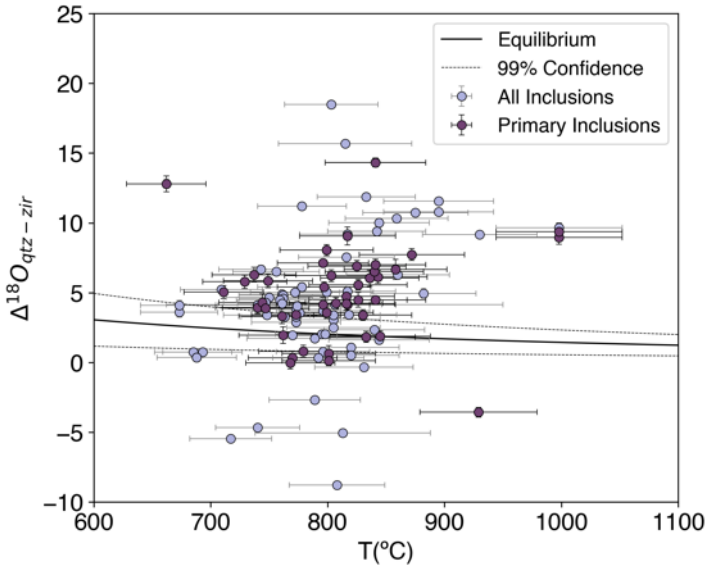

Figure 0.6: Oxygen isotope fractionation between quartz inclusions and zircon hosts. Experimentally predicted $\Delta^{18}O_{qtz\text{-}zir} = \delta^{18}O_{qtz} - \delta^{18}O_{zir}$ is shown with the solid line, and 99% confidence interval with the dashed lines (calibration of Trail et al., 2009). All inclusions shown in light purple; primary inclusions in dark purple. $T(°C) = T_{zir}$ of the host zircon. Error bars on T are 1σ of T_{zir}; error bars on $\Delta^{18}O_{qtz\text{-}zir}$ is 2 s.e. of the mean from counting statistics during analysis, which is typically smaller than the data points.

fractionation between quartz and zircon (Trail et al., 2009) predicts:

$$\Delta^{18}O_{qtz-zir} = \delta^{18}O_{qtz} - \delta^{18}O_{zir} \approx 1000 \ln \alpha_{qtz-zir} = \frac{2.33 \pm 0.24\text{x}10^6}{T(K)^2}$$

which results in quartz that is a few ‰ more enriched than zircon when in thermodynamic equilibrium at magmatic temperatures (Fig. 4.6).

Primary inclusions are closer to equilibrium than all inclusions overall, especially with fewer instances of significantly negative $\Delta^{18}O_{qtz\text{-}zir}$. Most inclusion-host pairs, however, have $\Delta^{18}O_{qtz\text{-}zir}$ that falls significantly outside the 99.9999998% confidence interval (6σ) of the experimental calibration of equilibrium fractionation. This likely results from exchange with hydrothermal fluids equilibrated either with supracrustal sediments enriched in ^{18}O, or with meteoric water depleted in ^{18}O relative to the primary magmatic values. Quartz more readily exchanges ^{18}O during hydrothermal alteration than zircon, so the primary equilibrium fractionation during crystal growth will be disproportionately modified by alteration of $\delta^{18}O_{qtz}$ (King et al., 1997; see discussion).

4.4 Discussion

4.4.1 Geologic context of P_{qtz}

In order to accurately interpret the results of this study, it is important to understand the geologic context that is being recorded in the analyzed values of P_{qtz} for both whole quartz as well as inclusion-host pairs. A first-order assumption is that quartz is crystallizing following initial melt generation and hybridization: in order to saturate quartz, a melt must be sufficiently enriched in SiO_2 such that SiO_2 is not exclusively sequestered in other silicate minerals. The evolved melt then must cool enough to saturate and crystallize quartz. In southern Tibetan granitoids, and indeed in most Cordilleran-style I-type plutons, empirical and experimental geochemistry indicate the vast majority of granitoid magmas are generated from a basaltic-

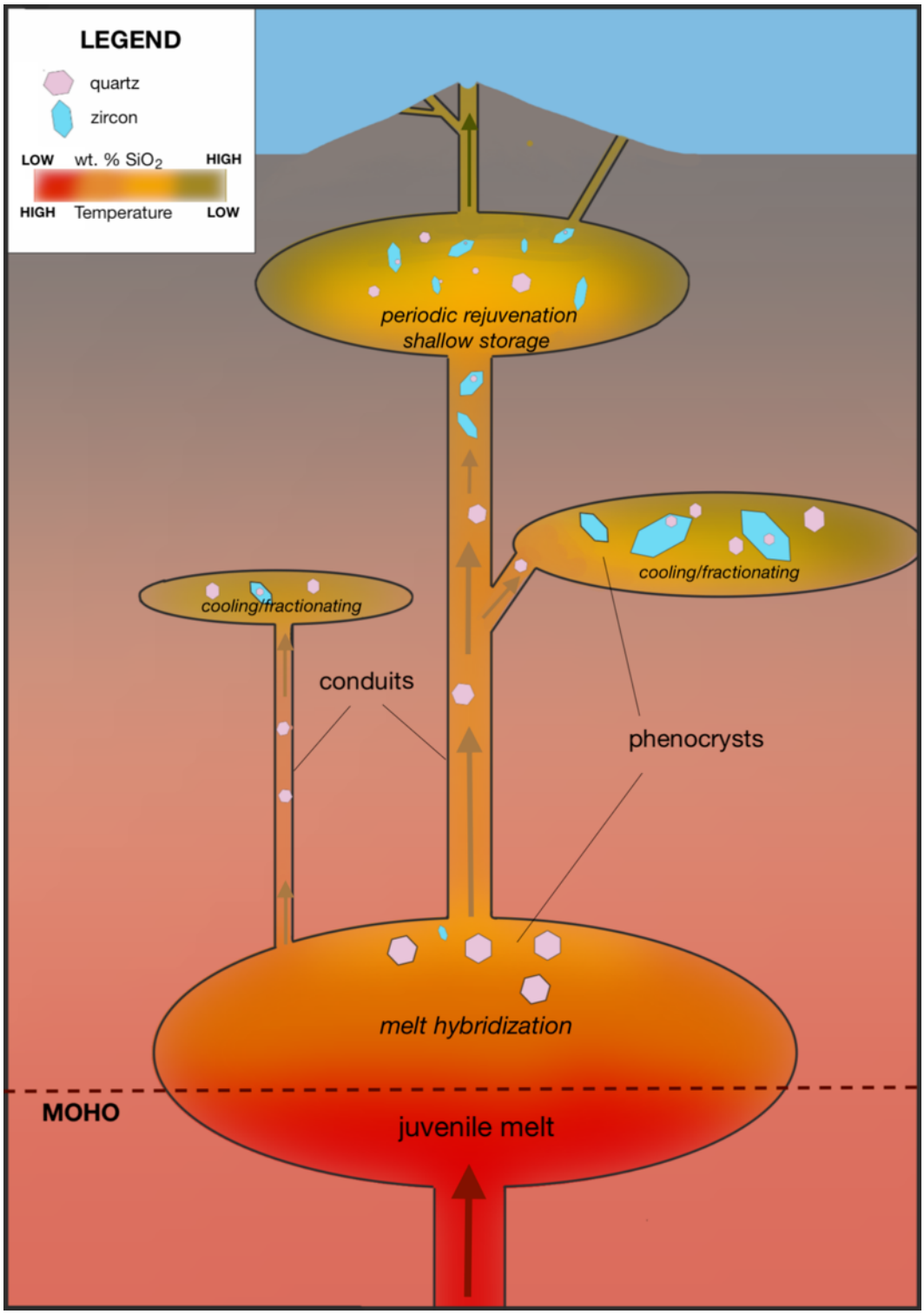

Figure 0.7: Schematic idealized diagram of a vertically extensive, compositionally heterogeneous magma system in which quartz (pink) and zircon (blue) crystals can nucleate, migrate, and/or include each other throughout various stages of melt generation and emplacement.

andesitic source with variable degrees of crustal assimilation (Roberts & Clemens, 1993; Douce,

1999; Alexander et al., 2019). A basaltic-andesitic source melt – generated either from partial melting of a hydrated mantle wedge, or from remelting of lower crustal cumulates and meta-igneous rocks – must achieve positive buoyancy relative to the surrounding lower crustal material to ascend and be emplaced or erupted. This can be achieved either with significantly higher *T* relative to a colder, denser lower crust; or through geochemical modification toward a lower-density, more felsic composition through fractionation and assimilation. Geochemical and geophysical studies indicate arc magmatism and crustal growth proceeds through an iterative sequence of partial melting, assimilation, and relamination of broadly andesitic magmas at the crust-mantle interface (Christensen & Mooney, 1995; Rudnick & Fountain, 1995; Sisson et al., 2005; Kelemen & Behn, 2016; Klaver et al., 2018). The maximum pressure (depth) at which quartz crystallizes from a differentiated silicic magma is therefore a minimum constraint on the thickness of the crust.

It is broadly understood that arc magmatism occurs through a multi-stage, vertically extensive, and thermally- and compositionally-heterogeneous process throughout which magma bodies can be alternately emplaced, cooled, recharged, and assimilate with surrounding crustal material (Cashman et al., 2017; and references therein). Crystallization of quartz and zircon is therefore likely to occur in multiple stages or regions during the generation, migration, and emplacement of granitoid magmas (Fig. 4.7). P_{qtz} results are best understood, therefore, as a range of pressures at which quartz was able to crystallize throughout the full history of granitoid magma-genesis and emplacement. A range of P_{qtz} values for a suite of plutons of a given age will be topologically representative of the minimum crustal thickness, indicated by the upper limit of P_{qtz}; and a lower limit on emplacement depth of granitic plutons, indicated by the minimum values of P_{qtz}. The range of P_{qtz} becomes a heuristic for a “zone of granitoid magmatism”,

representative of the vertical extent of the silicic portion of the trans-crustal magmatic system depicted in Fig. 4.7.

4.4.2 Whole quartz vs. Inclusions

Pressure-equivalent depths calculated from whole quartz analyses suggest rapid crustal thickening beginning at 65 Ma, the early onset of the India-Asia collision (Fig. 4.3). P_{qtz} values indicate the precollisional crust prior to 65 Ma was approximately 45-50 km thick, consistent with average crustal thicknesses of modern orogens (46 km) (Christensen & Mooney, 1995). Following 65 Ma, rapid crustal thickening is indicated by a P_{qtz} minimum crustal thickness of ca. 70 km, well before the canonical onset of continental collision at ca. 50 Ma (Yin & Harrison, 2000). Minimum emplacement depths of approximately 20 km persist throughout the ca. 50 Myr history of granitic magmatism recorded in these data.

Pressures recorded in quartz inclusions, however, suggest even greater depths of crystallization, especially after 70 Ma. P_{qtz} of primary inclusions imply an extremely thick crust well prior to the onset of collision. These results may not be entirely accurate, especially given that many inclusions approach the upper limit of the Thomas et al. (2010, 2015) calibration for P_{qtz}. Fig. 4.8 shows the dramatic dispersion of P_{qtz} of inclusions relative to whole quartz in the same rock. Taken at face value, these data suggest that arc magmatism is producing small quartz crystals in the lithospheric mantle, which is both geophysically and geochemically unlikely. More probable is that [Ti] of quartz inclusions has been modified following crystallization. Though diffusion of Ti is slow in the quartz lattice, fluid-mediated recrystallization of quartz inclusions could mobilize Ti and reset the primary magmatic signal. $\Delta^{18}O_{qtz\text{-}zir}$ of these inclusions suggests hydrothermal alteration of inclusions is not only likely, but almost certain (see § 4.4.3). It is also possible that some of the inclusions identified by EDS spectra are not crystalline quartz,

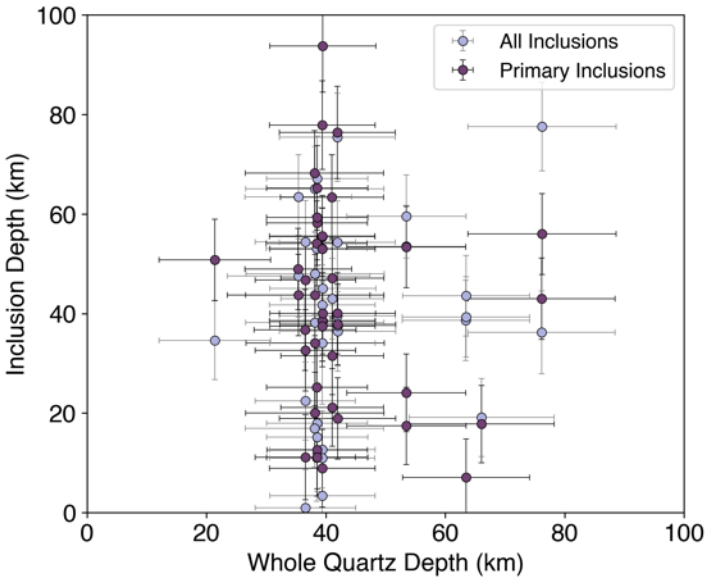

Figure 0.8: Relationship between P_{qtz}-equivalent depth of whole quartz and inclusions of discrete samples, with both primary (yellow) and secondary (cyan) inclusions shown. In most cases there are multiple inclusions per whole quartz datum, resulting in the vertical dispersion of inclusion depths for a given whole quartz depth.

but rather amorphous SiO_2, which could invalidate the application of the Ti-in-quartz thermobarometer. The calibration of Thomas et al. (2010; 2015) is based on thermodynamic data for quartz, which has significantly different thermodynamic and elastic properties compared to amorphous silica (Richet et al., 1982; Pabst & Gregorová, 2013). Inclusions that have been reset at temperatures significantly lower than T_{zir} will have spuriously high calculated P_{qtz}, as [Ti] in quartz is balanced by the interplay of $+\Delta V$ of thermal expansion and $-\Delta V$ of compression. If the inclusions have been reset at lower T, we can no longer rely on T_{zir} as the temperature constraint for the calculation of P_{qtz}. Further investigation of the crystal structure of quartz inclusions, as well as elastic thermobarometry, could elucidate these issues and provide some constraint as to the relevance of [Ti] of quartz inclusions in zircon.

As discussed in § 4.1.1, whole quartz crystals cannot be assumed *a priori* to be in thermodynamic equilibrium with separate zircon grains: it is possible that quartz crystallized in a different temperature regime than zircon. However, given that magma ascent in a conduit is isothermal, *sensu lato* (Costa et al., 2007), it is likely that the majority of quartz and zircon experienced similar crystallization temperatures. This notion is bolstered by the presence in these

granitoids of both quartz inclusions in zircon and zircon inclusions in quartz, suggesting approximately cotectic crystallization. Though whole quartz grains do not carry the guarantee of thermodynamic equilibrium with zircon during initial crystallization, their significantly larger volume relative to the inclusions (500 – 2000 μm vs. 5 – 30 μm diameter) armors them from complete resetting of primary [Ti] by hydrothermal interactions beginning at the grain interface.

4.4.3 Significance of $\Delta^{18}O_{\text{qtz-zir}}$

A majority of quartz inclusions in zircon are well outside of expected $\Delta^{18}O_{qtz\text{-}zir}$ equilibrium fractionation with their host zircons (Fig. 4.6). Alteration of $\Delta^{18}O_{qtz\text{-}zir}$ from magmatic equilibrium can occur through interaction with either hydrothermal fluids that have equilibrated with isotopically enriched sediments, or with isotopically depleted meteoric water. Secondary and highly altered inclusions are especially prone to large ($\geq \pm 10‰$) $\Delta^{18}O_{qtz\text{-}zir}$, bolstering the notion that oxygen isotopes of quartz inclusions can be progressively modified relative to their zircon hosts. These data are consistent with the probable modification of [Ti] in quartz inclusions from the primary magmatic signal. Fluid ingress could occur via micron-scale cracks in the host zircon, which will retain primary magmatic $\delta^{18}O$ while the quartz inclusion is modified.

Though Ti is significantly less mobile at hydrothermal conditions than O (Antignano & Manning, 2008), removal of a few ppm Ti will have drastic effects on calculated P_{qtz}. These data indicate that application of Ti thermobarometry to quartz inclusions in zircon requires significant vetting of quartz inclusions: they must possess an unaltered igneous crystal structure and have primary magmatic equilibrium $\Delta^{18}O_{qtz\text{-}zir}$ in order to be candidates for Ti thermobarometry. Applying just the $\Delta^{18}O_{qtz\text{-}zir}$ filter to this dataset reduces the number of usable inclusions to a quantity too small (n = 12) to draw real conclusions about the crustal thickening history of

southern Tibet.

4.4.4 Geologic implications of P_{qtz} results

Whole crystal P_{qtz} values provide compelling evidence that southern Tibet underwent rapid crustal thickening beginning early in the transition from oceanic subduction to continental collision. These data contradict indirect geochemical proxies applied in previous studies (e.g. Chen et al., 2018; DePaolo et al., 2019) and discussed in Chapters 2 and 3, which implied a thin margin of southern Tibet until well after the onset of continental collision. Given that the indirect geochemical proxies are based on or modified by assimilation with crustal material, it is probable that those proxies are subject to a geochemical hysteresis related to the evolving geothermal gradient during the tectonic transition from subduction to collision. [Ti] in quartz and zircon, however, record crystallization *P* and *T* conditions contemporaneously with granitoid formation, irrespective of second-order interactions with assimilated crustal material.

The consistent lower bound of ca. 20 km depth of quartz crystallization indicated by whole crystal P_{qtz} suggests a relatively static limit to the ability of granitic magmas to migrate vertically into the upper crust. While these data are not a direct constraint on the evolution of intra-crustal structure, they are consistent with the lack of structural evidence for upper-crustal deformation in southern Tibet in the past 65 Ma (Murphy et al., 1997; Yin & Harrison, 2000). P_{qtz} results indicate significant broadening of the zone of granitic magmatism post-65 Ma, exclusively extending into greater depths rather than symmetrically inflating both the lower and upper crust.

These data have profound implications for the rheology of the mid to lower crust, and by extension the deformation mechanisms available to southern Tibet as collision progressed. P_{qtz} results suggest a 60 km-thick trans-crustal magmatic system producing large volumes of

granitoid melts for many 10's of Ma prior to and after the onset of continental collision. In order to understand the thermo-mechanical implications of a widened zone of granitic magmatism, we must evaluate the thermal impacts of magmatic inflation in the context of overall orogenic heat flow. Previous studies have estimated ca. 15-30% magmatic inflation occurring in the mid Paleogene in the Tibetan plateau (e.g., Chen et al., 2018; DePaolo et al., 2019).

As a simple thought experiment, we can estimate the contribution of magmatic inflation to total Paleogene orogenic heat flow. The total surface heat flow, q_o (mW m^{-2}) can be described as the sum of mantle basal heat flow (q_m) and crustal radiogenic heat production:

$$q_o = q_m + A * C \tag{17}$$

where C is the crustal thickness and A is the average radiogenic heat production of the crust. Following the estimates of Rudnick & Gao (2014), we can use A = 0.89 μW m^{-3}. If q_m = 21 mW m^2 (Xian-Jie, 1991), and C is 50 km at 60 Ma, then total orogenic heat flow from basal heat flow and intracrustal radiogenic heat production would have been 65.5 mW m^{-2}. A 250000 km^2 orogen, approximately the size of the Lhasa terrane, would thus generate 1.1x10^{10} J/s of radiogenic heat, plus accumulate 5.3x10^9 J/s from mantle heat flow. P_{qtz} results suggest crustal thickening from ~50 km to ~80 km between 60 Ma and 40 Ma. Over the course of those 20 Ma, this equates to 10.3 TJ of total heat production, disregarding magmatic heat flux. Magmatic heat addition can be estimated from the density of granite magma (ρ = 2750 kg m^{-3}); its heat capacity C_p, the latent heat of crystallization, and the temperature of the magma. T_{zir} values in this study average 760ºC, or 1033K; according to the calibration of Miao et al. (2014), C_p would be ~1200 J kg^{-1} K^{-1} at this temperature. Latent heat of crystallization is approximated to 3x10^5 J kg^{-1} (Huppert & Sparks, 1988; Zhang et al., 2008). For the aforementioned orogen, magmatic heat is

calculated as:

$$Q_m = Q_T + Q_L \tag{18}$$

where Q_T is the heat from the temperature of the magma, and Q_L is the total heat produced by crystallization.

$$Q_T = V_o * f_m * T_m * \rho_m * C_{p(m)} \tag{19}$$

$$Q_L = V_o * f_m * L * \rho_m \tag{20}$$

where V_o is the volume of the orogen, f_m is the fraction of magmatic inflation, T_m, ρ_m, $C_{p(m)}$, and L are the temperature, density, heat capacity, and latent heat of crystallization per kg of the magma. If we assume an initial crustal thickness of 50 km at 60 Ma, increasing to 80 km by 40 Ma–as indicated by P_{qtz} results–and integrate the total magmatic inflation over this time period, we can calculate the impact of magmatic heat addition to the thermal budget of the orogen.

As crustal thickness increases, so does radiogenic heat production, thus producing higher q_o. Without magmatic inflation, 30 km of thickening increases q_o to 92 mW m^{-2} in this simplified model (Fig. 4.9). Magmatic inflation substantially increases the total heat budget of the orogen, even at relatively low volumes. Inflation of 10% over 20 Ma increases total Q of the orogen by 43%; inflation greater than 26% more than doubles the total heat production of the orogen (Fig. 4.9). The calculated total heat flow with magmatic inflation produces surface heat fluxes that are substantially higher than the average continental crust; 10% inflation leads to q_o of 92.6 – 116.6 mW m^{-2} from 50 km to 80 km thickness. These calculations are likely overestimates of actual

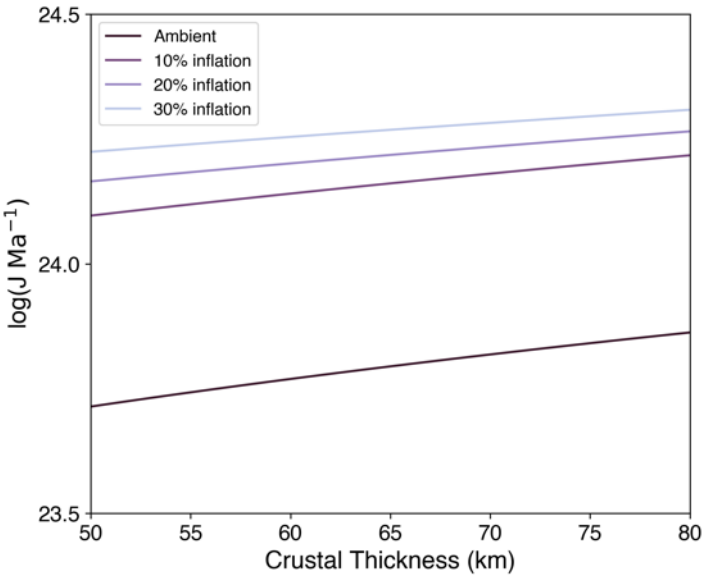

Figure 0.9: Modeled orogenic heat production per million years due to 30 km of thickening over 20 Ma. Curves are the log of heat production in an amagmatic orogen (ambient), and 10%, 20%, and 30% magmatic inflation. Units are in Joules per million years.

surface heat flow (q_o), which is dependent not only on the total radiogenic and magmatic heat production, but also the proximity of heat production to the surface (Jaupart & Mareschal, 2014). Nevertheless, these simple calculations suggest that magmatic addition in the range of 10-30% over the course of 20-30 Ma would have significantly influenced the orogenic heat budget of southern Tibet during the onset of collision, considerably impacting the thermomechanical properties of the mid- to lower-crust.

Relatively continuous emplacement of plutons throughout this zone of granite magmatism from 20km depth to the Moho would produce a steepened upper-crustal geotherm (Fig. 4.10) (Rothstein & Manning, 2003; Hasterok & Chapman, 2011). Magmatic heat input into the mid- and lower-crust produces a thermomechanical feedback cycle where hot, weak zones in the crust are more easily maintained, weakening the crust overall and prolonging the ability of injected magmas to assimilate with the surrounding country rock (de Silva & Gregg, 2014; Rees

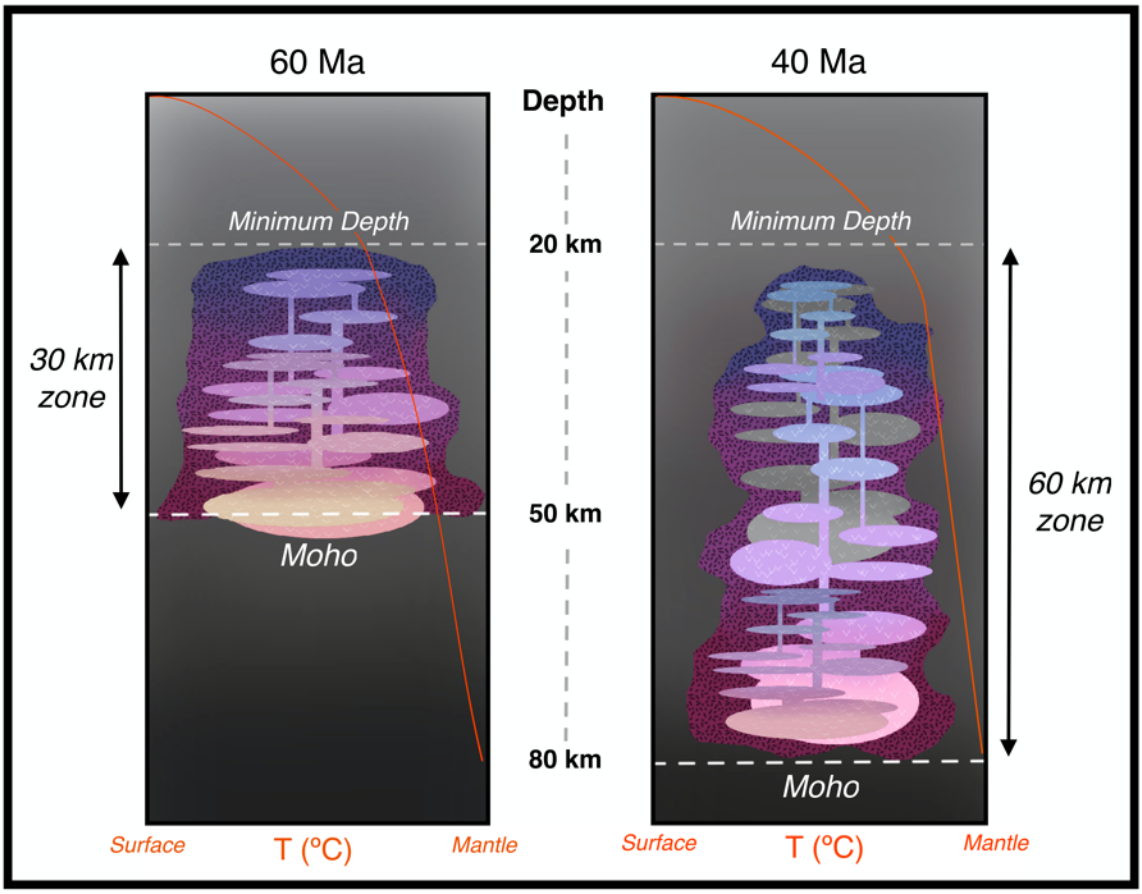

Figure 0.10: Schematic illustration of the "zone of plutonic activity" from 60 Ma to 40 Ma. Minimum depth of magmatism remains ca. 20 km, but rapid crustal thickening is indicated by an increase in maximum depths from $P_{qtz.}$ The geothermal gradient (orange line) is more steep in the upper crust by 40 Ma, due to persistent magmatism and thermal buffering in the plutonic zone leading to higher heat flux..

Jones et al., 2018). Moreover, thermal buffering of the mid- to lower-crust by metamorphism could reduce the apparent peak metamorphic temperatures observed in contemporaneous metamorphic units (Schorn et al., 2018), leading to an underestimate of the thermal gradient if metamorphic temperatures are the only proxy used for the evolving thermal regime. A crust weakened by magmatic heat below 20km depth could accommodate deformation primarily in the lower crust without significant strain rates in the upper crust (Gerbault et al., 2009); modern deformation of the southern Tibetan crust is consistent with a similar process of lower-crustal shortening and/or extrusion that is not manifested as dramatically at the surface (Royden et al.,

1997; Unsworth et al., 2005). Modern high heat flow in southern Tibet is attributed to plutonic activity in a similar zone as seen in the Paleogene (Francheteau et al., 1984; Wang, 2001); the observed deformation mechanisms seen in southern Tibet may represent a 60 Myr-long deformation regime in which collision is primarily accommodated through displacement and extrusion of the mid- to lower-crust due to weakening from continuous plutonic activity.

4.5 Conclusions

Ti-in-quartz and Ti-in-zircon thermobarometry is likely a more robust proxy for the crustal thickening history of southern Tibet when [Ti] is not affected by secondary alteration or diffusive loss. Quartz inclusions in zircon are susceptible to hydrothermal alteration and may be too small to be armored against resetting of primary magmatic [Ti]. Whole crystal P_{qtz} is likely retentive of primary magmatic signal due to larger grain size and armoring of primary core [Ti] by the outer volume of the grains. Whole crystal P_{qtz} results indicate rapid crustal thickening in southern Tibet much earlier than previously indicated by indirect geochemical proxies of crustal thickness. Maximum P_{qtz} values are representative of the minimum crustal thickness at the time of plutonism; minimum P_{qtz} values represent a lower limit on depth of emplacement for plutons in the mid-crust. These data demonstrate an extensive zone of plutonic activity between 20 km and the Moho; this zone of magmatic activity represents 75% of the Tibetan crust post-60 Ma, with substantial impact on the total heat budget of the orogen during the early- to mid-Paleogene.

Structural studies that seek to understand the deformation mechanisms necessary to accommodate hundreds of km of N-S shortening in southern Eurasia following the onset of the India-Asia collision must account for the rheological consequences of an extensive magmatic system in the lower three quarters of the crust. Magmatic activity in all but the upper quarter of the crust likely generated thermomechanical feedbacks that led to weakening of the crust,

potentially explaining the ability for the crust to undergo the extensive shortening required during collision without substantial deformation of the upper crust. Paleogene crustal structure and rheology were likely remarkably similar to modern southern Tibet's crustal structure and heat production, suggesting that collision-induced shortening has primarily been accommodated through mid- to lower-crustal thickening rather than upper-crustal shortening.

4.6 References

Agemar, T., Wörner, G., & Heumann, A. (1999). Stable isotopes and amphibole chemistry on hydrothermally altered granitoids in the North Chilean Precordillera: a limited role for meteoric water? *Contributions to Mineralogy and Petrology*, *136*(4), 331–344. https://doi.org/10.1007/s004100050542

Aikman, A. (2007). Tectonics of the eastern Tethyan Himalaya. Retrieved from https://openresearch-repository.anu.edu.au/handle/1885/146541

Alexander, E. W., Wielicki, M. M., Harrison, T. M., Lovera, O. M., & Depaolo, D. J. (2016, December). *Accessing the fourth dimension in orogenic reconstruction using granitoid thermobarometry*. Abstracts with Programs presented at the AGU Fall Meeting 2016, Moscone Center. Retrieved from https://agu.confex.com/agu/fm16/meetingapp.cgi/Paper/162115

Alexander, E. W., Wielicki, M. M., Harrison, T. M., DePaolo, D. J., Zhao, Z.-D., & Zhu, D.-C. (2019). Hf and Nd Isotopic Constraints on Pre- and Syn-collisional Crustal Thickness of Southern Tibet. *Journal of Geophysical Research: Solid Earth*, *124*, 11038–11054. https://doi.org/10.1029/2019JB017696

Anderson, J. Lawford, & Smith, D. R. (1995). The effects of temperature and fO_2 on the Al-in-hornblende barometer. *American Mineralogist*, *80*(5–6), 549–559.

https://doi.org/10.2138/am-1995-5-615

Anderson, J.L. (1996). Status of thermobarometry in granitic batholiths. *Earth and Environmental Science Transactions of The Royal Society of Edinburgh*, *87*(1–2), 125–138. https://doi.org/10.1017/S0263593300006544

Antignano, A., & Manning, C. E. (2008). Rutile solubility in H2O, H2O–SiO2, and H2O–NaAlSi3O8 fluids at 0.7–2.0 GPa and 700–1000 °C: Implications for mobility of nominally insoluble elements. *Chemical Geology*, *255*(1), 283–293. https://doi.org/10.1016/j.chemgeo.2008.07.001

Babeyko, A. Y., Sobolev, S. V., Trumbull, R. B., Oncken, O., & Lavier, L. L. (2002). Numerical models of crustal scale convection and partial melting beneath the Altiplano–Puna plateau. *Earth and Planetary Science Letters*, *199*(3), 373–388. https://doi.org/10.1016/S0012-821X(02)00597-6

Blattner, P., Abart, R., Adams, C. J., Faure, K., & Hui, L. (2002). Oxygen isotope trends and anomalies in granitoids of the Tibetan plateau. *Journal of Asian Earth Sciences*, *21*(3), 241–250. https://doi.org/10.1016/S1367-9120(02)00046-9

Boehnke, P., Watson, E. B., Trail, D., Harrison, T. M., & Schmitt, A. K. (2013). Zircon saturation re-revisited. *Chemical Geology*, *351*, 324–334. https://doi.org/10.1016/j.chemgeo.2013.05.028

Bray, R. E. (1969). Igneous rocks and hydrothermal alteration at Bingham, Utah. *Economic Geology*, *64*(1), 34–49. https://doi.org/10.2113/gsecongeo.64.1.34

Brown, M. (1994). The generation, segregation, ascent and emplacement of granite magma: the migmatite-to-crustally-derived granite connection in thickened orogens. *Earth-Science*

Reviews, *36*(1), 83–130. https://doi.org/10.1016/0012-8252(94)90009-4

Burov, E., & Yamato, P. (2008). Continental plate collision, P–T–t–z conditions and unstable vs. stable plate dynamics: Insights from thermo-mechanical modelling. *Lithos*, *103*(1), 178–204. https://doi.org/10.1016/j.lithos.2007.09.014

Cashman, K. V., Sparks, R. S. J., & Blundy, J. D. (2017). Vertically extensive and unstable magmatic systems: A unified view of igneous processes. *Science*, *355*(6331). https://doi.org/10.1126/science.aag3055

Chapman, J. B., Ducea, M. N., DeCelles, P. G., & Profeta, L. (2015). Tracking changes in crustal thickness during orogenic evolution with Sr/Y: An example from the North American Cordillera. *Geology*, *43*(10), 919–922. https://doi.org/10.1130/G36996.1

Chen, J.-L., Yin, A., Xu, J.-F., Dong, Y.-H., & Kang, Z.-Q. (2018). Late Cenozoic magmatic inflation, crustal thickening, and >2 km of surface uplift in central Tibet. *Geology*, *46*(1), 19–22. https://doi.org/10.1130/G39699.1

Cherniak, D. J. (2008). Si diffusion in zircon. *Physics and Chemistry of Minerals*, *35*(4), 179–187. https://doi.org/10.1007/s00269-007-0210-6

Cherniak, D. J., Hanchar, J. M., & Watson, E. B. (1997). Diffusion of tetravalent cations in zircon. *Contributions to Mineralogy and Petrology*, *127*(4), 383–390. https://doi.org/10.1007/s004100050287

Cherniak, D. J., Watson, E. B., & Wark, D. A. (2007). Ti diffusion in quartz. *Chemical Geology*, *236*(1), 65–74. https://doi.org/10.1016/j.chemgeo.2006.09.001

Cherniak, Daniele J., & Watson, E. B. (2003). Diffusion in Zircon. *Reviews in Mineralogy and*

Geochemistry, *53*(1), 113–143. https://doi.org/10.2113/0530113

Christensen, N. I., & Mooney, W. D. (1995). Seismic velocity structure and composition of the continental crust: A global view. *Journal of Geophysical Research: Solid Earth*, *100*(B6), 9761–9788. https://doi.org/10.1029/95JB00259

Claiborne, L. L., Miller, C. F., Flanagan, D. M., Clynne, M. A., & Wooden, J. L. (2010). Zircon reveals protracted magma storage and recycling beneath Mount St. Helens. *Geology*, *38*(11), 1011–1014. https://doi.org/10.1130/G31285.1

Costa, A., Melnik, O., & Vedeneeva, E. (2007). Thermal effects during magma ascent in conduits. *Journal of Geophysical Research: Solid Earth*, *112*(B12). https://doi.org/10.1029/2007JB004985

De Yoreo, J. J., Lux, D. R., & Guidotti, C. V. (1989). The role of crustal anatexis and magma migration in the thermal evolution of regions of thickened continental crust. *Geological Society, London, Special Publications*, *43*(1), 187–202. https://doi.org/10.1144/GSL.SP.1989.043.01.12

DePaolo, D. J., Harrison, T. M., Wielicki, M., Zhao, Z., Zhu, D.-C., Zhang, H., & Mo, X. (2019). Geochemical evidence for thin syn-collision crust and major crustal thickening between 45 and 32 Ma at the southern margin of Tibet. *Gondwana Research*, *73*, 123–135. https://doi.org/10.1016/j.gr.2019.03.011

Douce, A. E. P. (1999). What do experiments tell us about the relative contributions of crust and mantle to the origin of granitic magmas? *Geological Society, London, Special Publications*, *168*(1), 55–75. https://doi.org/10.1144/GSL.SP.1999.168.01.05

Farner, M. J., & Lee, C.-T. A. (2017). Effects of crustal thickness on magmatic differentiation in

subduction zone volcanism: A global study. *Earth and Planetary Science Letters*, *470*, 96–107. https://doi.org/10.1016/j.epsl.2017.04.025

Ferriss, E. D. A., Essene, E. J., & Becker, U. (2008). Computational study of the effect of pressure on the Ti-in-zircon geothermometer. *European Journal of Mineralogy*, *20*(5), 745–755. https://doi.org/10.1127/0935-1221/2008/0020-1860

Ferry, J. M. (1979). Reaction mechanisms, physical conditions, and mass transfer during hydrothermal alteration of mica and feldspar in granitic rocks from south-central Maine, USA. *Contributions to Mineralogy and Petrology*, *68*(2), 125–139. https://doi.org/10.1007/BF00371895

Ferry, J. M., & Watson, E. B. (2007). New thermodynamic models and revised calibrations for the Ti-in-zircon and Zr-in-rutile thermometers. *Contributions to Mineralogy and Petrology*, *154*(4), 429–437. https://doi.org/10.1007/s00410-007-0201-0

Francheteau, J., Jaupart, C., Jie, S. X., Wen-Hua, K., De-Lu, L., Jia-Chi, B., et al. (1984). High heat flow in southern Tibet. *Nature*, *307*(5946), 32–36. https://doi.org/10.1038/307032a0

Gallagher, C., & Bromiley, G. (2013). Ti in Quartz Standards. Retrieved from https://www.ed.ac.uk/geosciences/facilities/ionprobe/standard-materials-available/tiquartzstandards

Gerbault, M., Cembrano, J., Mpodozis, C., Farias, M., & Pardo, M. (2009). Continental margin deformation along the Andean subduction zone: Thermo-mechanical models. *Physics of the Earth and Planetary Interiors*, *177*(3), 180–205. https://doi.org/10.1016/j.pepi.2009.09.001

Ghiorso, M. S., & Gualda, G. A. R. (2013). A method for estimating the activity of titania in

magmatic liquids from the compositions of coexisting rhombohedral and cubic iron–titanium oxides. *Contributions to Mineralogy and Petrology*, *165*(1), 73–81. https://doi.org/10.1007/s00410-012-0792-y

Hammarstrom, J. M., & Zen, E. (1986). Aluminum in hornblende: an empirical igneous geobarometer. *American Mineralogist*, *71*(11–12), 12971313.

Harrison, T. M., Aikman, A.-, Holden, P.-, Walker, A. M., McFarlane, C.-, Rubatto, D.-, & Watson, E. B. (2005). Testing the Ti-in-Zircon Thermometer. *AGU Fall Meeting Abstracts*, *41*, V41F-1540.

Harrison, T. Mark, & Schmitt, A. K. (2007). High sensitivity mapping of Ti distributions in Hadean zircons. *Earth and Planetary Science Letters*, *261*(1), 9–19. https://doi.org/10.1016/j.epsl.2007.05.016

Harrison, T. Mark, Watson, E. B., & Aikman, A. B. (2007). Temperature spectra of zircon crystallization in plutonic rocks. *Geology*, *35*(7), 635–638. https://doi.org/10.1130/G23505A.1

Hasterok, D., & Chapman, D. S. (2011). Heat production and geotherms for the continental lithosphere. *Earth and Planetary Science Letters*, *307*(1), 59–70. https://doi.org/10.1016/j.epsl.2011.04.034

Hayden, L. A., & Watson, E. B. (2007). Rutile saturation in hydrous siliceous melts and its bearing on Ti-thermometry of quartz and zircon. *Earth and Planetary Science Letters*, *258*(3), 561–568. https://doi.org/10.1016/j.epsl.2007.04.020

Hofmann, A. E., Valley, J. W., Watson, E. B., Cavosie, A. J., & Eiler, J. M. (2009). Sub-micron scale distributions of trace elements in zircon. *Contributions to Mineralogy and*

Petrology, *158*(3), 317–335. https://doi.org/10.1007/s00410-009-0385-6

Hofmann, A. W., & Magaritz, M. (1977). Diffusion of Ca, Sr, Ba, and Co in a basalt melt: Implications for the geochemistry of the mantle. *Journal of Geophysical Research (1896-1977)*, *82*(33), 5432–5440. https://doi.org/10.1029/JB082i033p05432

Hu, F., Ducea, M. N., Liu, S., & Chapman, J. B. (2017). Quantifying Crustal Thickness in Continental Collisional Belts: Global Perspective and a Geologic Application. *Scientific Reports*, *7*(1), 1–10. https://doi.org/10.1038/s41598-017-07849-7

Huppert, H. E., & Sparks, R. S. J. (1988). The Generation of Granitic Magmas by Intrusion of Basalt into Continental Crust. *Journal of Petrology*, *29*(3), 599–624. https://doi.org/10.1093/petrology/29.3.599

Jaupart, C., & Mareschal, J.-C. (2014). 4.2 - Constraints on Crustal Heat Production from Heat Flow Data. In H. D. Holland & K. K. Turekian (Eds.), *Treatise on Geochemistry (Second Edition)* (pp. 53–73). Oxford: Elsevier. https://doi.org/10.1016/B978-0-08-095975-7.00302-8

Kapp, J. L. D., Harrison, T. M., Kapp, P., Grove, M., Lovera, O. M., & Lin, D. (2005). Nyainqentanglha Shan: A window into the tectonic, thermal, and geochemical evolution of the Lhasa block, southern Tibet. *Journal of Geophysical Research: Solid Earth*, *110*(B8). https://doi.org/10.1029/2004JB003330

Kapp, P., Manning, C. E., & Tropper, P. (2009). Phase-equilibrium constraints on titanite and rutile activities in mafic epidote amphibolites and geobarometry using titanite–rutile equilibria. *Journal of Metamorphic Geology*, *27*(7), 509–521.

https://doi.org/10.1111/j.1525-1314.2009.00836.x

Kelemen, P. B., & Behn, M. D. (2016). Formation of lower continental crust by relamination of buoyant arc lavas and plutons. *Nature Geoscience*, *9*(3), 197–205. https://doi.org/10.1038/ngeo2662

King, E. M., Barrie, C. T., & Valley, J. W. (1997). Hydrothermal alteration of oxygen isotope ratios in quartz phenocrysts, Kidd Creek mine, Ontario: Magmatic values are preserved in zircon. *Geology*, *25*(12), 1079–1082. https://doi.org/10.1130/0091-7613(1997)025<1079:HAOOIR>2.3.CO;2

Klaver, M., Blundy, J. D., & Vroon, P. Z. (2018). Generation of arc rhyodacites through cumulate-melt reactions in a deep crustal hot zone: Evidence from Nisyros volcano. *Earth and Planetary Science Letters*, *497*, 169–180. https://doi.org/10.1016/j.epsl.2018.06.019

Koschek, G. (1993). Origin and significance of the SEM cathodoluminescence from zircon. *Journal of Microscopy*, *171*(3), 223–232. https://doi.org/10.1111/j.1365-2818.1993.tb03379.x

Leake, B. E. (1998). Widespread secondary Ca garnet and other Ca silicates in the Galway Granite and its satellite plutons caused by fluid movements, western Ireland. *Mineralogical Magazine*, *62*(3), 381–386. https://doi.org/10.1180/002646198547648

Leech, M. L., Singh, S., Jain, A. K., Klemperer, S. L., & Manickavasagam, R. M. (2005). The onset of India–Asia continental collision: Early, steep subduction required by the timing of UHP metamorphism in the western Himalaya. *Earth and Planetary Science Letters*,

234(1), 83–97. https://doi.org/10.1016/j.epsl.2005.02.038

Lieu, W. K., & Stern, R. J. (2019). The robustness of Sr/Y and La/Yb as proxies for crust thickness in modern arcs. *Geosphere*, *15*(3), 621–641. https://doi.org/10.1130/GES01667.1

Lowry, R. K., Henderson, P., & Nolan, J. (1982). Tracer diffusion of some alkali, alkaline-earth and transition element ions in a basaltic and an andesitic melt, and the implications concerning melt structure. *Contributions to Mineralogy and Petrology*, *80*(3), 254–261. https://doi.org/10.1007/BF00371355

Lucassen, F., Becchio, R., Harmon, R., Kasemann, S., Franz, G., Trumbull, R., et al. (2001). Composition and density model of the continental crust at an active continental margin—the Central Andes between 21° and 27°S. *Tectonophysics*, *341*(1), 195–223. https://doi.org/10.1016/S0040-1951(01)00188-3

Mahon, K. I. (1996). The New "York" Regression: Application of an Improved Statistical Method to Geochemistry. *International Geology Review*, *38*(4), 293–303. https://doi.org/10.1080/00206819709465336

Miao, S. Q., Li, H. P., & Chen, G. (2014). Temperature dependence of thermal diffusivity, specific heat capacity, and thermal conductivity for several types of rocks. *Journal of Thermal Analysis and Calorimetry*, *115*(2), 1057–1063. https://doi.org/10.1007/s10973-013-3427-2

Miller, C. F., McDowell, S. M., & Mapes, R. W. (2003). Hot and cold granites? Implications of zircon saturation temperatures and preservation of inheritance. *Geology*, *31*(6), 529–532.

https://doi.org/10.1130/0091-7613(2003)031<0529:HACGIO>2.0.CO;2

Mungall, J. E., Dingwell, D. B., & Chaussidon, M. (1999). Chemical diffusivities of 18 trace elements in granitoid melts. *Geochimica et Cosmochimica Acta*, *63*(17), 2599–2610. https://doi.org/10.1016/S0016-7037(99)00209-4

Murphy, M. A., Yin, A., Harrison, T. M., Dürr, S. B., Chen, Z., Ryerson, F. J., et al. (1997). Did the Indo-Asian collision alone create the Tibetan plateau? *Geology*, *25*(8), 719–722. https://doi.org/10.1130/0091-7613(1997)025<0719:DTIACA>2.3.CO;2

Mutch, E. J. F., Blundy, J. D., Tattitch, B. C., Cooper, F. J., & Brooker, R. A. (2016). An experimental study of amphibole stability in low-pressure granitic magmas and a revised Al-in-hornblende geobarometer. *Contributions to Mineralogy and Petrology*, *171*(10), 85. https://doi.org/10.1007/s00410-016-1298-9

Nishimoto, S., & Yoshida, H. (2010). Hydrothermal alteration of deep fractured granite: Effects of dissolution and precipitation. *Lithos*, *115*(1), 153–162. https://doi.org/10.1016/j.lithos.2009.11.015

Pabst, W., & Gregorová, E. V. A. (2013). Elastic properties of silica polymorphs–a review. *Ceramics-Silikaty*, *57*(3), 167–184.

Profeta, L., Ducea, M. N., Chapman, J. B., Paterson, S. R., Gonzales, S. M. H., Kirsch, M., et al. (2015). Quantifying crustal thickness over time in magmatic arcs. *Scientific Reports*, *5*, 17786. https://doi.org/10.1038/srep17786

Putirka, K., Johnson, M., Kinzler, R., Longhi, J., & Walker, D. (1996). Thermobarometry of mafic igneous rocks based on clinopyroxene-liquid equilibria, 0–30 kbar. *Contributions*

to Mineralogy and Petrology, *123*(1), 92–108. https://doi.org/10.1007/s004100050145

Rees Jones, D. W., Katz, R. F., Tian, M., & Rudge, J. F. (2018). Thermal impact of magmatism in subduction zones. *Earth and Planetary Science Letters*, *481*, 73–79. https://doi.org/10.1016/j.epsl.2017.10.015

Richet, P., Bottinga, Y., Denielou, L., Petitet, J. P., & Tequi, C. (1982). Thermodynamic properties of quartz, cristobalite and amorphous SiO2: drop calorimetry measurements between 1000 and 1800 K and a review from 0 to 2000 K. *Geochimica et Cosmochimica Acta*, *46*(12), 2639–2658. https://doi.org/10.1016/0016-7037(82)90383-0

Roberts, M. P., & Clemens, J. D. (1993). Origin of high-potassium, calc-alkaline, I-type granitoids. *Geology*, *21*(9), 825–828. https://doi.org/10.1130/0091-7613(1993)021<0825:OOHPTA>2.3.CO;2

Rothstein, D. A., & Manning, C. E. (2003). Geothermal gradients in continental magmatic arcs; constraints from the eastern Peninsular Ranges Batholith, Baja California, Mexico. In *Special Paper 374: Tectonic evolution of northwestern Mexico and the Southwestern USA* (Vol. 374, pp. 337–354). Geological Society of America. https://doi.org/10.1130/0-8137-2374-4.337

Royden, L. H., Burchfiel, B. C., King, R. W., Wang, E., Chen, Z., Shen, F., & Liu, Y. (1997). Surface Deformation and Lower Crustal Flow in Eastern Tibet. *Science*, *276*(5313), 788–790. https://doi.org/10.1126/science.276.5313.788

Rudnick, R. L., & Gao, S. (2014). 4.1 - Composition of the Continental Crust. In H. D. Holland & K. K. Turekian (Eds.), *Treatise on Geochemistry (Second Edition)* (pp. 1–51). Oxford:

Elsevier. https://doi.org/10.1016/B978-0-08-095975-7.00301-6

Rudnick, Roberta L., & Fountain, D. M. (1995). Nature and composition of the continental crust: A lower crustal perspective. *Reviews of Geophysics*, *33*(3), 267–309. https://doi.org/10.1029/95RG01302

Ryerson, F. J., & Watson, E. B. (1987). Rutile saturation in magmas: implications for TiNbTa depletion in island-arc basalts. *Earth and Planetary Science Letters*, *86*(2), 225–239. https://doi.org/10.1016/0012-821X(87)90223-8

Schmidt, M. W. (1992). Amphibole composition in tonalite as a function of pressure: an experimental calibration of the Al-in-hornblende barometer. *Contributions to Mineralogy and Petrology*, *110*(2), 304–310. https://doi.org/10.1007/BF00310745

Schoene, B., Schaltegger, U., Brack, P., Latkoczy, C., Stracke, A., & Günther, D. (2012). Rates of magma differentiation and emplacement in a ballooning pluton recorded by U–Pb TIMS-TEA, Adamello batholith, Italy. *Earth and Planetary Science Letters*, *355–356*, 162–173. https://doi.org/10.1016/j.epsl.2012.08.019

Schorn, S., Diener, J. F. A., Powell, R., & Stüwe, K. (2018). Thermal buffering in the orogenic crust. *Geology*, *46*(7), 643–646. https://doi.org/10.1130/G40246.1

Schott, B., & Schmeling, H. (1998). Delamination and detachment of a lithospheric root. *Tectonophysics*, *296*(3), 225–247. https://doi.org/10.1016/S0040-1951(98)00154-1

de Silva, S. L., & Gregg, P. M. (2014). Thermomechanical feedbacks in magmatic systems: Implications for growth, longevity, and evolution of large caldera-forming magma reservoirs and their supereruptions. *Journal of Volcanology and Geothermal Research*,

282, 77–91. https://doi.org/10.1016/j.jvolgeores.2014.06.001

Sisson, T. W., Ratajeski, K., Hankins, W. B., & Glazner, A. F. (2005). Voluminous granitic magmas from common basaltic sources. *Contributions to Mineralogy and Petrology*, *148*(6), 635–661. https://doi.org/10.1007/s00410-004-0632-9

Thomas, J. B., Nachlas, W. O., Osborne, Z. R., Hoff, C., & Watson, E. B. (2019). Extended and improved Ti-in-quartz solubility model. In *AGU Fall Meeting 2019*. Retrieved from https://agu.confex.com/agu/fm19/meetingapp.cgi/Home/0

Thomas, Jay B., Bruce Watson, E., Spear, F. S., Shemella, P. T., Nayak, S. K., & Lanzirotti, A. (2010). TitaniQ under pressure: the effect of pressure and temperature on the solubility of Ti in quartz. *Contributions to Mineralogy and Petrology*, *160*(5), 743–759. https://doi.org/10.1007/s00410-010-0505-3

Thomas, Jay B., Watson, E. B., Spear, F. S., & Wark, D. A. (2015). TitaniQ recrystallized: experimental confirmation of the original Ti-in-quartz calibrations. *Contributions to Mineralogy and Petrology*, *169*(3). https://doi.org/10.1007/s00410-015-1120-0

Trail, D., Mojzsis, S. J., Harrison, T. M., Schmitt, A. K., Watson, E. B., & Young, E. D. (2007). Constraints on Hadean zircon protoliths from oxygen isotopes, Ti-thermometry, and rare earth elements. *Geochemistry, Geophysics, Geosystems*, *8*(6), Q06014. https://doi.org/10.1029/2006GC001449

Trail, D., Bindeman, I. N., Watson, E. B., & Schmitt, A. K. (2009). Experimental calibration of oxygen isotope fractionation between quartz and zircon. *Geochimica et Cosmochimica Acta*, *73*(23), 7110–7126. https://doi.org/10.1016/j.gca.2009.08.024

Tremblay, M. M., Fox, M., Schmidt, J. L., Tripathy-Lang, A., Wielicki, M. M., Harrison, T. M.,

et al. (2015). Erosion in southern Tibet shut down at ~10 Ma due to enhanced rock uplift within the Himalaya. *Proceedings of the National Academy of Sciences*, *112*(39), 12030–12035. https://doi.org/10.1073/pnas.1515652112

Unsworth, M. J., Jones, A. G., Wei, W., Marquis, G., Gokarn, S. G., & Spratt, J. E. (2005). Crustal rheology of the Himalaya and Southern Tibet inferred from magnetotelluric data. *Nature*, *438*(7064), 78–81. https://doi.org/10.1038/nature04154

Wang, Y. (2001). Heat flow pattern and lateral variations of lithosphere strength in China mainland: constraints on active deformation. *Physics of the Earth and Planetary Interiors*, *126*(3), 121–146. https://doi.org/10.1016/S0031-9201(01)00251-5

Wark, D. A., & Watson, E. B. (2006). TitaniQ: a titanium-in-quartz geothermometer. *Contributions to Mineralogy and Petrology*, *152*(6), 743–754. https://doi.org/10.1007/s00410-006-0132-1

Watson, E. B., & Cherniak, D. J. (1997). Oxygen diffusion in zircon. *Earth and Planetary Science Letters*, *148*(3), 527–544. https://doi.org/10.1016/S0012-821X(97)00057-5

Watson, E. B., & Harrison, T. M. (2005). Zircon Thermometer Reveals Minimum Melting Conditions on Earliest Earth. *Science*, *308*(5723), 841–844. https://doi.org/10.1126/science.1110873

Wiedenbeck, M., Hanchar, J. M., Peck, W. H., Sylvester, P., Valley, J., Whitehouse, M., et al. (2004). Further Characterisation of the 91500 Zircon Crystal. *Geostandards and Geoanalytical Research*, *28*(1), 9–39. https://doi.org/10.1111/j.1751-908X.2004.tb01041.x

Xian-Jie, S. (1991). Crust and Upper Mantle Thermal Structure of Xizang (Tibet) Inferred from

the Mechanism of High Heat Flow Observed in South Tibet. In V. Čermák & L. Rybach (Eds.), *Terrestrial Heat Flow and the Lithosphere Structure* (pp. 293–307). Berlin, Heidelberg: Springer. https://doi.org/10.1007/978-3-642-75582-8_14

Yin, A., & Harrison, T. M. (2000). Geologic Evolution of the Himalayan-Tibetan Orogen. *Annual Review of Earth and Planetary Sciences*, *28*(1), 211–280. https://doi.org/10.1146/annurev.earth.28.1.211

Zhang, B., Wu, J., Ling, H., & Chen, P. (2008). Estimating Influence of Crystallizing Latent Heat on Cooling-Crystallizing Process of a Granitic Melt and Its Geological Implications. *Acta Geologica Sinica - English Edition*, *82*(2), 438–443. https://doi.org/10.1111/j.1755-6724.2008.tb00594.x

– Chapter 5 –

Synthesis

5.1 Summary of Findings

This work demonstrates the complexity of geochemical proxies for crustal thickness. Magmatic systems associated with continental arcs and collision zones experience a wide range of petrogenetic conditions that are shaped by the thermal regime of the orogen, source composition of juvenile melts, and the composition of pre-existing crust. Silicic melts formed in arcs and collision zones exhibit a wide range of trace element and isotopic compositions that are influenced not only by the provenance of juvenile melt, but also variable degrees of crustal assimilation, hydrothermal alteration, and post-emplacement weathering. Indirect proxies for crustal thickness are especially vulnerable to unconstrained effects of assimilation, assimilant composition, and local thermal regime. In southern Tibet, it is likely that a combination of a complex, evolving tectonic setting, crustal assimilation, degree of differentiation, deuteric alteration, and weathering coalesced to produce complex signals in isotope and trace element chemistry that are not controlled solely by crustal thickness. Indirect geochemical proxies alone cannot determine *a priori* whether changes in isotopic chemistry reflect crustal thickening or fundamental changes in the parameters controlling pluton composition.

Ti-in-quartz and Ti-in-zircon thermobarometry is likely a more robust proxy for the crustal thickening history of southern Tibet when [Ti] is not affected by secondary alteration or diffusive loss. Whole crystal P_{qtz} results indicate rapid crustal thickening in southern Tibet much earlier than previously indicated by indirect geochemical proxies of crustal thickness. These data demonstrate an extensive zone of plutonic activity between 20 km and the Moho prior to and during collision. Magmatic activity in all but the upper quarter of the crust likely generated thermomechanical feedbacks that led to weakening of the crust, potentially explaining the ability for the crust to undergo the extensive shortening required during collision without substantial

deformation of the upper crust. Barometry results suggest that collision-induced shortening could primarily have been accommodated through mid- to lower-crustal thickening rather than upper-crustal shortening, which is consistent with structural observations (England & Searle, 1986; Murphy et al., 1997; Royden et al., 1997).

The spatial isotopic gradient in southern Tibet discussed in Ch. 2 can be interpreted through two endmember scenarios: (1) if the isotope chemistry of the assimilant remains constant through time, then such a spatial gradient implies a similar gradient in crustal thickness (or, at a minimum, a gradient in pluton emplacement depths). (2) If the assimilant composition is variable with latitude, i.e. the assimilant endmember is more radiogenic near the southern margin of Tibet, we cannot assume that more radiogenic isotopic signatures in southern plutons necessarily indicates lower degrees of assimilation. Geochemical signatures of crustal assimilation are limited, however, by our ability to constrain the chemical endmembers of variably assimilated magmas. Thermobarometry results are not consistent with the thermoisotopic modeling discussed in Ch. 2; it is clear that magmatic rocks in southern Tibet have experienced wide variation in assimilant composition and trace element partitioning (Ch. 3), which confound the use of indirect proxies for crustal thickness.

5.2 Future Work

Further investigation of isotopic and trace element heterogeneity in lower crustal melting, assimilation, storage, and homogenization (MASH) zones could help improve our understanding of factors influencing apparent assimilation and pseudobarometer signatures in collisional magmas. Previous work studying lower-crustal and mantle xenoliths in southern Tibet have revealed a wealth of information on recent thermobarometric, geochemical, and petrologic conditions of the Tibetan lower crust (e.g. Hacker et al., 2000; Chan et al., 2009; Hébert et al.,

2014). Examination of xenoliths in pre- and syn-collisional magmas (e.g., in the Linzizong volcanic group, ca. 60 – 40 Ma (Lee et al., 2009)) would provide information on magma storage depth and temperature, as well as likely crustal and mantle endmembers for geochemical assimilation. Thermobarometry of metamorphic Paleogene xenoliths could test the robustness of the granitoid Ti thermobarometry record for providing minimum crustal thicknesses, and additionally distinguish between melt generation and storage regions. The isotopic and trace element chemistry of these xenoliths, in addition to providing assimilant endmembers, would clarify the relationship between pseudobarometer trace element ratios and crustal assimilation. Additionally, composition-specific, thermobarometrically-constrained forward modeling of RAFC processes in granitoid MASH zones could illuminate the sensitivity of trace element and isotopic assimilation to the depth, temperature, and longevity of magma storage.

Granitoid magmas in southern Tibet act as time capsules for the dynamic geochemical and petrogenetic history of the Tibetan plateau throughout the onset of the India-Asia collision. This work demonstrates the wealth of information held within these rocks, as well as the challenges associated with inverting complex geochemical and thermobarometric histories in the context of major tectonic events. Granitoid thermobarometry is likely the way forward to continued improvement of our understanding of the spatiotemporal evolution of the Tibetan plateau; the development and testing of Ti thermobarometry, as well as other thermobarometric tools, can produce a robust record of the dynamic crustal thickness of continental orogens. By reconstructing not only depth, but also thermal histories of magmas in orogens, we can better constrain the thermal, chemical, and mechanical evolution of orogens like the Tibetan plateau.

5.3 References

Bohrson, W. A., & Spera, F. J. (2001). Energy-Constrained Open-System Magmatic Processes

II: Application of Energy-Constrained Assimilation–Fractional Crystallization (EC-AFC) Model to Magmatic Systems. *Journal of Petrology*, *42*(5), 1019–1041. https://doi.org/10.1093/petrology/42.5.1019

Bohrson, W. A., & Spera, F. J. (2003). Energy-constrained open-system magmatic processes IV: Geochemical, thermal and mass consequences of energy-constrained recharge, assimilation and fractional crystallization (EC-RAFC). *Geochemistry, Geophysics, Geosystems*, *4*(2). https://doi.org/10.1029/2002GC000316

Chan, G. H.-N., Waters, D. J., Searle, M. P., Aitchison, J. C., Horstwood, M. S. A., Crowley, Q., et al. (2009). Probing the basement of southern Tibet: evidence from crustal xenoliths entrained in a Miocene ultrapotassic dyke. *Journal of the Geological Society*, *166*(1), 45–52. https://doi.org/10.1144/0016-76492007-145

DePaolo, D. J., Perry, F. V., & Baldridge, W. S. (1992). Crustal versus mantle sources of granitic magmas: a two-parameter model based on Nd isotopic studies. *Earth and Environmental Science Transactions of The Royal Society of Edinburgh*, *83*(1–2), 439–446. https://doi.org/10.1017/S0263593300008117

England, P., & Searle, M. (1986). The Cretaceous-tertiary deformation of the Lhasa Block and its implications for crustal thickening in Tibet. *Tectonics*, *5*(1), 1–14. https://doi.org/10.1029/TC005i001p00001

Hacker, B. R., Gnos, E., Ratschbacher, L., Grove, M., McWilliams, M., Sobolev, S. V., et al. (2000). Hot and Dry Deep Crustal Xenoliths from Tibet. *Science*, *287*(5462), 2463–2466. https://doi.org/10.1126/science.287.5462.2463

Hébert, R., Guilmette, C., Dostal, J., Bezard, R., Lesage, G., Bédard, É., & Wang, C. (2014).

Miocene post-collisional shoshonites and their crustal xenoliths, Yarlung Zangbo Suture Zone southern Tibet: Geodynamic implications. *Gondwana Research*, *25*(3), 1263–1271. https://doi.org/10.1016/j.gr.2013.05.013

Lee, H.-Y., Chung, S.-L., Lo, C.-H., Ji, J., Lee, T.-Y., Qian, Q., & Zhang, Q. (2009). Eocene Neotethyan slab breakoff in southern Tibet inferred from the Linzizong volcanic record. *Tectonophysics*, *477*(1), 20–35. https://doi.org/10.1016/j.tecto.2009.02.031

Lovera, O. M., Harrison, M., Schmitt, A. K., Wielicki, M. M., & Tierney, C. R. (2015). Numerical Simulation of Magma Reservoirs to Interpret Chrono-Chemical Signal. *AGU Fall Meeting Abstracts*, *43*. Retrieved from http://adsabs.harvard.edu/abs/2015AGUFM.V43B3156L

Murphy, M. A., Yin, A., Harrison, T. M., Dürr, S. B., Chen, Z., Ryerson, F. J., et al. (1997). Did the Indo-Asian collision alone create the Tibetan plateau? *Geology*, *25*(8), 719–722. https://doi.org/10.1130/0091-7613(1997)025<0719:DTIACA>2.3.CO;2

Royden, L. H., Burchfiel, B. C., King, R. W., Wang, E., Chen, Z., Shen, F., & Liu, Y. (1997). Surface Deformation and Lower Crustal Flow in Eastern Tibet. *Science*, *276*(5313), 788–790. https://doi.org/10.1126/science.276.5313.788

Spera, F. J., & Bohrson, W. A. (2001). Energy-Constrained Open-System Magmatic Processes I: General Model and Energy-Constrained Assimilation and Fractional Crystallization (EC-AFC) Formulation. *Journal of Petrology*, *42*(5), 999–1018. https://doi.org/10.1093/petrology/42.5.999

Spera, F. J., & Bohrson, W. A. (2002). Energy-constrained open-system magmatic processes 3. Energy-Constrained Recharge, Assimilation, and Fractional Crystallization (EC-RAFC).

Geochemistry, Geophysics, Geosystems, *3*(12), 1–20.

https://doi.org/10.1029/2002GC000315